Nanomechanical Characterization of Aging Effects in Solder Joints

by

Md Hasnine

A dissertation submitted to the Graduate Faculty of
Auburn University
in partial fulfillment of the
requirements for the Degree of
Doctor of Philosophy

Auburn, Alabama
December 12, 2015

Keywords: Solder Joint, Aging, Nanoindentation, EBSD, Creep, Hardness, Microalloy, Microdiffraction, Crystal Orientation

Approved by

Jeffrey C. Suhling, Chair, Quina Distinguished Professor of Mechanical Engineering
Hareesh V. Tippur, McWane Endowed Professor of Mechanical Engineering
Barton C. Prorok, Professor of Materials Engineering
Michael J. Bozack, Professor of Physics

Abstract

Over the past decade, it has been demonstrated the large changes that occur in the mechanical (constitutive) response and failure behavior of lead free solders after exposure to isothermal aging. For example, measured stress-strain data illustrate large reductions in stiffness, yield stress, ultimate strength, and strain to failure (up to 50%) during the first 6 months after reflow solidification. Even more dramatic evolution was observed in the creep response of aged solders, where up to 10,000X increases were found in the steady state (secondary) creep strain rate (creep compliance) of lead free solders that were subjected to elevated temperature aging at 125 C. All of prior work was based on uniaxial testing of miniature bulk solder tensile specimens formed in glass tubes. However, there has been little work on aging effects on mechanical properties and creep behavior in individual solder joints. Such knowledge is crucial for optimizing the design, manufacturing, and reliability of microelectronic packages. Characterization of individual joints is quite challenging because of their extremely small size, and the difficulty in gripping them and applying controlled loadings.

In this work, aging phenomena in actual solder joints have been explored by nano-mechanical testing of single lead free solder joints extracted from PBGA assemblies. The lead free solder joints in this study were extracted from Amkor CABGA, 14 x 14 mm, 192 balls, 0.8 mm ball pitch, 0.46 mm ball diameter. A variety of samples with 10 different solder ball alloys were studied. After extraction, the joints were subjected to various aging

conditions (0 to 12 months of aging at T = 125 C). Using nanoindentation techniques, the stress-strain and creep behavior of the SAC solder materials were explored at the joint scale for various aging conditions. Mechanical properties characterized as a function of aging include the elastic modulus, hardness, and yield stress. Using a constant force at maximum indentation, the creep response of the aged and non-aged solder joint materials was also measured as a function of the applied stress level. With these approaches, aging effects in actual solder joints are being quantified and correlated to the magnitudes of those observed in testing of miniature bulk specimens. Empirical models were also developed to predict the observed behavior. In addition, an approach has been developed to predict tensile creep strain rates for low stress levels using nanoindentation creep data measured at very high compressive stress levels.

In a second aspect of this study, the effects of silver content on SAC solder aging has been evaluated by testing joints from SACN05 (SAC105, SAC205, SAC305, and SAC405) test boards assembled with the same reflow profile. The observed aging effects in the SACN05 solder joints have been quantified and correlated with the magnitudes observed in tensile testing of miniature bulk specimens performed in prior studies. The ability of microalloy additions (dopants) to reduce aging effects in solder joints was also examined by nanoindentation testing of several sets of doped/non-doped alloys. The investigated solder joint alloys included: (1) SAC105, SAC205, SAC105+Ni, SAC105+Mn and SAC205+Ni and (2) low silver doped alloys, SAC0307, SAC0307+Bi (SACX) and SN100C. For the doped alloys, the base SAC solder in the PBGA component solder balls was modified by microalloying an additional small amount (< 0.05%) of the dopant material (Ni, Mn, Bi etc.). After aging, the joints were loaded in the

nanoindentation system, and the load-deformation behavior during indentation was used to characterize the mechanical properties of the solder joints for various aging conditions including modulus, hardness, and yield stress. With this approach, aging effects in joints have been quantified and compared to the behavior of the standard and doped alloys.

Due to the variety of crystal orientations realized during solidification, it was important to identify the grain structure and crystal orientations in the tested joints. Polarized light microscopy and Electron Back Scattered Diffraction (EBSD) techniques have been utilized for this purpose. As another part of this work, the enhanced x-ray microdiffraction technique at the Advanced Light Source (Synchrotron) at the Lawrence Berkeley National Laboratory was employed to characterize several joints after various aging exposures (0, 1, and 7 days of aging at T = 125 C). For each joint, microdiffraction was used to examine grain growth, grain rotation, sub-grain formation, and residual strain and stress evolution as a function of the aging exposure.

Acknowledgments

I would like to express my deepest appreciation to my advisor, Dr. Jeffrey Suhling, for his guidance, support and most importantly his friendship during the course of my PhD study at Auburn University. He continuously and convincingly convey a spirit of pursuit of excellence and perfection in research. I am really grateful that I had the opportunity to work with an exceptional mentor who taught me beyond what is expected in academia.

I am extremely thankful to Dr. Barton Prorok for his contribution, support and access to the nanomechanics lab during the entire nanoindentation experiment. I would like to thank to my advisory committee members including Dr. Hareesh V. Tippur, and Dr. Michael J. Bozack for their insightful instruction and discussion regarding this research. Special thanks are also extended to all my co-workers and friends, Safina Hussain, Mohammad Motaleb, Muhannad Mustafa, Munshi Basit, Nusratjahan Chhanda, Jordan Roberts, Promod Chowdhury, Sudan Ahmed, Quang Nguyen, Chien-Chih Chen, Nianjun Fu, Mohammad Alam, Abdullah Fahim, Md Mahmudur Chowdhury, KM Rafidh Hassan, MariAnne Sullivan and John Marcell for their help, encouragement and friendship.

I am heartily grateful to my parents and all of my family members for their support to my study and life in the United States. Finally, I solemnly dedicate this dissertation and all achievements in pursuit of doctoral degree to my wife, Selina B. Samira, for her perseverance and love, and her understanding during last year at graduate school have been priceless to me.

Table of Contents

List of Tables

List of Figures

CHAPTER 1

INTRODUCTION

1.1 Tin Lead Solders in Electronics

Solders have been used for join metal parts for nearly 5000 years. Initially, the soft solders based upon tin and lead were developed for structural application such as construction of tools, plumbing and seal the joints between lead sheets and applications continued to those of structural joining between materials such as lead and copper based alloys. However, soldering was also performed to ensure electrical continuity. Soldering technology using tin lead alloys has had a significant role in the packaging of highly functional and low cost electronic device.

Solder joints are an important part of micro-electronic packages because they serve as mechanical as well as electrical interconnects. Its properties are crucial to the integrity of a solder joint which in turn determine the overall function of the assembly. In packaging industry the eutectic and near eutectic tin-lead solders, 63Sn-37Pb (wt %) and 60Sn-40Pb have been used exclusively as a soldering alloys. The tin-lead binary eutectic system have a low melting temperature of 183 C, allowing for a process condition which is compatible with substrate and device packages. Lead offering many technical advantages over other alloys such Pb is inexpensive and available, preventing the allotropic formation of white or beta tin to gray or alpha tin upon cooling past 13 C which increase structural integrity, lower the surface tension for tin-lead solder which facilitates the filling of the gaps and

holes by solder and lead have higher resistance to corrosion. Moreover the technical attributes, scientific knowledge, manufacturing technique and reliability of Sn-Pb solder has been established [1].

However, unquestionably, lead is toxic to human being as well as animals. So, despite the outstanding advantages of Sn-Pb solders, European Union (EU) legislation passed the Waste from Electrical and Electronic Equipment (WEEE) and the restriction of the use of lead in Electrical and Electronic Equipment (RoHS) directives in 2002. As a consequence leads were banned in new electronic equipment in the EU as of 1 July 2006. So, the environmental and health concerns over the use of lead in microelectronic packaging have led to the vigorous development of alternative solder alloys largely based on Sn [2-4].

1.2 Lead Free Solders in Microelectronics

In microelectronic packaging application, solder must meet the performance requirements. First, solder alloy must have desired melting temperature. Second, it must meet the expected level of electrical and mechanical performance. Third, it needs to be adequately wet common PCB lands. Fourth, it should form the inspect-able solder joints, allow high volume soldering and rework of defective joints, provide reliable solder joints under service conditions. Fifth, solder alloy and assembly should be less expensive. A brief summary of the performance characteristics of the potential lead free solder are listed in table 1.1 [3].

Table 1.1 Performance Characteristics of Lead Free Solder

Manufacturing Properties	Reliability Performance
Melting/liquidus temperature	Electrical conductivity
Wettability	Thermal conductivity
Cost	Coefficient of thermal expansion
Environmental friendlies	Shear properties
Availability and number of suppliers	Tensile properties
Manufacturability using current process	Creep resistance
Ability to be made into balls	Fatigue properties
Copper pick up rate	Corrosion resistance
Recyclability	Oxidation resistance
Ability to be made into paste	Intermetallic compound formation

To identify the alternative lead free solder, it is important to ensure that the properties of the alternative solder are comparable or superior to the Pb-Sn solder. However, there are some expected criteria required for perfect lead free solder such as [3-4]:

- Melting temperature has to be similar to Pb-Sn
- Good wettability to form a proper metallurgical bond between two metals
- Good surface tension to form a good solder joints
- Good resistance to creep, fatigue, vibration
- Resistance to thermal expansion
- Adequate mechanical and electrical properties to ensure the reliability
- Resistance to corrosion and oxidation behavior
- Environmentally friendly, non-toxic, recyclable and inexpensive

1.3 Lead Free Candidates and Alloy Composition

A large number of lead free alloys have been proposed so far. The solder alloys are binary, ternary and some are even quaternary alloys. A total of 70 alloys were identified

from literature [3, 5 and 6]. However, majority of the solder alloys were based on Sn being primary or major constituent. Among several lead free solders, Sn-Ag, Sn-Cu, Sn-Ag-Cu and other alloys involving elements such as Sn, Ag, Cu, Bi, In and Zn have been identified as potential candidates for the replacement of standard Sn-Pb solder [7].

1.3.1 Tin

The tin has the ability to wet and spread on a wide range of substrate has caused it to become the principal component of the solder alloys used for electronic applications. Melting temperature of elemental tin is 231 C and allotropic transformation temperature is below 13 C. Tin exists in two different forms at two different crystal structures in solid state. One is white or β-tin has a body center tetragonal structure stable at room temperature and other is gray or α-tin has a diamond cubic crystal structure is thermodynamically stable below 13 C. The transformation of β-tin to α-tin referred to as tin pest which causes increase in volume which can induce cracking in the tin structure. Tin is highly anisotropic means coefficient of thermal expansion and elastic modulus are orientation dependent [3], Figure 1.1. Therefore, when tin is repeatedly exposed to thermal cycling, plastic deformation and eventually cracking can occur at grain boundaries. Thus thermal fatigue can be induce in tin rich solder even without any external mechanical strain. However, the addition of other alloys have been reported to be effective in suppressing these phase transformation [3].

1.3.2 Sn-Cu System

The Sn-Cu binary alloy has a eutectic compositions of Sn- wt. 0.7% and a eutectic temperature of 227 C. The solidification reaction forms a hollow rods of intermetallic

Cu_6Sn_5 (Figure 1.2). However, because of the high concentration of tin, it may form tin whisker or transformation to gray tin may occur. Moreover this alloy have low mechanical properties [8].

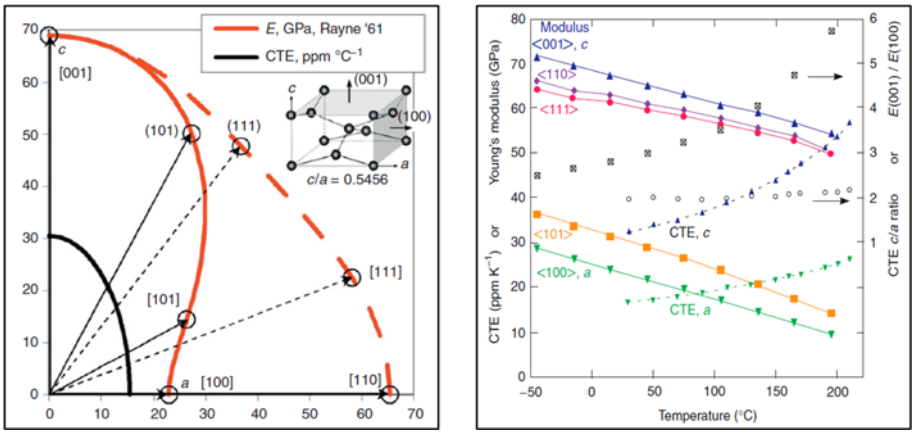

Figure 1.1 Coefficient of Thermal Expansion and Elastic Modulus as a Function of Crystal Orientation [3]

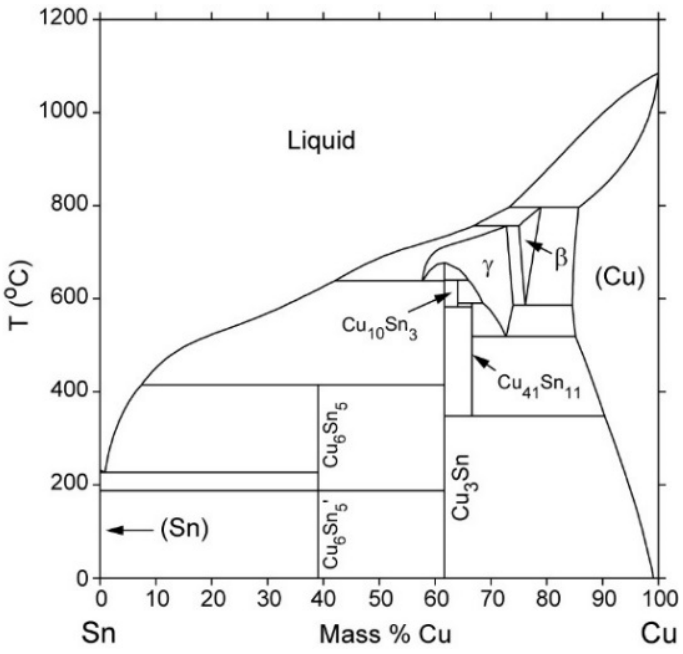

(http://www.metallurgy.nist.gov/phase/solder/cusn.html)

Figure 1.2 Sn-Cu Binary Phase Diagram

1.3.3 Sn-Ag System

The eutectic composition of the binary Sn-Ag system is of 96.5Sn-3.5 wt. %Ag and melting temperature is 221 C. From the phase diagram (Figure 1.3), the solidified microstructure consists with dendritic β-phase and eutectic dispersion of Ag_3Sn precipitates within a β- Sn matrix [9]. Similar to Sn-Cu, this alloy may be prone to whisker growth because of its high tin composition. This alloy also has poor wetting behavior in reflow application.

1.3.4 Sn-In System

This is the most commonly used alloy in SMT applications. The eutectic composition of this solder is In-49.1 wt. % Sn and melting temperature is 117 C.

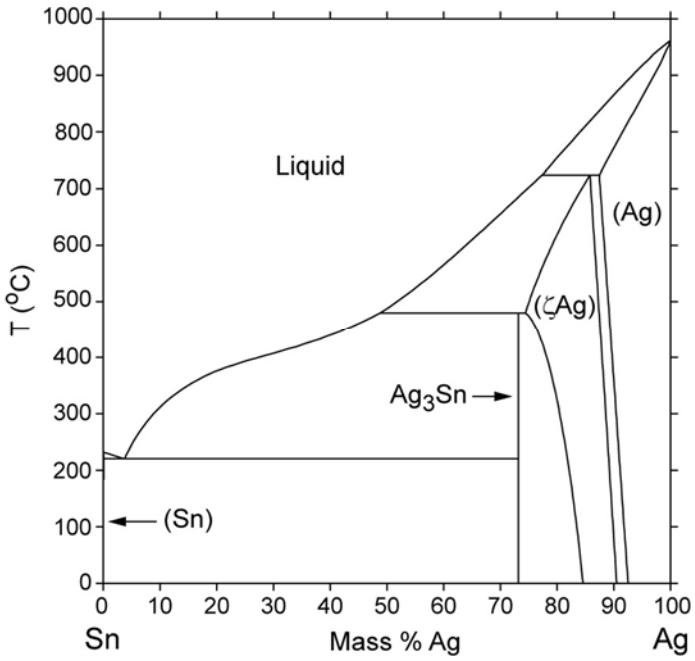

(http://www.metallurgy.nist.gov/phase/solder/agsn-w.jpg)

Figure 1.3 Sn-Ag Binary Phase Diagram

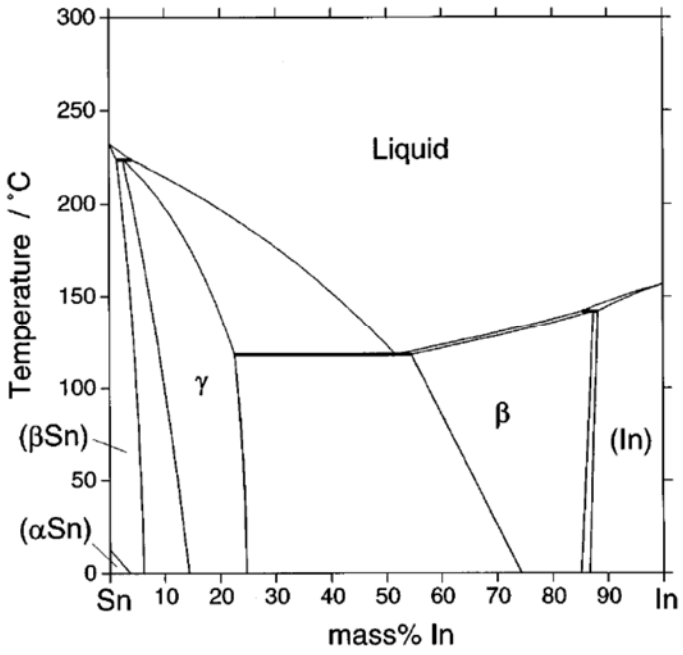

Figure 1.4 Sn-In Binary Phase Diagram [10]

1.3.5 Sn-Zn System

This alloy appears to be attractive alternative as its melting temperature is 198 C which is very close to tin-lead. The eutectic composition is Sn-9 wt. % Zn [3, 9]. The two different phases consists with Sn matrix phase and a secondary phase of hexagonal Zn containing less than 1% tin in solid solution. Both Sn and Zn interact with Cu to form intermetallic phases. The presence of Zn also leads to oxidation and corrosion due to the high potential of Zn.

1.3.6 Sn-Bi System

The Sn-Bi alloy has a eutectic composition of 42Sn-58Bi and relatively low melting temperature, 139 C. At moderate cooling rates, the eutectic Sn-Bi microstructure is lameller and resulted in the formation of large grains. However, tin precipitates from the

solder matrix along the boundaries of the large grains through which cracking occurs results in unpredictable early failure of solder joints. The interfacial segregation of Bi also results in a sharp decrease in fatigue and fracture resistance [3, 7].

1.3.7 Sn-Ag-Cu (SAC) System

Sn-Ag-Cu (SAC) alloys holding a commanding lead over all the lead free solder alloys used in today's market (Figure 1.5). Chart 1 shows the market share for wave soldering. Wave soldering is a process by which electronic circuit boards are slid over a pool of liquefied solder so that chips can be attached. Chart 2 reveals the market share for reflow soldering where the electronic circuit boards are screen printed with solder. The solder is then heated so that chip can be adhered to the boards [5].

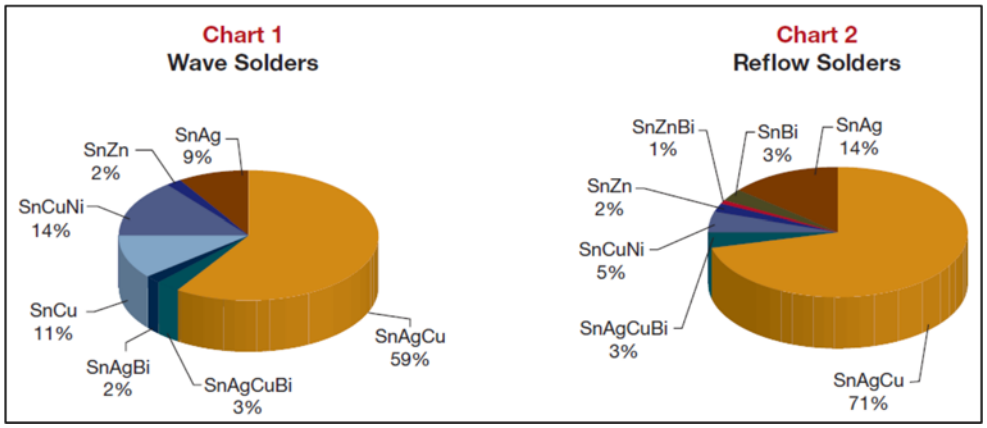

Figure 1.5 Lead Free Solder Market Share [5]

Several SAC alloys have been the proposed by various user groups and industry experts. These include 96.5Sn-3.0Ag-0.5Cu (SAC305), 95.5Sn-3.8Ag-0.7Cu (SAC387), 95.5Sn-3.9Ag-0.6Cu (SAC396) and 95.5Sn-4.0Ag-0.5Cu (SAC405), 95.5Sn-3.9Ag-0.6Cu (SAC396), 9Sn-0.3Ag-0.7Cu (SAC0307). For enhanced reliability of portable electronic

devices during accidental shock loading (e.g. high strain rates) several alloys with low silver content have been recommended including 98.5Sn-1.0Ag-0.5Cu (SAC105). The main benefits of the various SAC alloy systems are their relatively low melting temperatures compared with the Sn-Ag binary eutectic alloy, as well as their higher strength, superior resistance to creep and thermal fatigue and solderability when compared to other lead free solders.

From the phase diagram (Figure 1.6), the SAC ternary eutectic composition was found to be 3.5 wt. % Ag, 0.9 wt. % Cu and the balance Sn. And the eutectic temperature was found to be 217 C [6, 11]. Upon solidification, the microstructure of SAC alloy consists with three possible phases: β-Sn, Ag_3Sn and Cu_6Sn_5 [12-15], shown in Figure 1.7. The intermetallic compounds, Ag_3Sn and Cu_6Sn_5 nucleate with minimum undercooling whereas the β-tin phase requires 15-30 C undercooling to nucleate in solder joints. Because of this disparity in the undercooling for nucleation, plate like (Ag_3Sn) and rod like (Cu_6Sn_5) intermetallic grow to large in size in solder joint in the liquid phase if the cooling rate is slow. After nucleation, β-tin phase grows by a dendritic growth mechanism. The addition of Ag and Cu increase the flow stress which is a function of cooling rates [5]. Fast cooling rates increase the flow stress higher where slow cooling rates increase the strength modestly [16]. Ag and Cu also produces very hard intermetallic particle that acts to reinforce tin, allowing it to become a must stronger solder than Sn-Pb combinations. These fine dispersion of intermetallic particle pinning and blocking the movement of the dislocation thus increase the strength and reliability of solder joints.

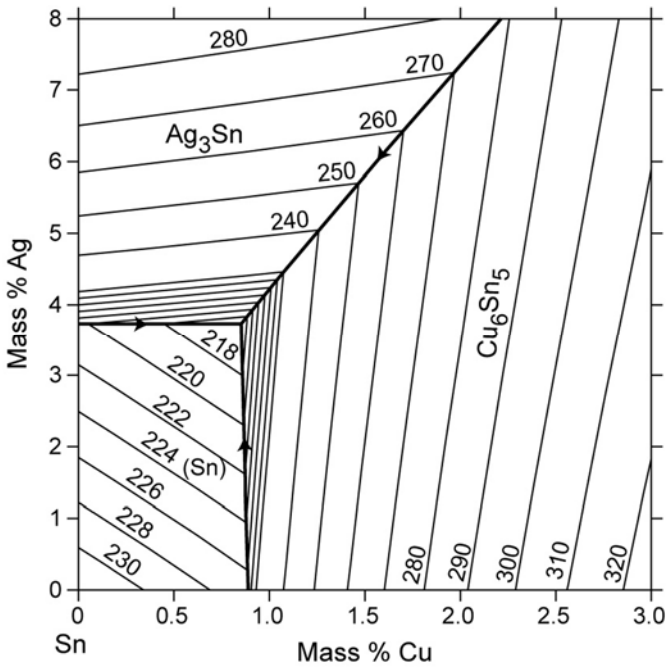

(http://www.metallurgy.nist.gov/phase/solder/agcusn-ll.jpg)

Figure 1.6 Sn-Ag-Cu Ternary Phase Diagram

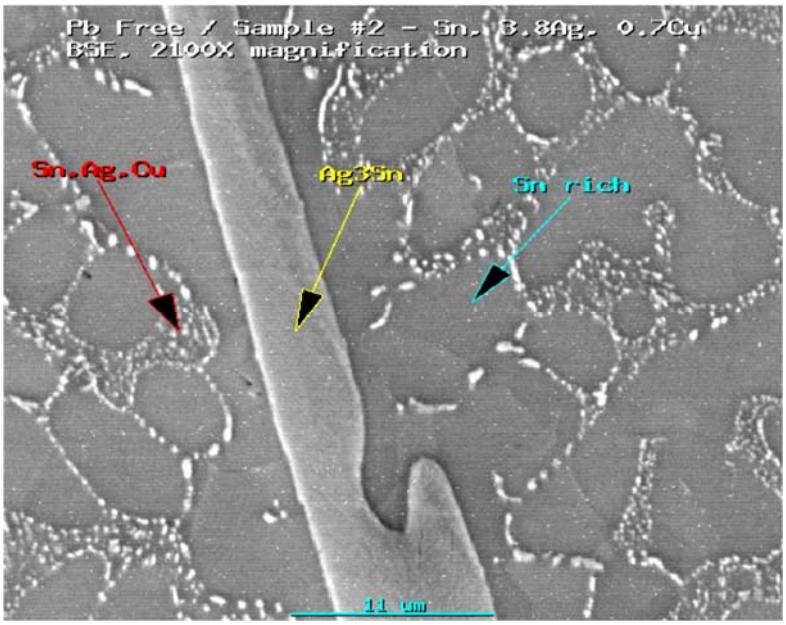

Figure 1.7 Typical SAC Solder Microstructure [14]

1.3.8 Doped Alloy (SAC+ X) System

SAC solders have shown more promising as to substitute for the Sn-Pb based solders. In view of that, the SAC solders are used in surface mount technology assemblies for microelectronics into industrial production. Since, the solder material has low melting temperature, creep deformation is one of the dominant deformation mode when homologous temperature, $T_h=T/T_m$, exceeds 0.4.Moreover, creep resistance is sensitive to the morphology of the second phase particle, depending on the composition and process parameters. Creep resistance can be enhance by the fine dispersion of precipitates. So, it is necessary to improve the mechanical properties of lead free solder alloys. The mechanical properties of solder joints can be greatly influenced by the addition of alloying elements or doped alloy [17]. Micro alloy element candidates include Bi, Zn, Ni, In, Co, Ge, Mn, Mg, Co, etc. Addition of such alloys modifies the microstructure and alter the bulk alloy characteristics, increase the volume fraction of eutectic phase and alter the crack pattern such improve the drop and shock reliability performance. It's also enhance the interfacial IMC layer properties by improving the ductility and toughness. Most of the doped solder alloy known to be increase the creep resistance by precipitate hardening or solid solution hardening of base alloy.

1.4 Mechanical Properties of Solder Materials

Solder joints are a critical part of microelectronic packages because they serve as electrical interconnects as well as mechanical support. The mechanical properties of solder alloy is critically important for making reliable products. Thermal fatigue, tensile and creep performance of solder joint is critically important for high reliability application.

Thus, accurate mechanical properties and constitutive equations for solder materials are needed for use in mechanical design, reliability assessment, and process optimization.

1.4.1 Tensile Properties

In real life application, solder joint experiences tensile loading. Therefore the tensile properties of solder alloy as such yield stress, ultimate tensile strength and elastic modulus is very important for determining the tensile deformation to which solder joint can sustain prior to failure.

Generally, tensile properties are described by stress-strain curves. In engineering application, engineering stress-strain are described as:

$$\sigma = \frac{P}{A} \tag{1.1}$$

$$\varepsilon = \frac{l_f - l_0}{l_0} \tag{1.2}$$

where, P is the load, A is the initial cross-sectional area, l_0 is the initial gauge length and l_f is the final gauge length.

Figure 1.8 shows the typical stress-strain curves for solder alloy. The curve consists with elastic and plastic region. In the elastic region, the engineering stress is linear and strain obeys the Hook's law:

$$\sigma = E\varepsilon \tag{1.3}$$

Where, E is the elastic modulus which can be determined form the slop of the elastic portion of the stress-strain curve.

The elastic modulus is inversely proportional to a power of the adjacent atomic distance X_0 at equilibrium as follows [16]:

$$E \propto \frac{1}{(X_0)^n} \tag{1.4}$$

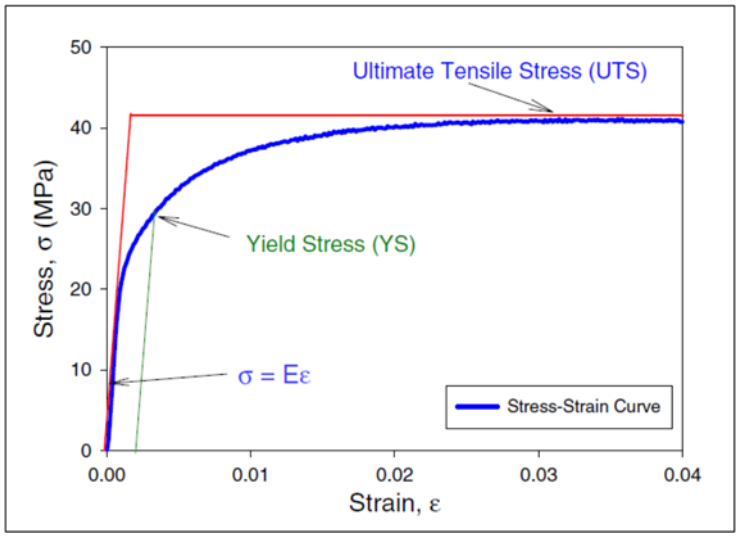

Figure 1.8 Typical Stress-Strain Response for Ductile Materials [16]

When the distance between the atoms is larger, the elastic modulus will be smaller. The value of the elastic modulus obtained from slope of the stress-strain curve is referred as apparent or effective modulus and it includes the inelastic deformation or time dependent deformation such as creep. When the load is high enough to exceed the elastic deformation, the material will experience plastic deformation. Materials subjected to plastic deformation will simultaneously elongate and decrease in diameter is called yielding. The yield stress is defined as the stress to cause the onset of plastic deformation. The ultimate tensile stress is the maximum stress level that the material can withstand before failure under uniaxial loading.

1.4.2 Creep of Solders

Creep deformation is one of the major failure mode of solder joints in microelectronic packaging because of its high homologous temperature. Solder experiences thermo-mechanical stresses due to different coefficient of thermal expansion between chip and other layers within the packages. These stresses can cause plastic deformation over a long period of service time [18]. Solder alloy go under creep deformation even at room temperature. In real life application electronic module operates over a -40 C to +125 C which are in the range of 0.48-0.87T_m and these range are rapid creep deformation range when devices are under stress. Thus, through understanding of creep deformation in lead free solder is the uppermost concern for the electronic packaging industry.

Creep of materials is associated with time-dependent plasticity under a constant stress at an elevated temperature. When the test specimen is subjected to a constant load, the initial, instantaneous response includes elastic and time-independent plastic flow. Creep then proceeds in three stages of primary, secondary and tertiary creep (Figure 1.9).

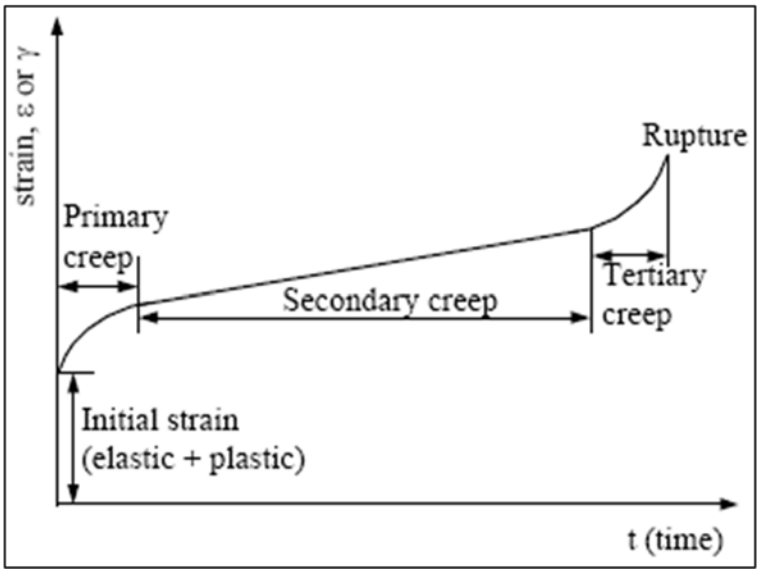

(http://www.msed.nist.gov/solder/clech/Sn-Pb_Creep.htm)

Figure 1.9 Typical Creep Response for Ductile Materials

Primary Creep

During this stage, creep, the strain rate decreases over time, due to strain hardening which restricts the deformation.

Secondary or Steady State Creep

For most metals, secondary creep is the dominant deformation mode at temperatures above half the melting temperature. In this stage, strain rate is retarded by the strain hardening while recrystallization and recovery tends to accelerate the creep rate. The two processes of hardening and softening reaches a dynamic balances and creep rate is very stable.

Tertiary Creep

In this stage creep strain rate increases rapidly until the specimen ruptures. Tertiary creep proceeds by void formation and growth along grain boundaries, micro-cracking and necking of tensile specimens.

1.4.3 Creep Deformation Mechanisms

Creep is a plastic deformation that is determined by kinetics of the processes occurring on the atomic scale: the glide motion of dislocation lines, their coupled glide and climb, the diffusional flow, the relative displacement of grains by grain boundary sliding, mechanical twinning and so forth. Several creep mechanism has been explored that can contribute to creep. The major creep deformation mechanism such as dislocation creep, diffusional creep, grain boundary sliding can be summarize in a creep deformation map, as shown in Figure 1.10 [19- 23].These deformation map is divided into fields which shows the regions of stress and temperature over which each of the deformation mechanism is dominant. The map is divided into five groups [24].

Ideal Strength

The ideal shear strength defines a stress level which deformation of a perfect crystal ceases to be elastic and becomes catastrophic: the crystal structure become mechanically unstable. Plastic flow occurs when ideal strength is exceeded.

Dislocation Glide Creep

Dislocation glide occurs at high stress level and relatively low temperatures. Dislocations can move by gliding in a slip plane, a process requiring little thermal

activation. This motion is almost always obstacle-limited: it is the interaction of potentially mobile dislocations with other dislocations, with solute or precipitates, with grain boundaries, or with the periodic friction of the lattice itself which determines the rate of flow and the yield strength.

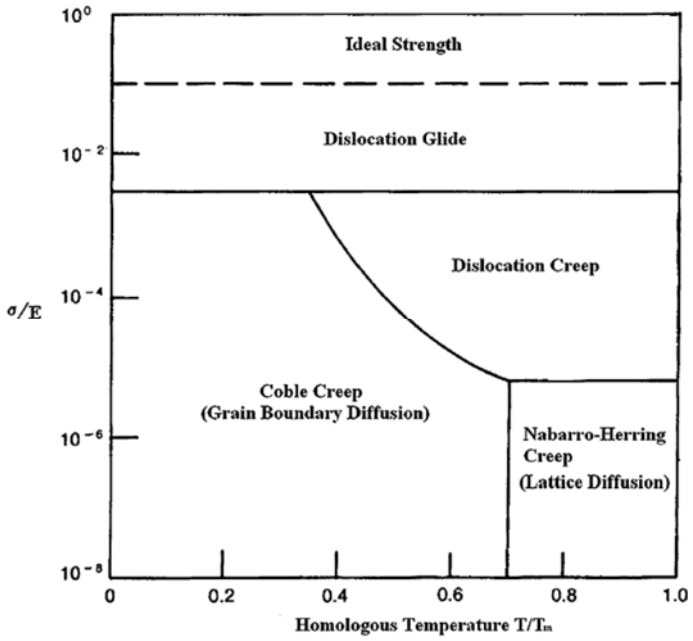

Figure 1.10 Creep Deformation Mechanism [24]

Dislocation Creep

This process occurs at high temperature with homologous temperature greater than 0.5Tm. At high temperatures, dislocations acquire a new degree of freedom: they can climb as well as glide. The rate-determining step for dislocation motion is often a climb process, which requires diffusion and is thus time-dependent and favored by higher temperatures. If a gliding dislocation is held up by discrete obstacles, a little climb may release it, allowing it to glide to the next set of obstacles where the process is repeated.

The glide step is responsible for almost all of the strain, although its average velocity is determined by the climb step. Mechanisms which are based on this climb-plus-glide sequence refer to as climb-controlled creep [19]. Obstacles in the slip plane, such as other dislocations, precipitates or grain boundaries, can lead to such situations.

Grain Boundary Diffusion-Coble Creep

Diffusion creep occurs by transport of material via diffusion of atoms within a grain. It is driven by a gradient of free energy or chemical potential created by the applied stress. If the diffusion paths are predominantly through the grain boundaries, called Coble creep and this deformation favored at low temperature.

Lattice Diffusion-Nabarro-Herring Creep

This is also diffusional creep which is strongly dependent on high temperature. In Nabarro-Herring creep, atoms diffuse through the lattice and the grain becomes larger as the applied stress does work and the process will be faster at high temperatures as there are more vacancies. For diffusion paths through the grains the atoms have a slower jump frequency but more paths.

Grain Boundary Sliding Creep

This deformation occurs at high temperature and contributes significantly in superplasticity. This deformation plays an important role in tertiary creep where it contributes to initiation and propagation of intercrystalline cracks. This process is controlled by the accommodating processes where the sliding surfaces deviates from the perfect plane [21].

So, for the solder alloy, it is believed that dislocation controlled and lattice diffusion controlled creep could be the major deformation mode because of their high homologous temperature.

1.4.4 Fatigue Damage

Solder interconnects in electronic packaging experienced cyclic stress-strain due to mismatch of coefficient of thermal expansion (CTE) between coupled joints. Cyclic temperature changes due to ambient temperature change or the machine goes through on/off cycles. Due to cyclic stress-strain, materials structure break down, finally fracture and this deformation process is called fatigue.

During cycling loading, fatigue failure developed at three stages. First, crack nucleation- cracks initiate at the sites of stress concentration. Secondly, crack propagation along crystal planes with high resolve shear stress or perpendicular to the applied stress. Finally, cracks eventually reaches critical dimension and propagates very rapidly. Fatigue life of a materials define as the number of cycles to fail at specified stress level. The length of a material's fatigue life depends on such factors as surface finish, load amplitude and direction, residual stress, grain size, internal defect distribution, notch sensitivity, geometry and size, as well as temperature and environment.

1.4.5 Shear

Due to temperature variation and CTE mismatch of joined materials, solder joint experienced shear stress. So, the shear properties of the solder alloy such as the shear modulus and shear strength become important.

Similar to tensile stress-strain curve, Hooke's law also holds for the linear elastic behavior in shear:

$$\tau = G\gamma \tag{1.5}$$

where ,G is called the shear modulus of elasticity. The shear modulus is also related to the elastic modulus and Poisson's ratio by the equation:

$$G = \frac{E}{2(1+\nu)} \tag{1.6}$$

The type and magnitude of strains in solder joints under thermal cyclic conditions are often quite complex. For surface mount applications, the strain is nominally in shear. However, tensile and mixed-mode strains can occur owing to bending of the chip carrier or board.

1.4.6 Elastic Anisotropy of Solder Joint

SAC solder joints are mostly composed with Sn and different from the FCC crystal structure of lead, Sn has a tetragonal crystal structure and each grain exhibits highly anisotropic characteristics in its mechanical, thermal and diffusion properties. With the lattice constant of a = b = 5.83A, much larger than that of the c axis, c = 3.18A, as shown in Figure 1.11, the elastic modulus and hardness of Sn are highly dependent on grain orientation [25]. For example, the modulus of elasticity of tin in (001) direction (67.6 GPa) is three times higher than (100) direction (23.6 GPa), Figure 1.12.

The orientation of the anisotropic tin crystal and the intermetallic phases in Sn-based solder alloys play important roles in determining the mechanical behavior and the reliability of a solder joint [26-33]. The mismatch of this orientation leads to the strain gradient and shear cracking of the solder joints. Erince, et.al. [26] reported that thermal

anisotropy of β-tin induced damage in the interfacial cohesive zone elements and formed intergranular fatigue cracks which reduces the thermal fatigue life under thermal cycling. They developed a model based on anisotropy of solder joint to predict the fatigue damage parameters.

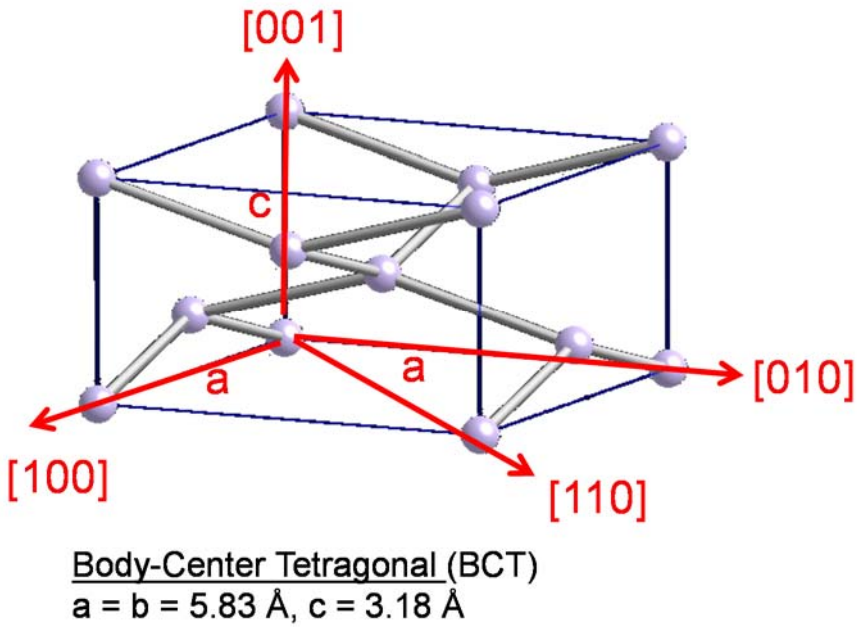

Figure 1.11 Crystal Structure of Tin [25]

Similar study was done by Ubachs, et.al. [27] and confirmed that anisotropy plays in important role in determining the thermal fatigue life of solder joints. They concluded that stress concentrations arise at grain boundaries, dependent on the orientation of the connected grains and their interface. In addition, anisotropy of β-Sn played an important part in strain distributions and the variations of strain in different grains lead to the development of unexpected deformations at the grain-boundary regions. Park, et.al. [28] revealed anisotropic nature of deformations in different grains of the SAC solder.

Ball grid array (BGA) solder joints are mostly multicrystalline with 1-6 grains with different orientations, as shown in Figure 1.13. The majority of the failures in the lead free solder joints occur in the tin phase near an intermetallic interface.

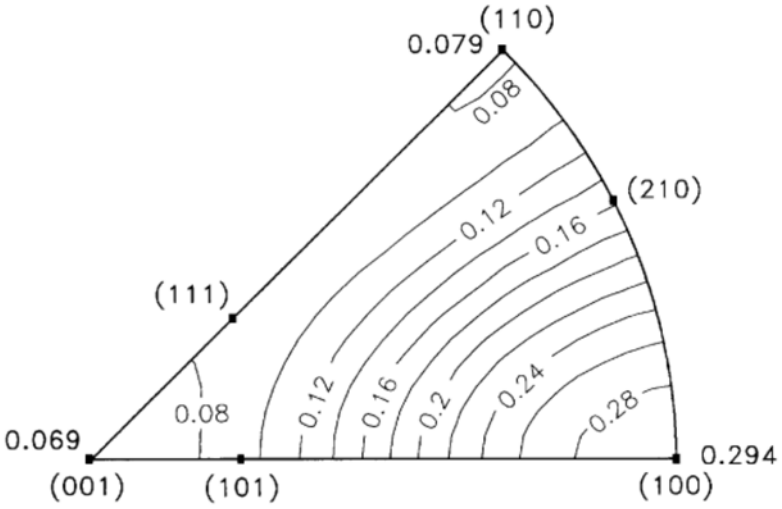

Figure 1.12 Elastic Modulus of β-Tin Crystal as a function of Crystal Orientation [25]

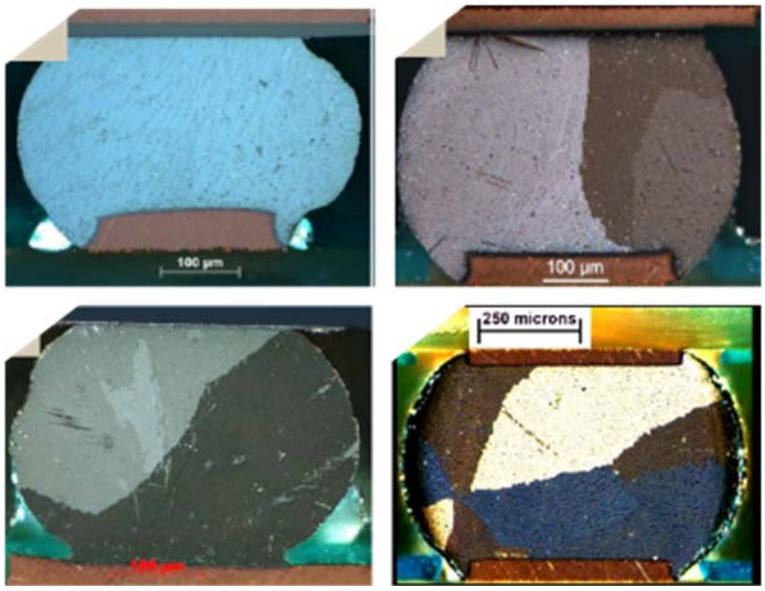

Figure 1.13 Cross-Polarized Image of Single Grain and Multigrain Solder Joints with Different Crystallographic Orientation [31]

Therefore, it is important to understand the crystal orientation dependent nanomechanical properties of the solder joints and to better understand how the damage develops with respect to Sn crystal orientation. Researcher have pointed out to take the effects of anisotropy of β-Sn into consideration as a significant factor in the development of damage and reliability modeling [29-31]. Thus, it is crucial to assess and correlate the orientation and aging induced changes in the mechanical properties of lead free solder joints.

1.4.7 Nanoindentation Technique

Indentation testing is a method that consists essentially of touching the material of interest of whose mechanical properties such as elastic modulus and hardness are unknown with another material whose properties are known. This technique has its origins in Moh's hardness scale of 1822. However, the adoption of Brinell, Knoop, Vickers and Rockwell tests all follow from a refinement of the method of indenting one material with another. Nanoindentation (NI) is a simple indentation testing in which the length scale of the penetration is measured in nanometer. These technique have been motivated by the development of nanostructured materials and miniaturization of engineering and electronic components. In nanoindentation technique the area of contact is determined by measuring the depth of penetration of indenter into the specimen surface. The known geometry of the indenter then allows the size of the area of contact to be determined. Indentation load-displacement data can be used to measure the elastic modulus, hardness, and creep properties [34].

Nanoindentation tests are generally made with either spherical or pyramidal indenters. Diamond is the most frequently used indenter material because of its high

modulus and hardness. The Berkovich triangular pyramidal indenter is preferred over four sided Vickers or Knoop indenter because its edges are more easily constructed to meet a single point.

A recent improvements in nanoindentation testing is the continuous stiffness measurement (CSM) technique. It offers a direct measure of dynamic contact stiffness during the loading portion of an indentation test and, being somewhat insensitive to thermal drift, allows an accurate observation of small volume deformation [35]. The CSM method provides some benefit over conventional nanoindentation technique. For example, it can measure the mechanical properties as a continuous function of distance into the surface and the ability to measure storage and loss modulus of polymer as a function of frequency.

1.5 Objectives of This Research

There have been some limited investigations on the effects of aging on mechanical properties and creep behavior of solder joint arrays. And, there has been little work on aging effects on mechanical properties and creep behavior in individual solder joints. Such knowledge is crucial for the optimizing the design, manufacturing, and reliability of microelectronic packages. Characterization of individual joints is quite challenging because of their extremely small size, and the difficulty in gripping them and applying controlled loadings. In this work, aging phenomena in actual solder joints have been explored by nano-mechanical testing of single lead free solder joints extracted from PBGA assemblies. The following objectives will be achieved in this research:

(1) Characterize the mechanical behavior of SAC solder joints in ball grid array electronic packages using Nanoindentation technique.

(2) Compare mechanical properties and creep behavior of solder joints to the analogous results for bulk solder specimens.

(3) Developed an approach to compare the uniaxial tensile creep strain rate with Nanoindentation.

(4) Characterize the effects of aging on the elastic modulus, hardness, and creep behavior of SAC solder balls.

(5) Correlate the mechanical behavior of solder joints with the measured crystal orientation using EBSD and optical polarize microscope.

(6) Compare the influence of sample dimensions on the measured uniaxial creep response.

(7) Explore the effects of silver content on aging behavior of SACN05 solder joints with N = 1%, 2%, 3% and 4% silver.

(8) Examine the ability of dopants to reduce aging effects in joints by testing of different sets of doped/non-doped alloys.

(9) Use synchrotron X-ray microdiffraction technique on the 12.3.2 beamline at Advanced Light Source (ALS)/Lawrence Berkeley National Laboratory (LBNL) to study the changes in grain orientation and distribution, grain growth, rotation and sub-grain formation and residual strain magnitudes that occur in small lead free solder joints subjected isothermal aging.

1.6 Organization of the Dissertation

This dissertation is divided into following chapters:

Chapter 1: Introduction to lead free solder alloys and basic mechanical properties of solder alloys.

Chapter 2: Literature review on isothermal aging effects on solder alloy mechanical properties and microstructure evolution, Nanoindentation to study solder alloy, micro-alloy to modify lead free solder microstructure and x-ray microdiffraction to characterize solder joints.

Chapter 3: Description of the experimental procedure, sample preparation, uniaxial and Nanoindentation creep data processing and X-ray microdiffraction test procedure.

Chapter 4: Characterization of SAC305 solder joints and prediction of uniaxial creep using nanoindentation creep.

Chapter 5: Characterization of aging effects in SAC305 solder joints.

Chapter 6: The effects of silver content on the aging resistance of SAC solder joints.

Chapter 7: Reduction of aging effects using microalloy additions.

Chapter 8: Study of aging effects in lead free solder joints using synchrotron x-ray microdiffraction.

Chapter 9: Summary and Conclusions.

Chapter 10: Future works

CHAPTER 2

LITERATURE REVIEW

2.1 Introduction

The ongoing transition to lead free soldering has been motivated by environmental concerns, legislative mandates, and market differentiation. Although no clear solution has been identified for all applications; Sn-Ag, Sn-Ag-Cu (SAC), and other alloys involving elements such as Sn, Ag, Cu, Bi, In, and Zn have been identified as potential replacements for standard 63Sn-37Pb eutectic solder. Although, there is a large discrepancies in mechanical properties of solder alloy, one critical factor has been neglected in most literature is isothermal aging. In real life operation environment, many electronics exposed to high temperature and stress levels. These challenges pushed the increased reliability of all electronic systems, motivate continuously investigate of aging effects in lead free solder alloy. The mechanical properties of a lead free solder are strongly influenced by its microstructure, which is controlled by its thermal history including solidification rate and thermal aging after solidification. Due to aging phenomena, the microstructure, mechanical response, and failure behavior of lead free solder joints in electronic assemblies are constantly evolving when exposed to isothermal aging and/or thermal cycling environments. Such aging effects are greatly exacerbated at higher temperatures typical of thermal cycling qualification tests. However, significant changes occur even with aging at room temperature. Solder joint fatigue is one of the predominant failure mechanisms in

lead free electronic assemblies exposed to thermal cycling. Thus, accurate mechanical properties and constitutive equations for solder materials are needed for use in mechanical design, reliability assessment, and process optimization.

However, significant changes occur even with aging at room temperature. Solder joint fatigue is one of the predominant failure mechanisms in lead free electronic assemblies exposed to thermal cycling. Thus, accurate mechanical properties and constitutive equations for solder materials are needed for use in mechanical design, reliability assessment, and process optimization.

2.2 Aging Effects on Material Properties

The effects of aging on the constitutive and failure behavior of lead free solder has been extensively investigated by the authors. Medvedev, et al. [36] observed a 30 % loss of tensile strength for bulk Sn/Pb solder stored for 450 days at room temperature while 4-23% loss of tensile strength for solder joints subjected to room temperature storage for 280-435 days. Lampe, et al. [37] observed the similar behavior and found losses in shear strength and hardness of up to 20 % in Sn-Pb and Sn-Pb-Sb solder alloys stored for 30 days at room temperature.

The effects of room temperature aging on the mechanical properties and creep behavior of SAC alloys have been extensively studied by Ma, et al. [38-39]. The measured stress-strain data demonstrated large reductions in stiffness, yield stress, ultimate strength, and strain to failure (up to 40 %) during the first 6 months after reflow solidification. In addition, even more dramatic evolution was observed in the creep response of aged solders, where up to 100X increases were found in the steady state creep strain rate of lead free solders that were simply allowed to sit in a room temperature environment. In addition,

Ding, et al. [40] explored the evolution of fracture behavior of Sn-Pb tensile samples with elevated temperature aging while Zhang, et al. [41] have shown that prior aging cause's large reductions in the reliability of BGA test assemblies subjected thermal cycling accelerated life testing. The same author also systematically studied the effects of aging on SAC alloy composition and found degradation in tensile properties with aging [42-43]. Xiao and Armstrong, et al. [44-45] recorded stress-strain curves for SAC396 specimens subjected to various durations of room temperature aging, and found losses of ultimate tensile strength of up to 25 %.

Several studies have also documented the degradation of Sn-Pb and SAC solder ball shear strength in area array packages subjected to room temperature aging. Chen, et al. [46] have studied the Sn-Pb and Sn-3.5Ag solders and measured the variations in solder bump shear strength with aging. They concluded that shear strength for both solder materials decreases slightly after aging at 150 % for 1500 hours, 8.9 % for Sn-Pb solder bumps and 5.3 % for Sn-3.5Ag. Anderson, et al. [47] measured significant hardness losses and microstructural coarsening for Sn-Pb, Sn-Ag, and Sn-Zn eutectic solders stored at 25 C for 1000 hours.

The effects of aging at elevated temperature have been studied widely due to the drastic changes in the microstructure and mechanical properties. Mustafa, et al. [48] have studied the aging-induced changes occurring in the cyclic stress-strain behavior of lead free SAC solders for both tension/compression and shear loadings. Using the developed approaches, the influence of aging on the fatigue life of lead free alloys was also examined [49]. Motalab, et al. [50] have included aging effects in the Anand constitutive model and energy density based failure criterion for SAC solders, and then used these theories with

finite element analyses to predict the thermal cycling life of aged BGA assemblies. Good correlations were achieved with the measured lifetimes from references [42]. Lall and coworkers, et al. [51] have investigated changes in the high strain rate behavior of SAC solders subjected to aging.

There have been limited prior mechanical loading studies on aging effects in actual solder joints extracted from area array assemblies (e.g. PBGA or flip chip). This is due to the extremely small size of the individual joints, and the difficulty in gripping them and applying controlled loadings (tension, compression, or shear). Pang, et al. [52] have measured microstructure changes, intermetallic layer growth, and shear strength degradation in custom SAC single ball joint lap shear specimens subjected to elevated temperature aging. Darveaux, et al. [53] performed an extensive experimental study on the stress-strain and creep behavior of solder using specially constructed double lap shear specimens with a 10 x 10 area array solder balls. He found that aging for 1 day at 125 C caused significant effects on the stress-strain and creep behavior. For example, aged specimens were found to creep much faster than non-aged specimens by a factor of up to 20 times for both SAC305 and SAC405 solder alloys. Wiese, et al. [54] also studied the effects of aging on solder joint creep using custom assemblies with 4 flip chip solder balls, and found highly accelerated creep rates after aging at 125 C. Dutta and coworkers, et al. [55] used an impression creep technique with a cylindrical punch to study creep in PBGA solder balls that had been subjected to thermal-mechanical cycling. Similar aging induced degradation in creep properties were also reported in bulk samples by Chavali, et al. [56]. Mysore, et al. [57], also recorded the aging induced degradations in creep properties in bulk samples.

Isothermal aging also leads to phase coarsening of both β-Sn and precipitates, the dispensing and coalescing of IMC particles, as well as the accelerated growth of grains, and the interfacial IMC thickness between Cu trace and bulk solder joints. Fix, et al. [58] investigated phase coarsening in SAC alloy and suggested a Sn diffusion controlled process for 175 C aging (Figure 2.1).

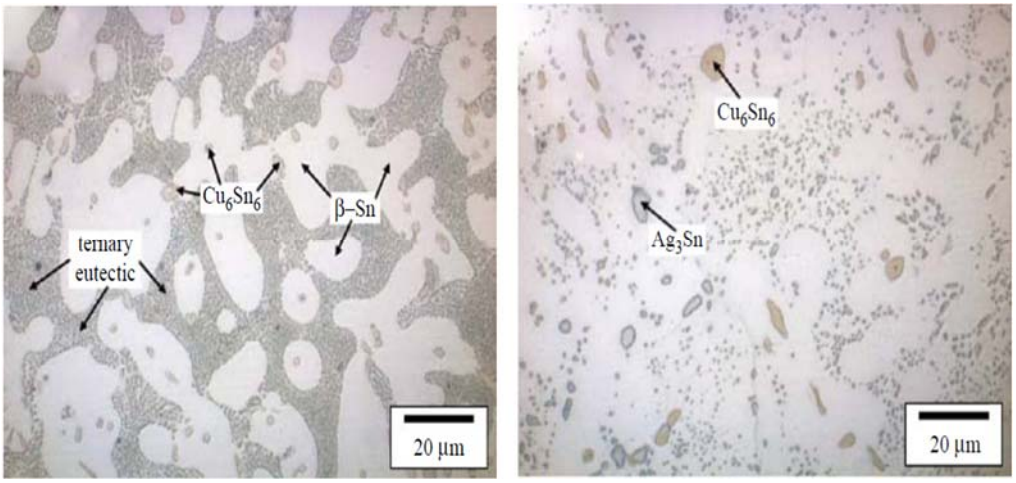

Figure 2.1 Microstructure Evolution of SAC405 Solder Joints [58]

Xiao, et al. [45] have studied the aging effects on dispensing and coalescing IMC phase growth with aging in bulk SAC396 samples (Figure 2.2) and Pang, et al. [52] graphed the IMC in the interfacial region after aging at 100-150 C for up to 1000 hrs (Figure 2.3).

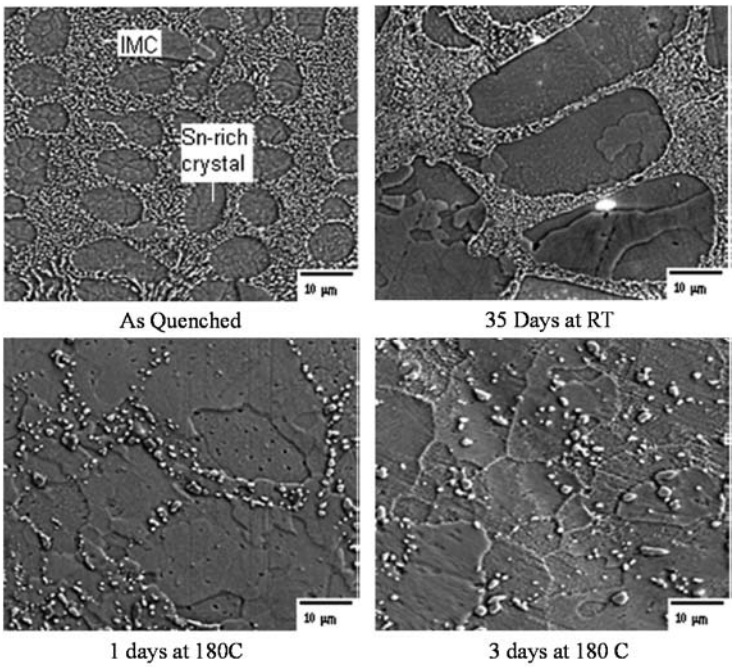

Figure 2.2 SEM Micrograph of As-Aged SAC396 Samples [45]

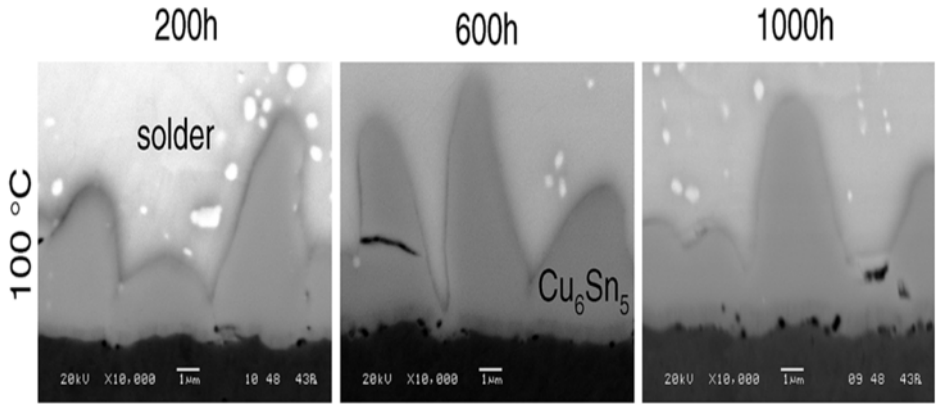

Figure 2.3 Evolution of IMC with Aging [52]

2.3 Nanoindentation to Study Solder Alloy

Nanoindentation techniques have been widely used to probe the mechanical properties and deformation behavior of extremely small material samples. Over the past

decade, it has been applied by several investigators to characterize lead free solder joints and intermetallic compounds (IMC) in lead free solder joints [59-73]. In early studies by Rhee, et al. [59-60], Chromik, et al. [61], and Deng and coworkers, et al. [62-63], the elastic modulus E and hardness H of various regions in Sn-Ag and SAC lead free solder joints were explored by nanoindentation. In particular, the properties for the Sn-rich phase (β-tin) and the eutectic phase (containing β-tin and a mix of Sn-Ag and Sn-Cu intermetallics) were explored. Attempts were also made to indent individual Sn-Ag and Sn-Cu intermetallic particles [61-63], and then to compare the properties of the IMCs to those for the solder joint phases. Rhee, et al. [59] also measured changes in the mechanical properties after the joints were subjected to thermal-mechanical cycling.

Gao, et al. [64-65] have used nanoindentation to characterize the effects of loading rate on the modulus and hardness of Sn-Ag lead free solders. They also performed creep experiments for two different microstructures (bulk cast and reflowed), and examined the effects of elevated temperature aging on the hardness. Indentation experiments with a heated stage to control the solder sample temperature have been performed by Sun, et al. [66], Liu, et al. [67], Gao, et al. [68], and Han and coworkers, et al. [69]. The alloys tested in these studies included SAC387, 80Au-20Sn, SAC305, and SAC357, respectively. In all of these investigations, the temperature dependencies of the mechanical properties (E, H) of the solder matrix or individual solder phases were characterized. In addition, the sensitivity of the creep response of lead free solder to temperature has also been examined [69]. Han, et al. [70] have studied the indentation size effect on the creep behavior of SAC357 lead free solder.

The effect of thermal aging on the mechanical properties of intermetallic compounds at SAC solder joint interfaces have been explored using nanoindentation by Xu and Pang, et al. [71-72] and Song, et al. [73]. Significant drops in both the modulus and hardness were recorded for aged samples relative to non-aged samples. Xu and Pang, et al. [71] also characterized the mechanical properties of the various phases and IMCs in a SAC387 solder joint. Venkatadri, et al. [74] have studied the effects of aging on lead free solder joints using a micro-hardness test to perform single indents on joints.

2.4 Dopants to Mitigate the Aging Effects

The mechanical behavior and reliability of solder materials can be greatly influenced by the addition of micoalloying elements (dopants) such as Ni, Bi, In, Mn, etc. Addition of small quantities of these elements to the solder alloy can modify its microstructure, alter its bulk alloy characteristics, increase the volume fraction of eutectic phases, and alter the crack pattern to improve the drop and shock reliability performance. It can also enhance the interfacial IMC layer properties by improving their ductility and toughness.

Mu, et al. [75-76] found that addition of Ni reduce the creep of Cu_6Sn_5 which play a determinant role in the overall deformation of solder joint. It is also found that addition of Ni reduce the thermal expansion of IMC and stabilize the hexagonal IMC down to room temperature [77]. Furthermore, the solubility of Ni modifies the growth texture of IMC [78].

El-Daly, et al. [79-80] and Hammad, et al. [81] also observed improved creep resistance in SAC alloys doped with Ni, Sb and Zn. They concluded that addition of these doped alloy refine the microstructure, lower the precipitate coarsening thus increase the

resistance to dislocation movement and dislocation pile up in the adjacent β-Sn grains which improves the creep properties (Figure 2.4).

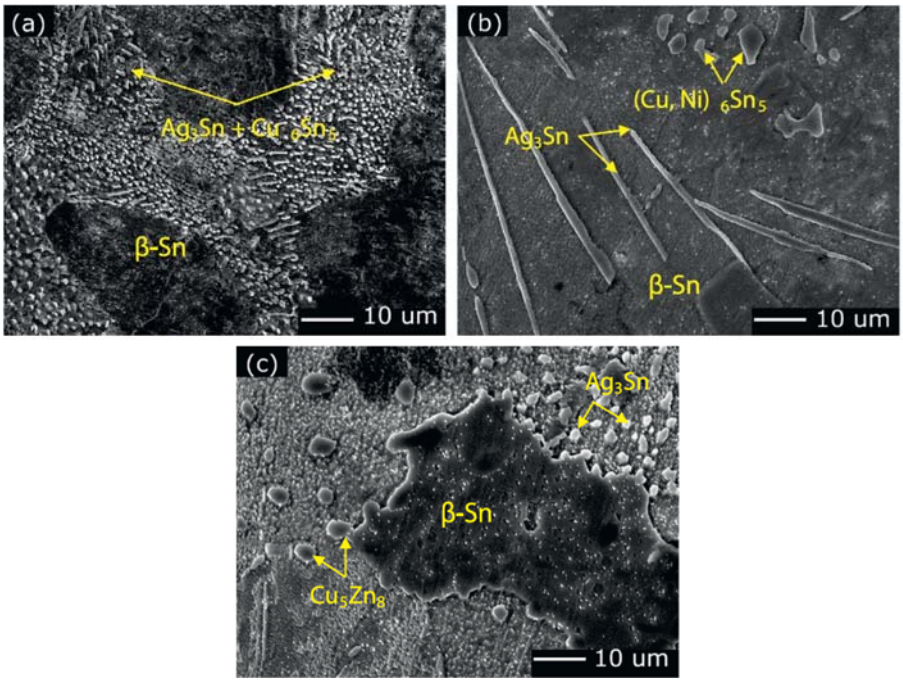

Figure 2.4 SEM Microstructure of (a) SAC205 (b) SAC205+Ni and (c) SAC205+Sb [80]

Witkin, et al. [82] have found that aging has minimal effect on creep of Bi containing solder because aging has minimal effect on activation energy of SACBi solders. They also concluded that Bi particles are precipitating at the boundary of the SAC solder which can be attributed to combination of solid solution and particle strengthening. As aging leads to coarsening of Ag_3Sn particles but redistribution of Bi particles results in fine dispersion of Bi throughout the interior of the grain and grain boundary which diminish the loss of particle reinforced eutectic region. It was also found that addition of Bi can decrease the growth of IMC which can possibly inhibit the Sn diffusion along the grain boundary.

Mukerjee, et al. [83] have studied the effects of adding Mn on the viscoplastic behavior of SAC solders. They found that addition of 0.05 wt-% Mn to SAC105 improved its creep resistance by one-two orders of magnitude. Doping with manganese has also been shown to improve drop impact reliability [84-85].

Sweatman, et al. [86] and Coyle and coworkers, et al. [87] observed increased board level reliability for certain components when using SAC105 doped with Ni and Mn.

2.5 Effects of Grain Orientation on Mechanical Response

The crystal orientation of tin phase in lead free solder has significant effect on mechanical properties, stress state as well as the reliability of solder joints. Zamiri, et.al. [32], investigated that difference in crystal orientation led to different in mechanical properties. They also confirmed that internal energy of the system is also a function of tin crystal orientation. Traditionally, electron backscattering diffraction (EBSD) method more commonly used to determine the grain orientation of the solder material. Jing, et al. [33], performed EBSD measurement on individual solder joint and confirmed that anisotropy of tin and the resulting stress concentration significantly damage the fatigue life of individual solder joint. Similar study was done by Bieler, et al. [29]. They performed EBSD study on different solder joints and showed a variety of grain orientation which caused non-uniform stress from joint to joint. For example, solder balls with x-axis parallel to pad surface, crack happens and propagate after thermal cycling, as shown in Figure 2.5. This findings also illustrated a correlation between damage in the solder balls with tin grain orientation. And Nanoindentation technique has been routinely used to measure the mechanical properties of solder joint. So, the combination of the nanoindentation and EBSD measurements provides a better understanding of relationship between grain orientation

and mechanical behaviors. Villain, et al. [30], have used the EBSD and Nanoindentation to identify the grain orientation and hardness of solder joints. Their results indicated that solder joint with different orientation had different hardness value and reliability data.

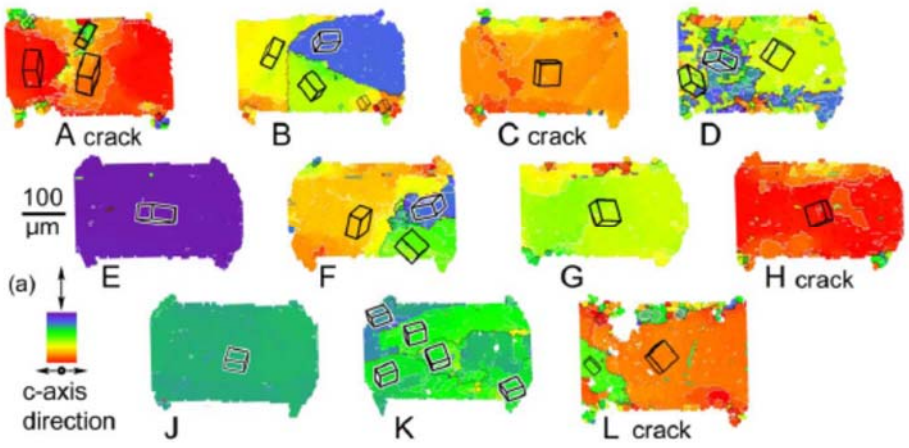

Figure 2.5 Crystal Orientation Maps of Different Joints from a Row in a Package [29]

2.6 Comparison of Nanoindentation Creep with Uniaxial Creep

Several attempts have been made to directly correlate the nanoindentation creep results with those from convention creep such as uniaxial creep. Goodall and Clyne, et al. [88] reported a poor correlation between nanoindentation data with the conventional creep reported in the literature. Poisl, et al. [89] made an effort to correlate the indentation strain rate with the effective strain experienced by the material under the indenter. Lucas and Oliver, et al. [90] carried out nanoindentation creep on indium and observed a stress exponent value of 5 which is similar to reported in uniaxial creep. The magnitude of the two creep strain rates differ greatly and no reason for this was given.

Wang, et al. [91] made an effort to directly compare the nanoindentation creep with the uniaxial creep. There appears to be a large discrepancy between the two creep strain rates.

2.7 Summary and Discussion

In this chapter an extensive review has been discussed on four major area including solder material characterization including aging effects, micro alloy addition, Nanoindentation to study solder materials and x-ray microdiffraction.

Aging is perhaps the main cause of the discrepancies in the mechanical property databases for soldering materials. A number of studies on aging effects in lead free solder materials have been performed over the last couple of years. These investigations have quantified the large changes that occur in the mechanical (constitutive) response and failure behavior of lead free solders after exposure to isothermal aging. The mechanical behavior of Sn-Ag-Cu (SAC) lead free solders degrade significantly during room temperature and elevated temperature aging. For example, measured stress-strain data illustrate large reductions in stiffness, yield stress, ultimate strength, and strain to failure (up to 50%) during the first 6 months after reflow solidification. Even more dramatic evolution was observed in the creep response of aged solders, where up to 10,000X increases were found in the steady state (secondary) creep strain rate (creep compliance) of lead free solders that were observed for SAC solders subjected to elevated temperature aging at 125 C. It was also shown that aging induces reductions in the fatigue life of lead free solder materials. Aging has also been reported to coarsening the microstructure and increase the IMC thickness.

It has been shown that shown that addition of the microalloy elements significantly reduced the aging degradations of the mechanical properties and creep resistance in the joints. The possible candidates of the X-additive include Bi, Zn, Co, Ni, Mn, Cr, Ge, Ti, Si, B, Al, In, etc. It has been demonstrated that addition of micro alloys will not only refine the grains structure and IMC particles but also control the growth of interfacial IMC layers.

CHAPTER 3

SAMPLE PREPARATION AND EXPERIMENTAL PROCEDURE

3.1 Introduction

In this chapter, sample preparation and testing procedure has been presented. Lead free solder joints were extracted from PBGA assemblies (Amkor CABGA, 14 x 14 mm, 192 balls, 0.8 mm ball pitch, 0.46 mm ball diameter). Using nanoindentation techniques, the stress-strain and creep behavior of the SAC solder materials have been explored at the joint scale for various aging conditions. Due to the variety of crystal orientations realized during solidification, it was important to identify the grain structure and crystal orientations in the tested joints. Polarized light microscopy and Electron Back Scattered Diffraction (EBSD) techniques have been utilized for this purpose. In addition, an approach has been developed to predict tensile creep strain rates for low stress levels using nanoindentation creep data measured at very high compressive stress levels.

Along with the actual solder joints, a novel specimen preparation procedure was developed where solder uniaxial test specimens were formed in high precision rectangular cross-section glass tubes using a vacuum suction process. For the current work, uniaxial creep samples with nominal dimensions of 10 (length) x 3 (width) x 0.5 (height) mm and 10 (length) x 1 (width) x 0.5 (height) mm were utilized. Microstructural analysis was conducted using Scanning Electron Microscope (SEM). Finally, x-ray microdiffraction

technique at the Advanced Light Source (Synchrotron) at Lawrence Berkeley National Laboratory was employed to characterize several joints after various aging exposures.

3.2 Solder Joint Samples and Polishing Procedure

The lead free solder joints in this study were extracted from PBGA assemblies (Amkor CABGA, 14 x 14 mm, 192 balls, 0.8 mm ball pitch, 0.46 mm ball diameter). The test boards were assembled as part of the iNEMI Characterization of Pb-Free Alloy Alternatives Project [92-93], and a variety of samples with 10 different solder ball alloys are being studied and listed in Table 3.1.

Table 3.1 BGA Alloys (SAC and SAC+X)

No.	BGA Ball Alloy (Standard)
1	Sn-0.3Ag-0.7Cu (SAC0307)
2	Sn-1.0Ag-0.5Cu (SAC105)
3	Sn-2.0Ag-0.5Cu (SAC205)
4	Sn-3.0Ag-0.5Cu (SAC305)
5	Sn-4.0Ag-0.5Cu (SAC405)
No.	BGA Ball Alloy (Doped)
6	Sn-1.0Ag-0.5Cu-0.05Ni (SAC105+Ni)
7	Sn-1.0Ag-0.5Cu-0.03Mn (SAC105+Mn)
8	Sn-2.0Ag-0.5Cu-0.05Ni (SAC205+Ni)
9	Sn-0.3Ag-0.7Cu +Bi (SACX0307)
10	Sn-0.7Cu+0.05Ni+Ge (SN100C)

These joints were extracted from test boards where the original components had SAC305 solder balls, the bare test boards had ENIG surface finish, and where SAC305 solder paste was used in the surface mount assembly process. The assembled PBGA components were cut out from the test boards and then cross-sectioned into samples of solder joints from each alloy. The samples were then mounted in a prepared conductive epoxy resin stub. Details of the sample preparation process include mechanical grinding

and polishing of the actual solder joints with several silicon carbide (SiC) papers with grit size of 320, 400, 600, 800 and 1200. The polishing process was performed on a rotating metallographic disc which is shown in Figure 3.1. Final polishing was done by 1 μm diamond paste followed by 0.05 μm colloidal silica suspensions. Finally, the sample surface was cleaned with distilled water and compressed air. This resulted in mirror finish samples suitable for nanoindentation tests, SEM microscopy and EBSD test, as shown in Figure 3.2.

3.3 Nanoindentation System and Test Procedures

The nanoindentation tests were conducted using an instrumented MTS Nanoindenter XP system with a Berkovich tip indenter, shown in Figure 3.3. The load versus indentation displacement normal to the cross-section surface was measured during each indentation experiment, and the elastic modulus could then be extracted using the approach proposed by Oliver and Pharr, et al. [94-95] to process the measured slope of the load-displacement curve in the unloading phase (See Figure 3.4). In addition, the Continuous Stiffness Measurement (CSM) technique was also used in all experiments to extract elastic modulus and hardness as a function of the distance from the surface (indentation depth).

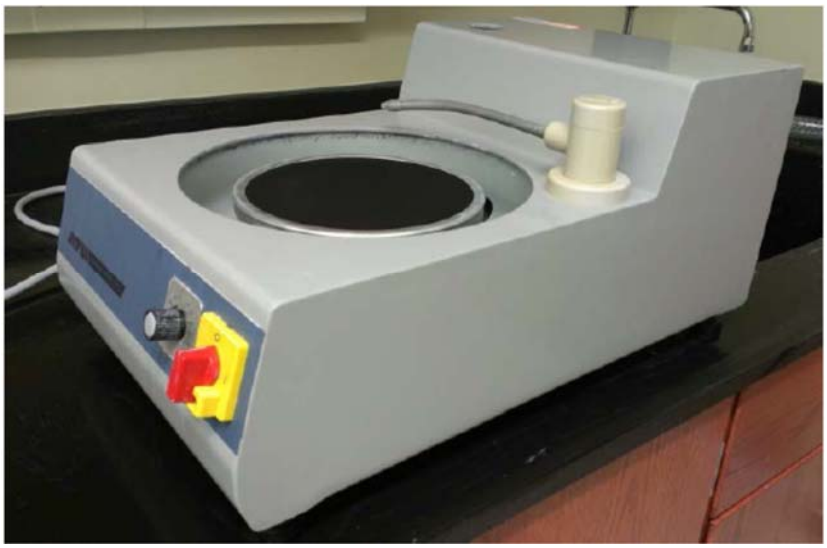

Figure 3.1 Nanoindentation and Microscopy Sample Preparation Machine

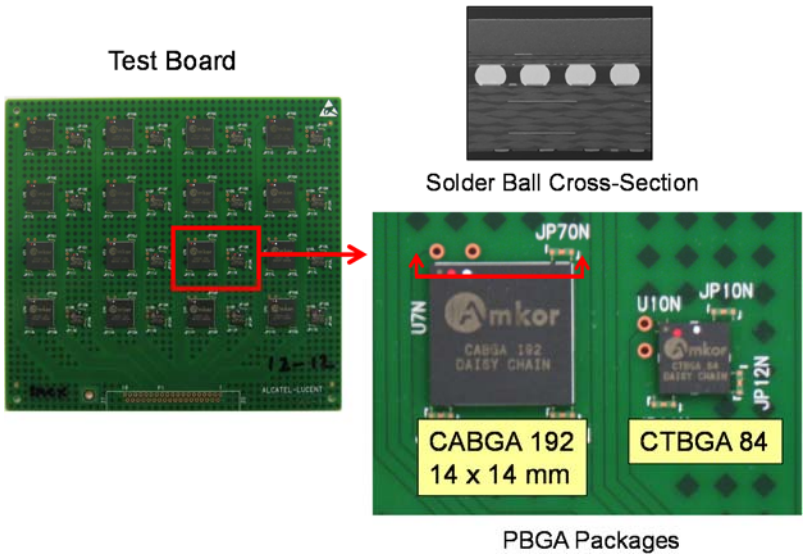

Figure 3.2 iNEMI Test Board and Solder Alloy

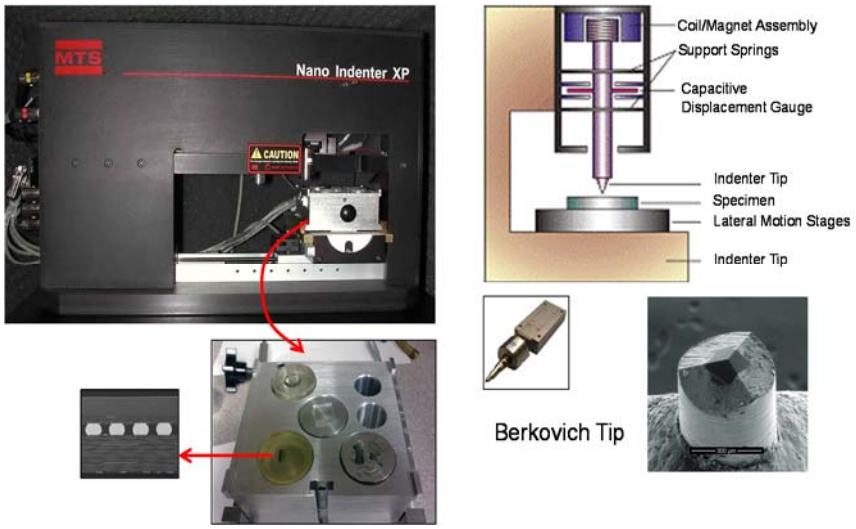

Figure 3.3 MTS Nanoindentation System

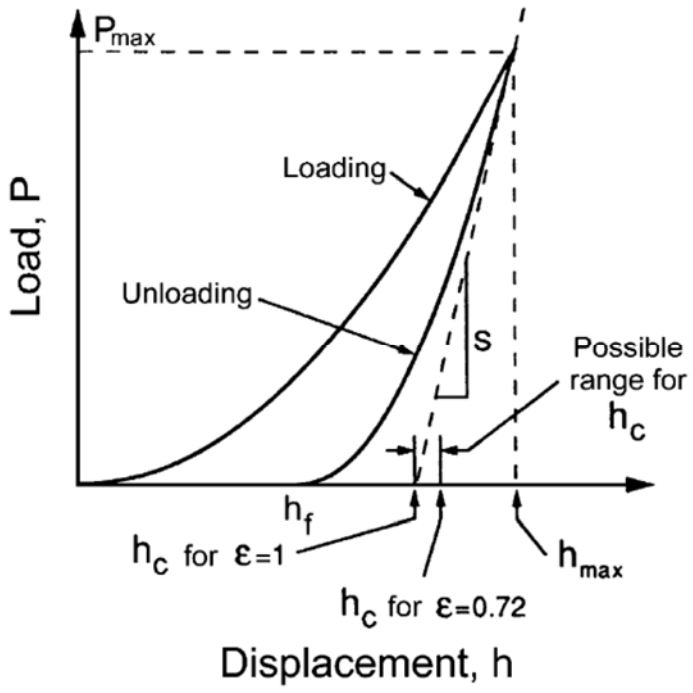

Figure 3.4 Load-Displacement Curve in Unloading Phase (h_c is Contact Impression and ε is Geometric Constant) [94]

A typical cross-sectioned lead free solder ball sample after nanoindentation testing is shown in Figure 3.5, and a close-up view of an example permanent indentation mark is

shown in Figure 3.6. For each set of experimental test conditions, an array of several indents were made (e.g. 2 x 3 array as shown in Figure 3.5), and the individual indent test values were averaged to obtain statistically relevant results and consistency of inspection. All tests were performed on single grain (Sn crystal) solder balls, so that there were no orientation effects caused by an indentation array covering two or more grain boundaries of grains with significantly different crystal orientation (different material properties). A maximum load of 30 mN was selected for the tests so that the indentation marks were large enough to cover all the phases of solder material (see Figure 3.6). Thus, the nanoindentation tests characterized the global mechanical properties of the solder joints, rather than the localized properties in the β-Sn phases (Sn-rich dendrites) or in the eutectic phases between dendrites that contain Sn-Ag and Sn-Cu intermetallics. Indentation experiments were conducted at constant indentation displacement rate of 10 nm/sec, corresponding to an effective strain rate of 0.05 sec^{-1}. Calibration of the load and hardness measurements was performed on fused silica.

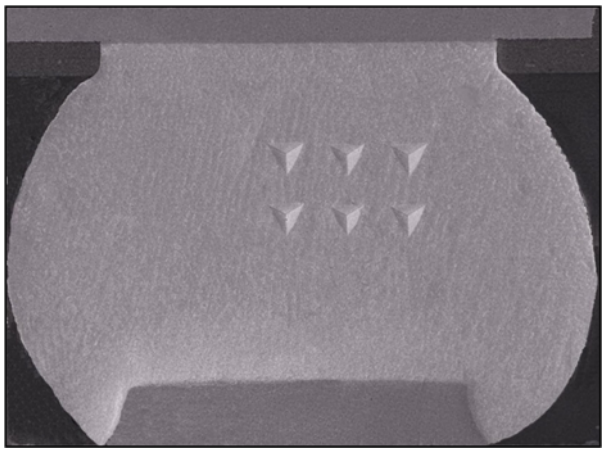

Figure 3.5 Solder Ball after Nanoindentation System

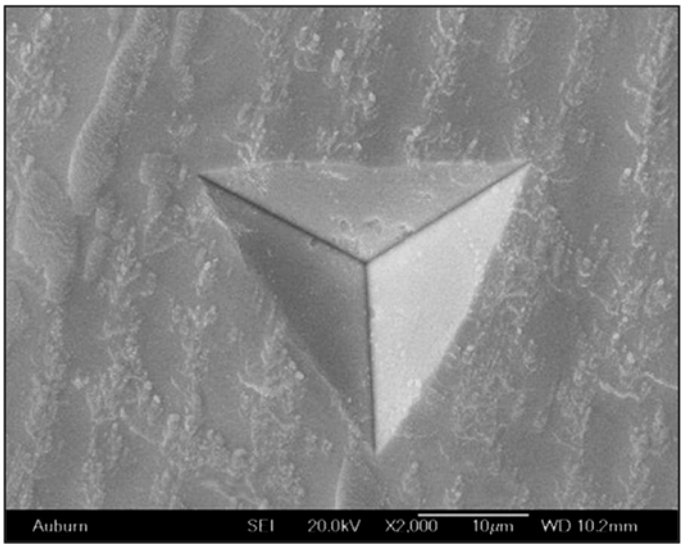

Figure 3.6 Permanent Indentation after Testing

Indentation creep tests were performed holding the load constant at its maximum value of 30 mN for 500-1000 sec. After this dwell, the sample was unloaded at the same 10 nm/sec displacement rate used during loading. There was also a holding period of 60 sec after 90% unloading to allow for thermal drift correction. In our work, the thermal drifts were kept smaller than 0.05 nm/sec, and the thermal drift effects were excluded from the resulting displacement data.

3.4 Indentation Procedure for Lead Free Solder Joints

Measurement of Elastic Modulus and Hardness

A typical nanoindentation load versus displacement (P vs. h) curve for one of the SAC305 solder joint samples is shown in Figure 3.7. During indentation, continuous load-displacement data are recorded. The measured response consists of three segments: (1) loading at constant deformation rate (10 nm/sec) to the indentation force reaches its prescribed maximum value of 30 mN; (2) dwell (creep) for 900 sec at maximum load of

30 mN; and (3) unloading at the same constant deformation rate (10 nm/sec). The loading curve is a function of loading rate. The slope S = dP/dh of the unloading region at maximum load is called the unloading stiffness, and can be used to calculate the elastic modulus E and hardness H at the point of maximum indentation using the Oliver and Pharr method [94-95]. In addition to S, the procedures to calculate E and H (see below) require the values of P_{max}, h_{max}, ν (Poisson's ration of the indented material), and several geometrical parameters and materials constants for the indentor tip.

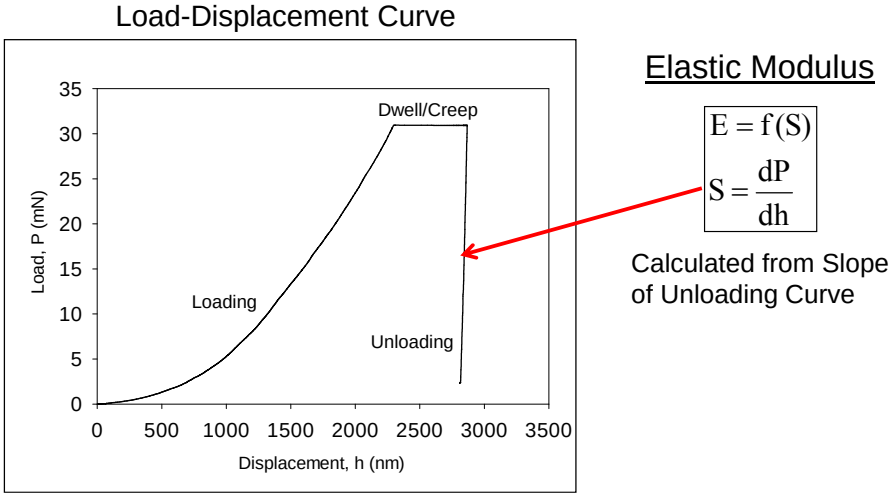

Figure 3.7 Typical Nanoindentation Load-Displacement Curve for Solder Material

In nanoindentation testing, the hardness (Meyer hardness) H is defined as maximum load divided by projected contact area A of the indentation at maximum load:

$$H = \frac{P_{max}}{A} \tag{3.1}$$

The hardness is thought of as a material flow resistance or resistance to plastic deformation. For many metals, the hardness and yield stress can be related by the approximation:

$$H \approx 3\sigma_Y \quad \text{or} \quad \sigma_Y \approx \frac{H}{3} \tag{3.2}$$

This empirical expression is often referred to as the Tabor relationship [96-97].

For the Berkovich indentor tip used in the work, the projected contact area at maximum load is given by:

$$A = 24.5h_c^2 + Ch_c \tag{3.3}$$

where h_c is the vertical distance in which the contact is made, and C is a geometrical factor that is approximately 150 nm [35]. The distance h_c can be related to the measured indentation displacement using theory of elasticity based contact mechanics:

$$h_c = h_{max} - h_s = h_{max} - \varepsilon\frac{P_{max}}{S} \tag{3.4}$$

where h_{max} is the measured maximum indentation displacement from the P vs. h curve, h_s is the displacement of the surface of the material at the perimeter of the indentor contact, and ε is a geometrical constant for the Berkovich indentor tip [94]. Combining equation (3.1, 3.3 and 3.4), the hardness H and projected contact area A can be related to P_{max}, h_{max}, and S measured from the nanoindentation P vs. h curve. Equation (3.2) can then be used to estimate the yield stress of the indented material from the measured hardness.

Using the assumption that the contact area remains constant during withdrawal of the indentor tip and theory of elasticity solutions for contact of a material with a rigid punch, it can be established that the unloading stiffness from the recorded nanoindentation curve is given by:

$$S = \frac{dP}{dh} = \frac{2\beta\sqrt{A}}{\sqrt{\pi}}E_r \quad \text{or} \quad \frac{1}{E_r} = \frac{2\beta\sqrt{A}}{\sqrt{\pi}S} \tag{3.5}$$

where, $\beta \approx 1$ is a geometrical factor for the chosen indentor tip and E_r is the reduced modulus [34-35]. The desired elastic modulus E of the material being indented is related to the reduced modulus, E_r using following equation:

$$E = \frac{1 - \nu^2}{\left[\frac{1}{E_r}\right] - \left[\frac{1 - \nu_i^2}{E_i}\right]} \tag{3.6}$$

where, ν is the Poisson's ratio of the indented material (usually assumed to be 0.3 if unknown), ν_i is the known Poisson's ratio of the indentor tip material, and E_i is the known elastic modulus of the indentor tip material [94-95]. Combining equation (3.3 – 3.6), the elastic modulus E can be related to P_{max}, h_{max}, and S measured from the nanoindentation P vs. h curve.

In the Continuous Stiffness Measurement (CSM) method, the procedure above is modified by measuring the unloading stiffness dP/dh continuously along the load-displacement nanoindentation curve (P vs h curve). This is accomplished by superimposing a small harmonic oscillating force on top of the normal force vs. time curve obtained by application of the constant indentation rate [35, 95], as shown in Figure 3.8. The value of S in this case is:

$$S = \frac{dP}{dh} = \left[\frac{1}{\frac{P_{os}}{h(\omega)}\cos\phi - (K_s - m\omega^2)} - K_f^{-1} \right] \tag{3.7}$$

where, P_{os} is the peak value of the applied harmonic force with frequency ω, $h(\omega)$ is the magnitude of the indenter displacement when the harmonic force is applied, ϕ is the phase angle between the force and displacement, m is the mass of indenter, K_s is the spring constant of leaf spring supporting indenter, and K_f is stiffness of the indenter [35, 94]. The

values of E and H can then be evaluated continuously as a function of the indentation depth h during the nanoindentation test by using equation (3.1 - 3.6) and the values of dP/dh, P, h recorded at each point along the nanoindentation curve.

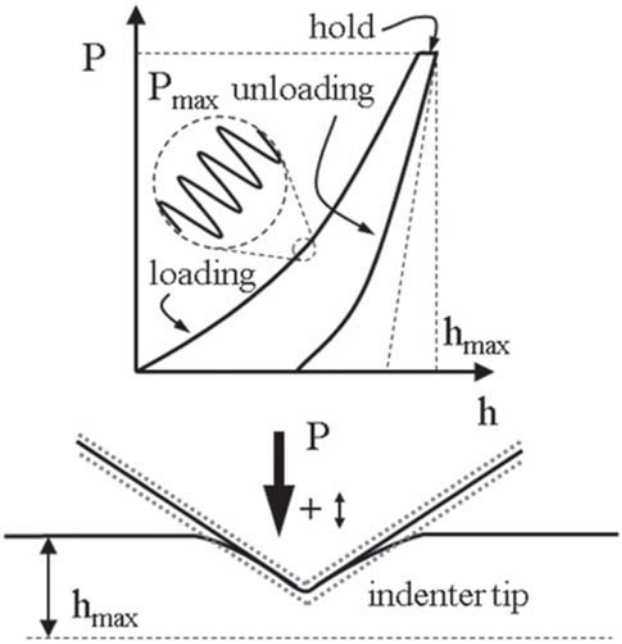

Figure 3.8 Continuous Stiffness Measurement System [35]

3.5 Aging Studies on SAC Solder Joints

Aging phenomena in doped and non-doped lead free solder joints have been explored by nanomechanical testing. The solder joints were exposed to various aging conditions prior to testing. The SAC alloys considered were from BGA components fabricated using 10 different SAC alloys. Using the nanoindentation techniques detailed above, the stress-strain and creep behavior of the standard (non-doped) and doped SAC solder joints have been explored for various aging conditions. Mechanical properties characterized as a function of aging include the elastic modulus and hardness, as well as

the creep strain rate vs. applied stress response. With these approaches, aging effects in solder joints were quantified and correlated to the magnitudes of those observed in stress-strain and creep testing of miniature bulk specimens with hundreds of grains performed in prior studies [38-43]. In addition, new creep experiments with aging have been performed on very small tensile specimens (SAC105 and SAC305) with approximately 10 grains, and these data have also been correlated with the nanoindentation results.

The SACN05 lead free solder joints in this study are composed of 95+% Sn. Thus, the properties of Sn dominate the behavior of these alloys. Sn has a Body-Center Tetragonal (BCT) crystal structure, and each grain exhibits highly anisotropic characteristics in its mechanical, thermal, and diffusion properties. The Sn grain/crystal orientations and the intermetallic phases present in a solder joint will play important roles in determining its mechanical behavior and the reliability. Due to the highly anisotropic nature of Sn crystals, a variety of mechanical properties can be found in a single joint that contains multiple grains. To avoid having the nanoindentation results vary across a solder joint when making several indents under the same aging conditions, we have limited our testing to single grain solder joints. Even with this restriction, it is important to understand the precise grain orientation and the crystallographic direction normal to the polished surface in each tested joint so that results from multiple joints can be compared. Polarized light microscopy and Electron Back Scattered Diffraction (EBSD) techniques have been utilized for this purpose.

Experimental Test Matrix

The aging induced changes in mechanical behavior of single crystal non-doped and doped solder joints have been examined by nanomechanical testing of 10 different SAC

solder joints. Aging effects were evaluated using nanoindentation testing of four SAC105 joints, three SAC205 joints, two SAC305 joints, three SAC405 joint, three SAC0307 joints, four SAC105+Ni joints, four SAC105+Mn joints, three SAC205+Ni joints, three SACX0307 joints and three SN100 joints. Total 32 joints are tested at different aging conditions and listed in Table 2 .For each joint alloy, different sets of aging conditions were explored including: no aging; and 10, 30, 90, 180 and 360 days of aging at T = 125 C. For each aging duration, six indentations (2 x 3 array) were performed on each ball. All of the BGA test boards were stored in a freezer at T = -10 C prior to cross-sectioning to minimize any aging effects after board assembly. Aging of the epoxy mounted samples was then performed in a box oven, and light polishing was performed to remove any oxides after each oven exposure. For each aging condition and solder joint, the individual and average results for the 6 indentations have been reported for the elastic modulus, hardness, and creep strain rate vs. stress curves.

Table 3.2 Tested BGA Solder Joints

Alloy	No of Joints
SAC105	4
SAC205	3
SAC305	2
SAC405	3
SAC0307	3
SAC105+Ni	4
SAC105+Mn	4
SAC205+Ni	3
SACX0307	3
SN100C	3

3.6 Uniaxial Bulk Sample Preparation Procedure

A novel specimen preparation procedure was developed where solder uniaxial test specimens were formed in high precision rectangular cross-section glass tubes using a vacuum suction process. The setup for the procedure is shown in Figure 3.9. The solder alloy is melted in a crucible with a pair of heating coils, and thermal couples are attached to the crucible to control the temperature. One end of a rectangular cross-section glass tube is inserted into the molten solder, and the other end provides a suction force by using a vacuum pump. A regulator on the vacuum system controls the force drawing the solder into the tube. Then, the glass tubes are cooled by water quenching or sent through a SMT reflow oven (Figure 3.10) to re-melt the solder in the tubes and subject them to any desired temperature profile (i.e. same as actual solder joints), as illustrated in Figure 3.11. Finally the glass tube is removed (Figure 3.12), and the bulk specimen is inspected by a micro-focus X-ray system to detect its quality. Figure 3.13 shows an example of good and bad specimens. With proper experimental techniques, samples with no flaws and voids were generated.

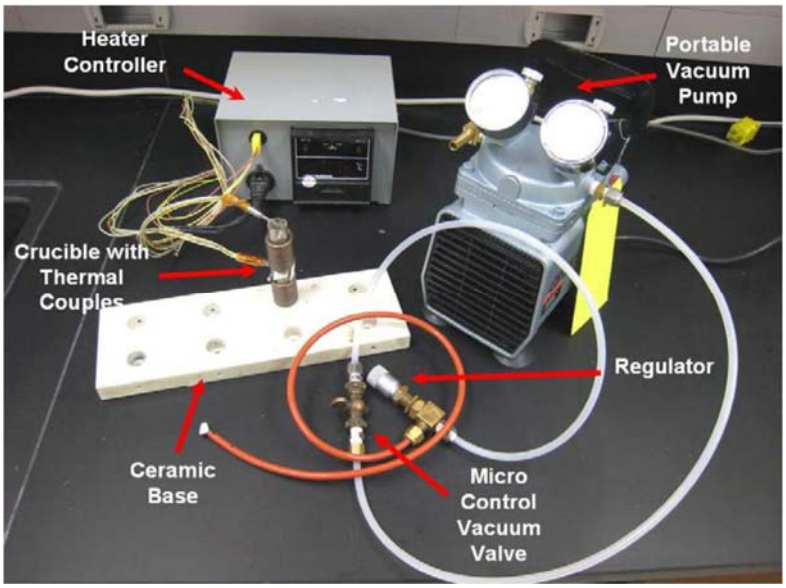

Figure 3.9 Specimen Preparation Setup

Figure 3.10 Heller 1800EXL Reflow Oven

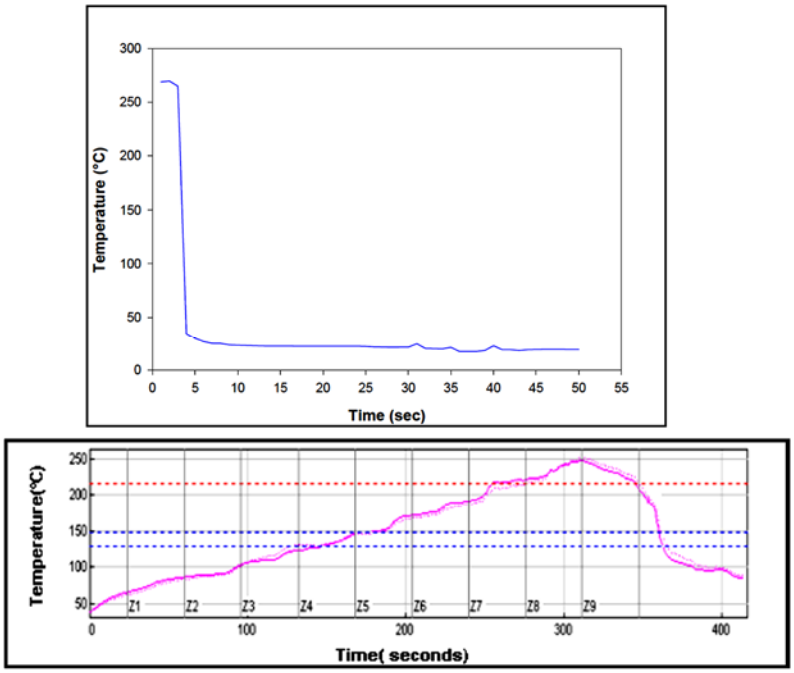

Figure 3.11 Specimen Cooling and Reflow Profiles

Figure 3.12 Solder Uniaxial Test Specimens

Figure 3.13 X-ray Inspection of Solder Specimens (Good and Bad Samples)

Uniaxial samples were formed with nominal dimensions of 80 x 3 x 0.5 mm. A thickness of 0.5 mm was chosen because it matches the height of typical BGA solder balls. Uniaxial creep testing has been performed on very small bulk specimens (SAC105 and SAC305) to correlate with the nanoindentation creep. In this study, we have used three different dimensions of uniaxial creep sample including 60 x 3 x 0.5 mm (large), 10 x 3 x 0.5 mm (medium) and 10 x 1 x 0.5 mm (small), as shown in Figure 3.14. These medium and small specimens cut out from the large ones using wire saw (diameter 0.01 in), as illustrated in Figure 3.15.

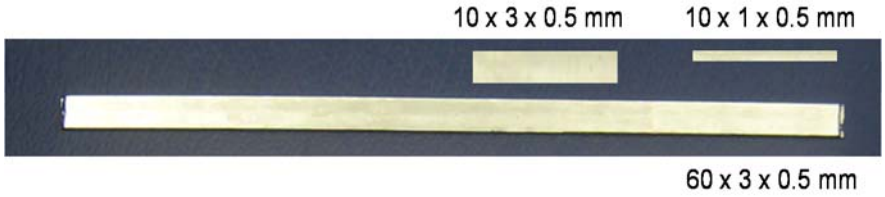

Figure 3.14 Uniaxial Specimens with Different Dimensions

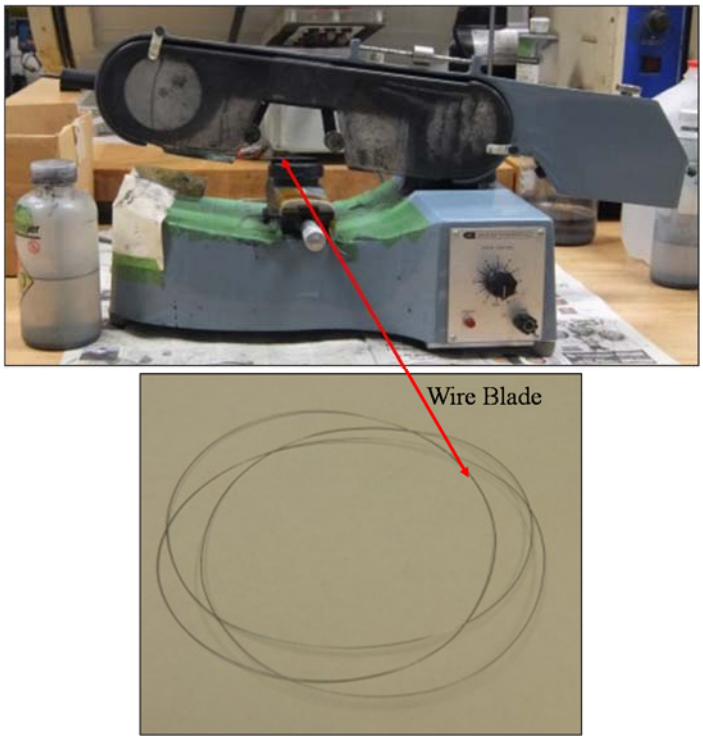

Figure 3.15 Wire Saw Set Up

Uniaxial Creep Testing System and Data Processing

Creep tests are carried out using a Micro Tension/Torsion testing machine as shown in Figure 3.16. The system provides an axial displacement resolution of 0.1 micron and a rotation resolution of 0.001°. Creep testing were conducted at room temperature (25 C). Samples were aged at 125 C for various durations (0, 10, 30, 90, 180, 270, and 360 days) while the applied stresses for the creep testing were σ = 5, 10, 15, 20 and 25 MPa.

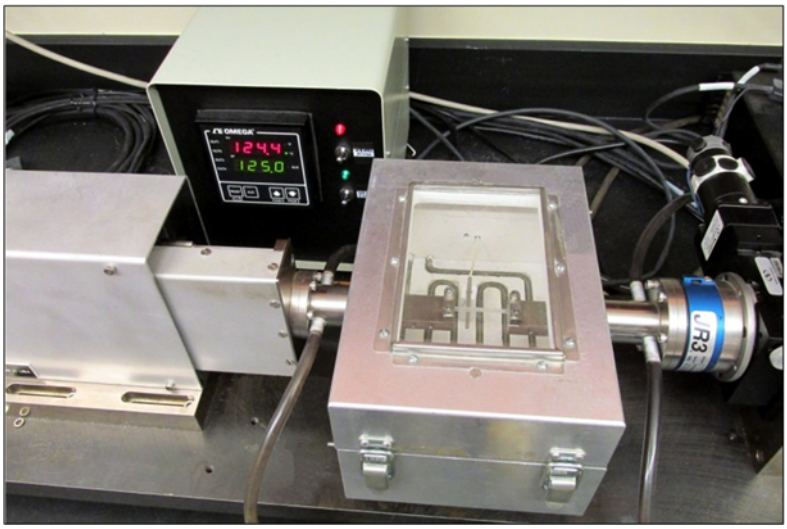

Figure 3.16 Uniaxial Testing System

In the creep testing, 6 to 8 specimens were tested for each set of aging conditions, and the creep strain versus time curves were recorded. These curves can be fitted with an empirical creep strain vs. time model to generate an "average" representation of the creep response under the specific aging conditions. For the range of aging conditions considered in this work, the raw creep strain vs. time data in the primary and secondary creep region were found to be well fitted by the four parameter Burger's (spring-dashpot) model (Figure 3.17):

$$\varepsilon(t) = 1 + C_0 + C_1 * t + C_2(1 - e - C_3 * t) \tag{3.8}$$

In practice, the measured creep rate for each curve was also compared to numerical evaluation of the minimum slope value in the secondary creep region for the observed strain rate versus time response. Variations of the average creep rates with aging were determined and then modeled as a function of aging time to correlate with the nanoindentation creep.

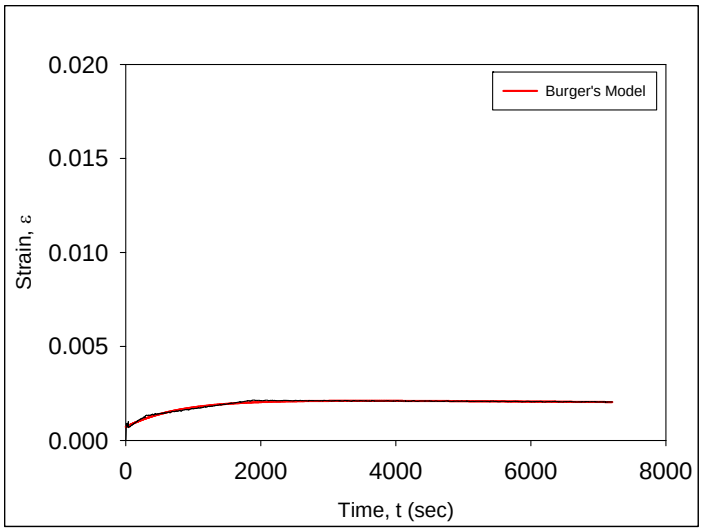

Figure 3.17 Solder Creep Curve and Burger's Model

3.7 Microstructure Study and Solder Joint Crystal Orientations

Microstructure analysis of the solder joints were conducted using an OLYMPUS BX60 Optical Microscope (Figure 3.18) equipped with Normaski prism for grain orientation/structure. Polarized light images were taken by adjusting the polarization filters to identify different grains in the samples. A JEOL JSM-7000F Field Emission Scanning Electron Microscope (SEM) (Figure 3.19) was also utilized for revealing morphology of solder joints. The grain orientation was characterized by an EBSD system (HKL, channel 5) attached to the JEOL JSM-7000F SEM instrument equipped with a field emission gun.

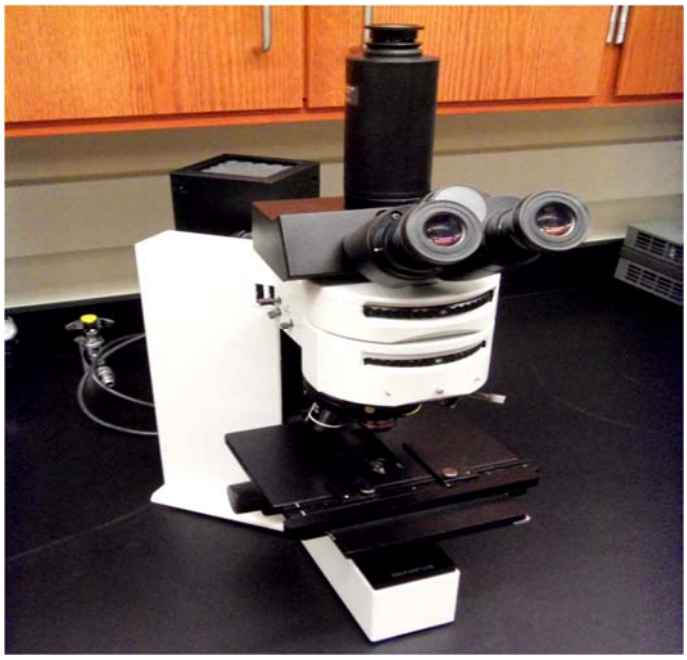

Figure 3.18 OLYMPUS BX60 Optical Microscope

Figure 3.19 JEOL JSM -7000F Field Emission SEM

Using polarized light optical microscopy on an Olympus BX60 metallographic microscope system, it was verified that each of the tested SAC solder joints were comprised

of a single grain. The unique colors and contrasts obtained for the samples for each alloy under polarized light also indicated that the crystal orientations were different (see Figure 3.20). To more rigorously understand the joint orientations, Electron Backscatter Diffraction (EBSD) was performed.

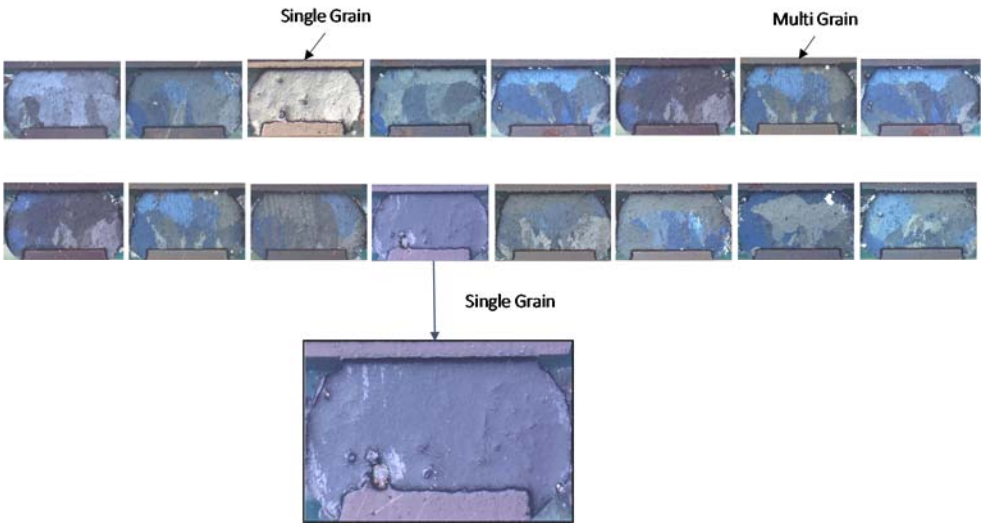

Figure 3.20 Solder Joints with Different Crystal Orientation

EBSD Set up and Procedure

Electron Backscatter Diffraction (EBSD) is a technique that is commonly used to characterize crystallographic or grain orientations on the surface of specimens [98]. As illustrated in Figure 3.21, the standard set-up for EBSD is relatively simple and a well-polished sample has to be highly tilted in the SEM. This is typically 70° from the horizontal. Electrons from the sample scatter and travel in all conceivable directions. They reach the detector and form the so-called Electron Backscatter Diffraction Pattern (EBSP). Higher tilt angles result in significantly poorer spatial resolution down the tilted surface, whereas lower tilt angles give weaker diffraction patterns and can result in increased charging in

insulating materials. A special EBSD detector is used to view the diffracted electrons. This detector is usually attached to one of the side ports of the SEM, and is comprised of a phosphor screen and a low light camera (CCD camera). During analysis, the detector is

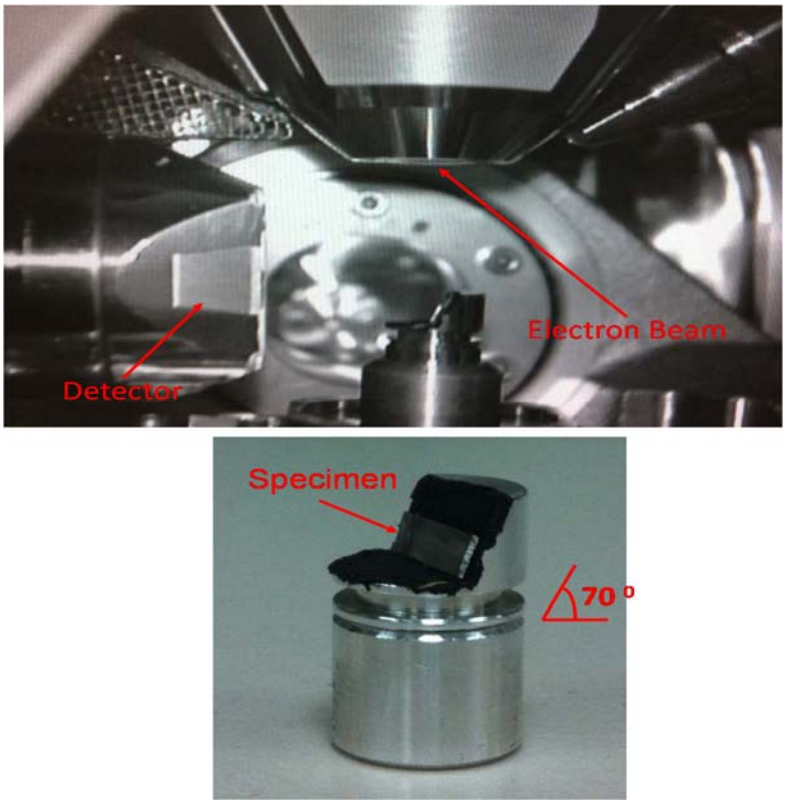

Figure 3.21 Setup for EBSD System

inserted into the chamber so that the phosphor screen is close to the sample, as shown in Figure 3.22. Electrons satisfy the Bragg diffraction condition:

$$n\lambda = 2d \sin \theta \tag{3.9}$$

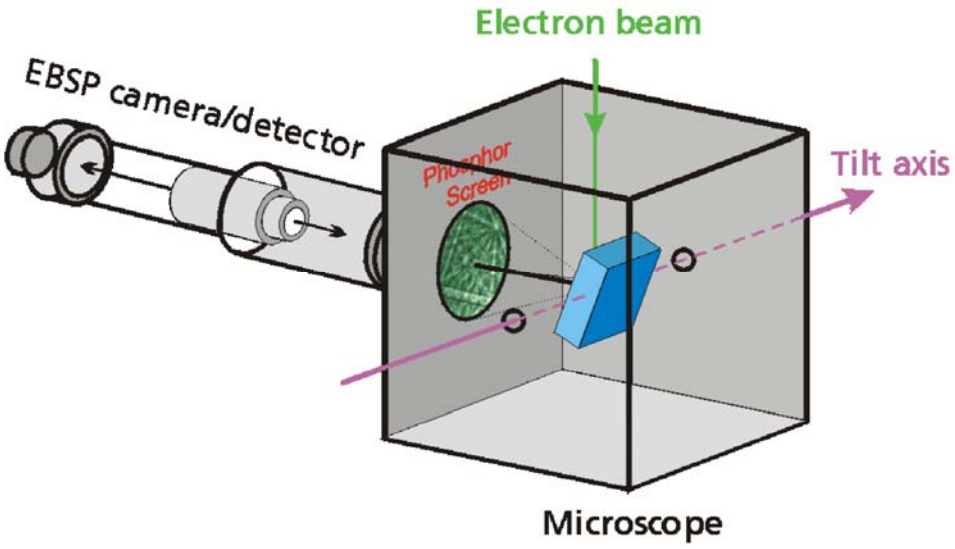

Figure 3.22 EBSD Detector with Phosphor Screen

where, λ is the wavelength of the incident beam, n is the order of the diffraction process, d is the interplanar spacing, and θ is the Bragg angle. For a particular crystallographic plane, these scattered electrons form two cones and intersect the screen of the detector, which generate straight lines of so-called Kikuchi bands. When sets of different lattice planes in the crystal structure are considered, the resulting diffraction pattern has many intersecting Kikuchi bands form on the phosphor screen. From an available phase database of EBSD results for β-Sn, the collected EBSP or Kikuchi bands can be indexed, as shown in Figure 3.23. After analyzing the EBSP, an area of the specimen surface is chosen to do automated mapping. Finally, collected EBSD data can be analyzed in the post processing to determine grain sizes and orientations using the software such as Tango and Mambo. Tango is used for a wide variety of maps to measure grains. Mambo is used to produce pole figures and inverse pole figures from EBSD orientation data. The primary steps of the EBSD method are given in Figure 3.24.

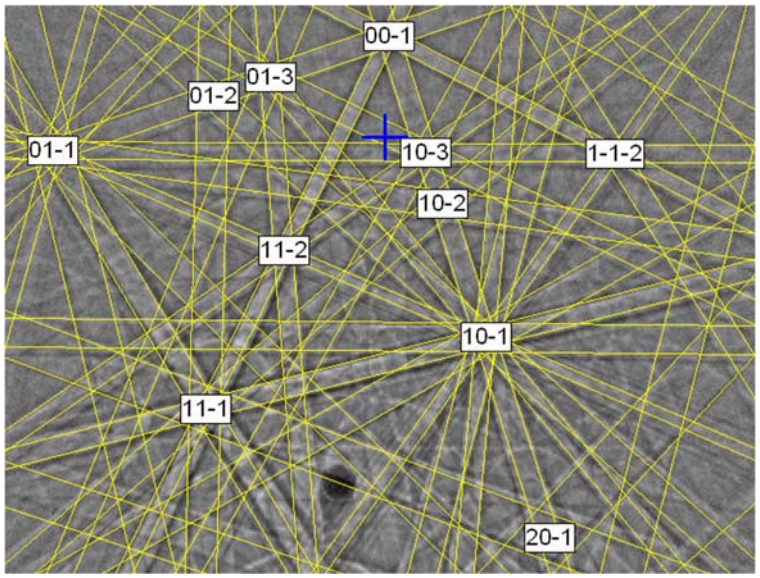

Figure 3.23 Detection of Kikuchi Band

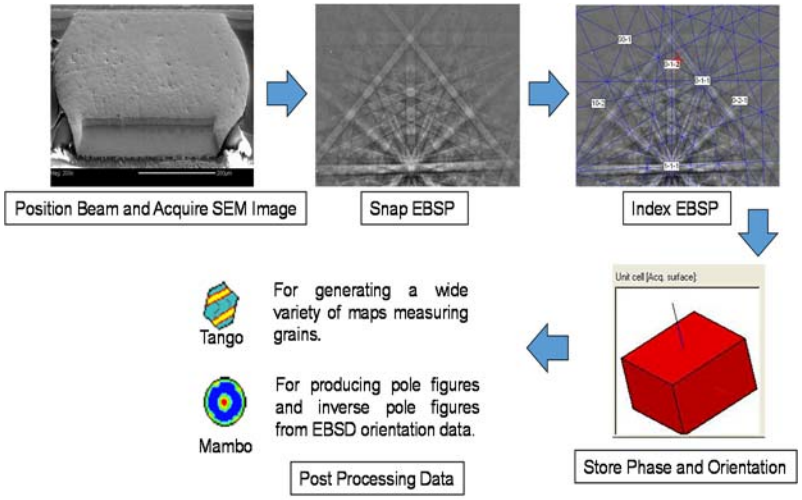

Figure 3.24 Primary Steps of the EBSD Method

EBSD Data Processing

A scanning map with a step size 5 μm in each direction was obtained for each joint using an EBSD system (Oxford HKL Channel 5) attached to a JEOL JSM-7000F SEM.

For each scanning point, the Electron Backscatter Diffraction Pattern (EBSP) or so-called Kikuchi bands were indexed, and an available phase database for β-Sn was used to find the three Euler angles relative to the crystallographic directions of the tetragonal crystal. These measurements determined the orientations of the crystallographic directions with respect to the three sample axes for the each grain. For the two SAC305 joints, the Euler angles and inverse pole figures (IPFs) about z-axes were generated from EBSD measurements, as shown in Table 3 and Figure 3.25. These measurements determined the orientations of the crystallographic directions with respect to the z- axes for the grain. The spot with the strongest intensity in each IPF is related to the orientation information for the β-Sn matrix.

Table 3.3 Crystal Orientation Euler Angles from EBSD

Joint	φ_1 [deg]	ϕ [deg]	φ_2 [deg]
#1	86.35	155.37	10.41
#2	124.28	16.18	11.16

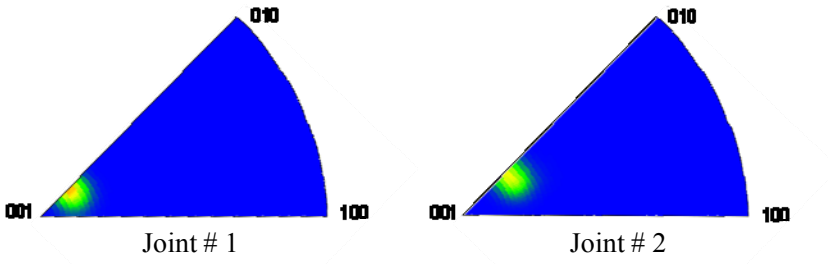

Figure 3.25 Inverse Pole Figures for SAC305 Solder Joints

From the EBSD data, three Euler angles were obtained for each grain, as shown in Table 2. Euler angles are widely used to define the orientation of a sample relative to the crystal, which are formed from rotating the sample coordinate system by φ_1 about the z'-axis, ϕ about the x-axis, and φ_2 about the z-axis until the sample coordinate system comes into coincidence with the crystallographic coordinate system, as shown in Figure 3.26. The

relationship between the sample coordinates and the crystallographic coordinates is established by the following vector transformation:

$$\begin{bmatrix} x \\ y \\ z \end{bmatrix} = \begin{bmatrix} \cos\varphi_2 & \sin\varphi_2 & 0 \\ -\sin\varphi_2 & \cos\varphi_2 & 0 \\ 0 & 0 & 1 \end{bmatrix} \begin{bmatrix} 1 & 0 & 0 \\ 0 & \cos\phi & \sin\phi \\ 0 & -\sin\phi & \cos\phi \end{bmatrix} \begin{bmatrix} \cos\varphi_1 & \sin\varphi_1 & 0 \\ -\sin\varphi_1 & \cos\varphi_1 & 0 \\ 0 & 0 & 1 \end{bmatrix} \begin{bmatrix} x' \\ y' \\ z' \end{bmatrix} \quad (3.10)$$

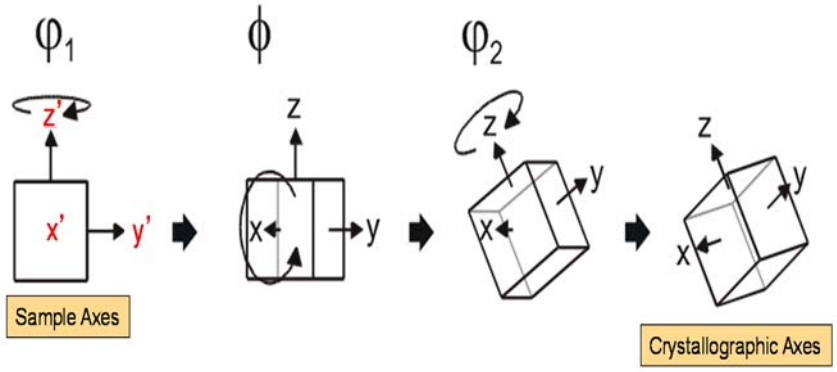

Figure 3.26 Formation of Euler Angles

The crystallographic orientation can be obtained based on the calculation of the vector transformation. For example, the crystallographic plane in the single grain (Joint # 1) perpendicular to the z' axis has a unit vector [0 0 1] in the sample coordinates. Using the equation of the vector transformation, the unit vector is transformed to be [0.0753 0.4089 0-.909] in the crystallographic coordinates. A particular plane can be expressed by the equation, Ax + By + Cz + D = 0, where A, B, C and D are constants. The vector [A B C] is a normal vector of the plane. For the transformed vector in the crystallographic coordinates [x y z] = [0.0753 0.4089 -0.909], the plane perpendicular to the unit vector can be written as 0.0753x + 0.4089y - 0.909z + D = 0. Then the intercepts of the x-axis, y-axis, and z-axis are equal to D/0.0753, D/0.4089, and D/-0.909, respectively. In the unit cell of β-Sn as shown in Figure 3.27, the plane (h k l) has three intercepts, given by a/h (x-

intercept), a/k (y-intercept) and c/l (z-intercept), where h, k, l are miller indices of the plane. Therefore, D/0.0753 = 5.8315/h and h = 0.439/D; D/0.4089 = 5.8315/k and k = 2.38/D; D/-0.909 = 3.1814/l and l = -2.89/D. By converting h, k, l to integers, the plane perpendicular to the transformed vector in the crystallographic coordinates was found to be (1 5 -6) for the single grain solder joint # 1. Using the same method as discussed, the crystallographic coordinates was found to be (1 5 10) for the solder joint # 2 with respect to the z' axis. The details of the orientation of the two solder joints were illustrated in table 3.4.

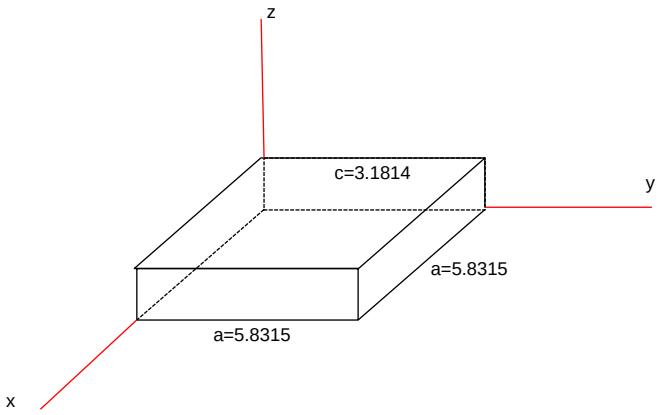

Figure 3.27 Unit Cell of β-tin

Table 3.4 Calculation of Grain Orientation for the Two SAC305 Solder Joints

Joints	Unit vector in sample coordinate	Unit vector in crystallographic coordinate	Miller indices			Plane
	z' axis	z' axis	h	k	l	
# 1	[0 0 1]	[0.0753 0.4089 -0.909]	0.439	2.38	-2.89	(1 5 -6)
# 2	[0 0 1]	[0.0541 0.2737 0.9730]	0.315	1.59	3.09	(1 5 10)

Using the elastic modulus map for a β-Sn crystal shown in Figure 1.12, the orientation of solder joint #2 is seen to be slightly closer to the highest stiffness (001) direction. Thus, it was expected to have slightly higher modulus and hardness values, and slower creep rates for all aging conditions, even before our testing revealed that this was actually the case.

Similar approach was used to identify the analogous inverse pole figure and crystallographic orientation for other tested solder joint alloys such as SAC105, SAC205, SAC405, SAC0307, SACX0307, SAC105+Ni, SAC105+Mn, SAC205+Ni and SN100C, respectively.

Analogous crystallographic coordinates and Inverse Pole Figure (IPF) plots for the tested SAC105, SAC205, SAC405, SAC0307, SACX0307, SAC105+Ni, SAC105+Mn, SAC205+Ni and SN100C solder joints are shown in Table 3.5, 3.6, 3.7, 3.8, 3.9, 3.10, 3.11, 3.12 and 3.13 and Figures 3.28, 3.29, 3.30, 3.31, 3.32, 3.33, 3.34, 3.35, and 3.36, respectively.

Table 3.5 Calculation of Grain Orientation for the Four SAC105 Solder Joints

Joints	Unit vector in sample coordinate	Unit vector in crystallographic coordinate	Miller indices			Plane
	z' axis	z' axis	h	k	l	
# 1	[0 0 1]	[0.6052 0.5057 0.614]	3.52	2.95	1.95	(2 1 1)
# 2	[0 0 1]	[0.6154 0.4207 -0.665]	3.58	2.45	-2.11	(1 1 -1)
# 3	[0 0 1]	[0.7389 0.4896 -0.461]	4.31	2.85	-1.46	(3 2 -1)
# 4	[0 0 1]	[0.5355 0.6644 0.518]	3.12	3.87	1.64	(2 2 1)

Table 3.6 Calculation of Grain Orientation for the Three SAC205 Solder Joints

Joints	Unit vector in sample coordinate	Unit vector in crystallographic coordinate	Miller indices			Plane
	z' axis	z' axis	h	k	l	
# 1	[0 0 1]	[0.456 0.8466 -0.270]	2.65	4.93	-0.85	(3 6 -1)
# 2	[0 0 1]	[0.681 0.4283 0.592]	3.97	2.49	1.88	(2 1 1)
# 3	[0 0 1]	[0.5427 0.8111 0.214]	3.16	4.72	0.68	(5 7 1)

Table 3.7 Calculation of Grain Orientation for the Three SAC405 Solder Joints

Joints	Unit vector in sample coordinate	Unit vector in crystallographic coordinate	Miller indices			Plane
	z' axis	z' axis	h	k	l	
# 1	[0 0 1]	[0.264 0.871 -0.410]	1.54	5.08	-1.30	(1 4 -1)
# 2	[0 0 1]	[0.869 0.0822 -0.486]	5.07	0.479	-1.54	(3 0 -1)
# 3	[0 0 1]	[0.666 0.2481 0.703]	3.88	1.37	2.24	(3 1 2)

Table 3.8 Calculation of Grain Orientation for the Three SAC0307 Solder Joints

Joints	Unit vector in sample coordinate	Unit vector in crystallographic coordinate	Miller indices			Plane
	z' axis	z' axis	h	k	l	
# 1	[0 0 1]	[0.881 0.1724 -0.444]	5.14	1	-1.39	(4 1 -1)
# 2	[0 0 1]	[0.745 0.5069 -0.43]	4.34	2.95	-1.36	(3 2 -1)
# 3	[0 0 1]	[0.827 0.4264 -0.359]	4.83	2.48	1.14	(4 2 1)

Table 3.9 Calculation of Grain Orientation for the Three SACX0307 Solder Joints

Joints	Unit vector in sample coordinate	Unit vector in crystallographic coordinate	Miller indices			Plane
	z' axis	z' axis	h	k	l	
# 1	[0 0 1]	[0.492 0.6633 0.562]	2.87	3.86	1.78	(1 2 1)
# 2	[0 0 1]	[0.874 0.061 0.478]	5.09	0.352	1.52	(3 0 1)
# 3	[0 0 1]	[0.0255 0.879 -0.475]	0.145	5.12	-1.51	(0 3 -1)

Table 3.10 Calculation of Grain Orientation for the Four SAC105+Ni Solder Joints

Joints	Unit vector in sample coordinate	Unit vector in crystallographic coordinate	Miller indices			Plane
	z' axis	z' axis	h	k	l	
# 1	[0 0 1]	[0.4685 0.6408 -0.6080]	2.73	3.74	1.93	(1 2 -1)
# 2	[0 0 1]	[0.5357 0.7061 -0.4630]	3.12	4.11	-1.47	(2 3 -1)
# 3	[0 0 1]	[0.6754 0.7178 0.1660]	3.93	4.18	0.528	(7 8 1)
# 4	[0 0 1]	[0.4550 0.8306 0.3240]	2.65	4.84	1.03	(3 5 1)

Table 3.11 Calculation of Grain Orientation for the Four SAC105+Mn Solder Joints

Joints	Unit vector in sample coordinate	Unit vector in crystallographic coordinate	Miller indices			Plane
	z' axis	z' axis	h	k	l	
# 1	[0 0 1]	[0.9742 0.1772 -0.1280]	5.68	1.03	-0.407	(5 1 0)
# 2	[0 0 1]	[0.5789 0.5981 0.552]	3.37	3.48	1.75	(2 2 1)
# 3	[0 0 1]	[0.0769 0.7502 -0.6560]	0.448	4.37	-2.08	(0 2 -1)
# 4	[0 0 1]	[0.3746 0.9261 0.019]	2.18	5.40	0.60	(3 9 1)

Table 3.12 Calculation of Grain Orientation for the Three SAC205+Ni Solder Joints

Joints	Unit vector in sample coordinate	Unit vector in crystallographic coordinate	Miller indices			Plane
	z' axis	z' axis	h	k	l	
# 1	[0 0 1]	[0.2655 0.8595 0.435]	1.54	5.01	1.38	(1 4 1)
# 2	[0 0 1]	[0.5574 0.5519 -0.222]	3.25	3.21	-1.97	(2 2 -1)
# 3	[0 0 1]	[0.5655 0.79361 -0.222]	3.29	4.62	-0.71	(5 7 -1)

Table 3.13 Calculation of Grain Orientation for the Three SN100C Solder Joints

Joints	Unit vector in sample coordinate	Unit vector in crystallographic coordinate	Miller indices			Plane
	z' axis	z' axis	h	k	l	
# 1	[0 0 1]	[0.9692 0.1152 - 0.215]	5.65	0.672	-0.684	(8 1 -1)
# 2	[0 0 1]	[0.7539 0.5014 -0.4240]	4.39	2.92	-1.34	(3 2 -1)
# 3	[0 0 1]	[0.2166 0.8681 0.4450]	1.26	5.06	1.41	(1 4 1)

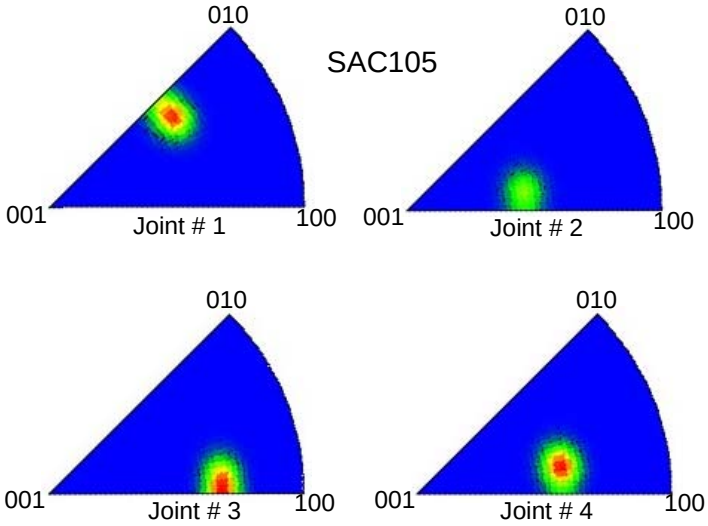

Figure 3:28 Inverse Pole Figures for SAC105 Solder Joints

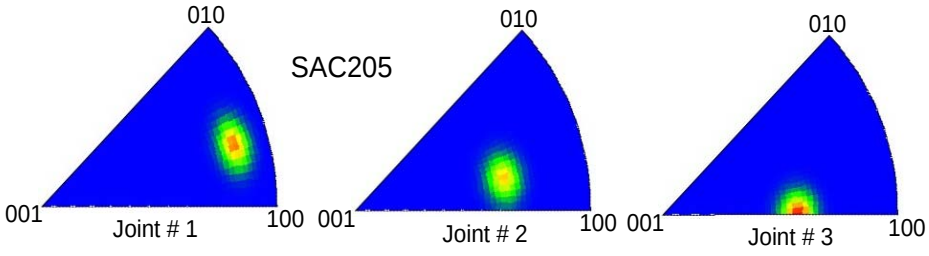

Figure 3:29 Inverse Pole Figures for SAC205 Solder Joints

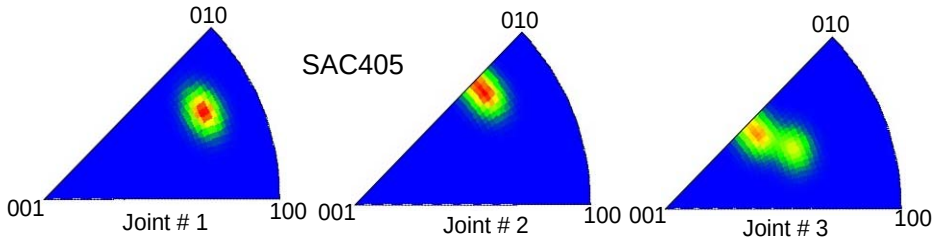

Figure 3:30 Inverse Pole Figures for SAC405 Solder Joints

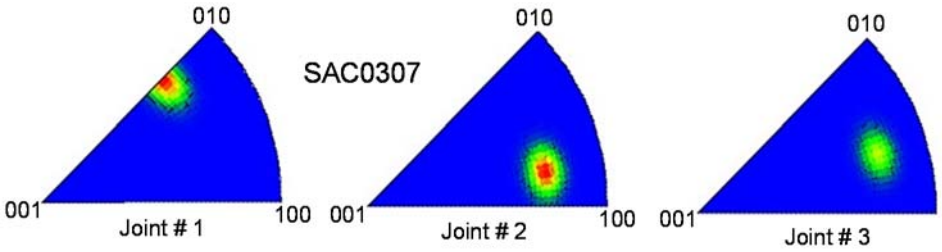

Figure 3:31 Inverse Pole Figures for SAC0307 Solder Joints

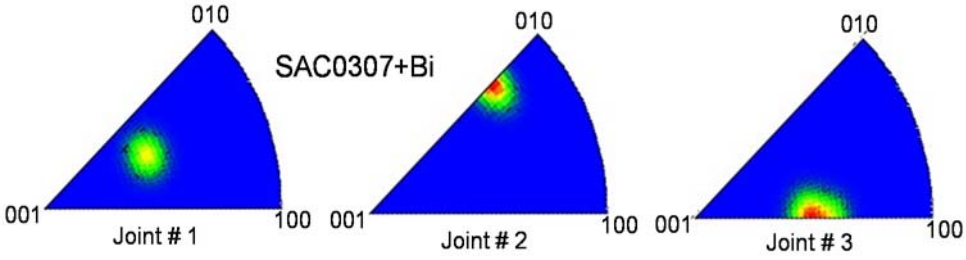

Figure 3:32 Inverse Pole Figures for SAC0307+Bi Solder Joints

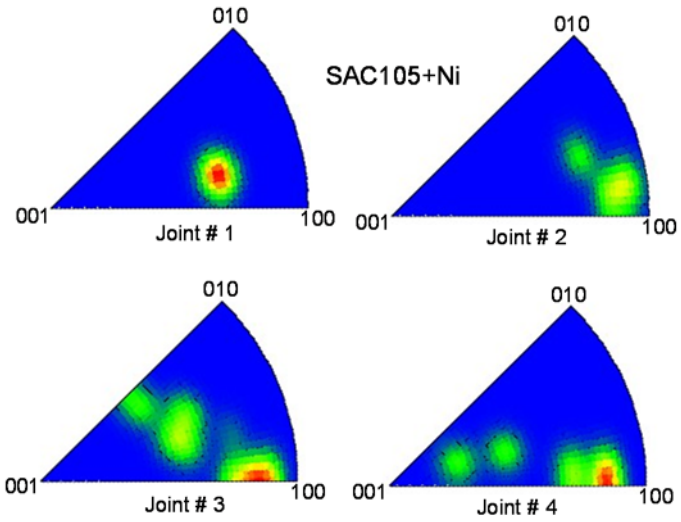

Figure 3:33 Inverse Pole Figures for SAC105+Ni Solder Joints

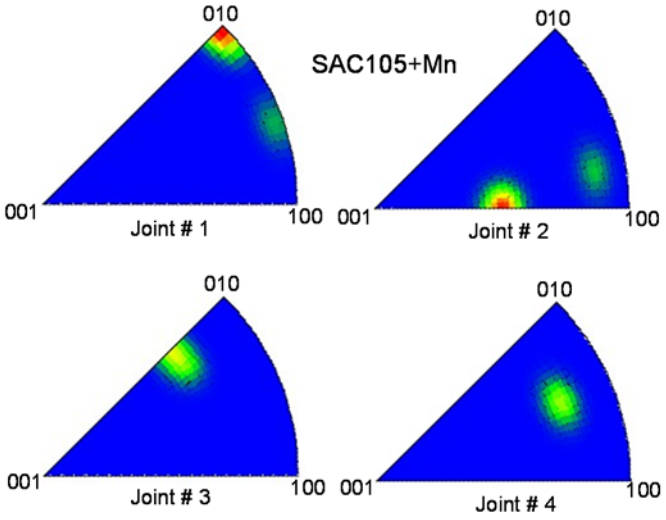

Figure 3:34 Inverse Pole Figures for SAC105+Mn Solder Joints

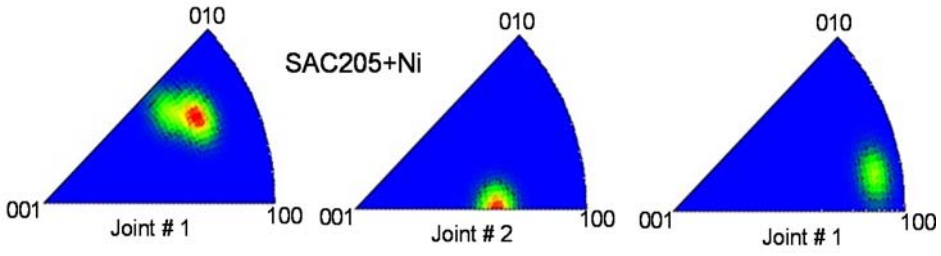

Figure 3:35 Inverse Pole Figures for SAC205+Ni Solder Joints

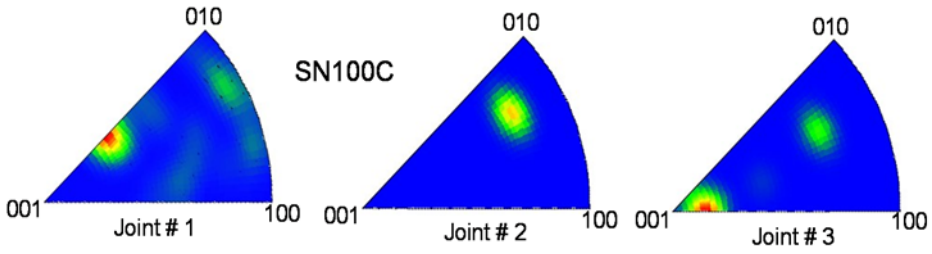

Figure 3:36 Inverse Pole Figures for SN100C Solder Joints

For each alloy, the joint orientations were unique for each joint in the set. For example, it is expected that joint #1 will have the largest modulus and hardness for the SAC105 joints. Likewise, joint #1 is expected to have the largest modulus and hardness for the SAC205 joints, and joint #2 is expected to have the largest modulus and hardness for the SAC405 joints. Joint # will have the largest modulus and hardness for the SAC0307 joints where joint #1 have the largest modulus and hardness for the SACX0307 joints. In case of SAC105+Ni joints, joint #4 will have the largest modulus and hardness whereas joint #1 is expected to have the largest modulus and hardness for the SAC105+Mn joints. For the both SAC205+Ni and SN10C alloy, joints #1 is expected to have the largest modulus and hardness.

3.8 X-ray Microdiffraction Study

The development of the modern integrated circuit and related device structures has brought about the need to understand material behavior, including mechanical properties, at the submicron and nanometer scale. The creation of such small components such transistors and solder interconnects requires a thorough understanding of the mechanical properties of materials at these small length scales. Synchrotron based x-ray microdiffraction is a new powerful experimental technique available for studying mechanical properties of materials at micron or submicron scales, in the range of grains and defect interactions [99-100]. The method is capable of measuring the variation in internal (residual) stress, strain, grain orientation, grain rotation, and plastic deformations between grains and within individual grains [101-104]. This can provide important information on changes occurring within a solder joint at small scales. The technique is based on very small submicron high brilliance x-ray beam, which is produced using focusing optics such as Kirkpatrick-Baez (KB) mirrors at synchrotron facilities. Data are recorded as raster scans of an array of Laue diffraction patterns by a large area charge couple device x-ray detector, and then subsequently analyzed to give grain orientation, stress/strain distributions, and dislocation densities.

The Advanced Light Source (ALS) at Lawrence Berkeley National Laboratory in Berkeley, CA, is a third-generation synchrotron radiation source which is well known as one of the brightest available sources of extreme ultraviolet and soft x-ray radiation in the world. The x-ray microdiffraction beamline described here is located at superconducting bending magnet beamline 12.3.2 of the ALS. The beamline provides an extremely bright x-ray beam with a spectral range of approximately 5 - 22 keV.

Figure 3.37 shows the schematic layout of the X-ray microdiffraction beamline. It consists of the source, a horizontally deflecting toroidal M1-mirror (grazing angle 3.5 mrad), a pair of roll slits defining the size of the virtual secondary source, a four-bounce two-channel cut Si (111) monochromator, a second pair of slits (from JJx- ray, Denmark) serving as aperture, a set of KB mirrors, the sample stage, and two detectors. The acceptance of the M1- mirror is limited to 0.2 mrad by a water-cooled aperture. The distances from the source for this beamline are 13, 22.4, and 24.8 m for M1, secondary source slits, and sample, respectively. The silicon M1 mirror focuses the source onto a virtual object. This intermediate image is de-magnified by a ratio of 8:1 and 16:1 in horizontal and vertical, respectively, by a pair of KB mirrors. A four-bounce Si (111) monochromator can optionally be brought into the beam path for monochromatic microdiffraction on nanosized grains. The sample is positioned on a high-precision stage consisting of eight different motorized stages as indicated in Figure 3.38 a. The lower xyz stage allows for aligning the rotation axes (χ and ϕ) onto the x-ray focal point (Figure 3.38 b). The upper xyz stages allow to place the sample onto the center of rotation and to scan the sample through the x-ray beam. Since the beamline is designed for high spatial resolution with an x-ray focus spot below 1 μm, the scanning stages need to be more precise than this. The sample is accurately positioned on the calibrated x-ray focus point by means of a commercial laser triangulation unit (Keyence LK-G152). The absolute distance between sample and diffraction detector is additionally calibrated using a Si-diffraction standard single crystal. The beamline is equipped with two detectors, namely, a MAR133 x-ray CCD and a Si-drift detector. The MAR133 is used to record the polychromatic and monochromatic diffraction patterns.

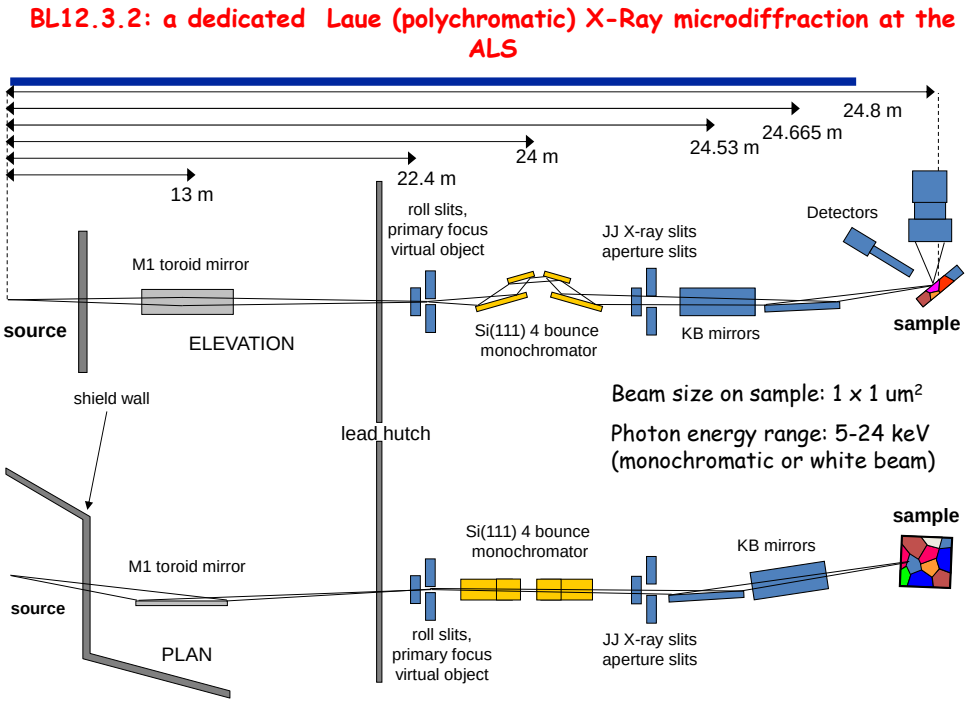

Figure 3:37 X-ray Microdiffraction Setup

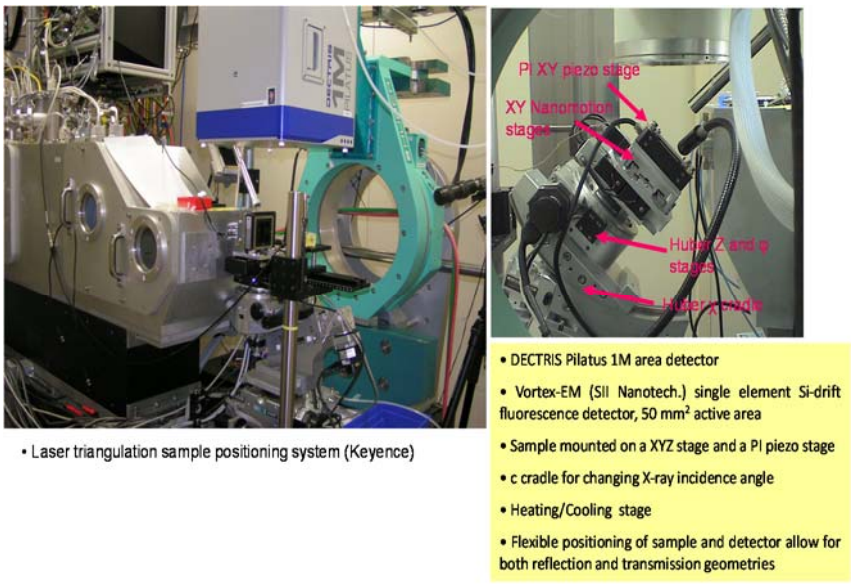

(a) Sample Positioning Stage

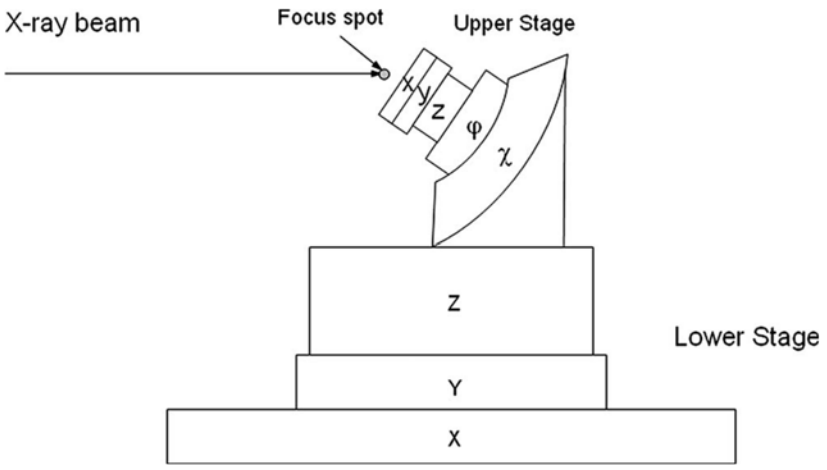

(b) Lower Stage for Sample Alignment

Figure 3:38 Sample Stage with Detector

The CCD detector is mounted on a Huber stage with its rotation axis mounted horizontally. This allows placing the detector at various vertical two theta angles between 0° and 90°. The Si-drift detector (Vortex-EM by SII Nanotechnology Inc.) is used for x-ray fluorescence elemental mapping, which in turn can also be used to precisely locate the focused x-ray on the sample.

3.9 Summary and Discussion

Aging phenomena in actual solder joints have been explored by nano-mechanical testing of single SAC lead free solder joints extracted from PBGA assemblies. Nanoindentation testing procedure and sample preparation has been presented to explore the stress-strain and creep behavior of the SAC solder materials at the joint scale. Polarized light microscopy and Electron Back Scattered Diffraction (EBSD) techniques have been utilized to identify the grain structure and crystal orientations in the tested joints. In addition, an approach has been developed to predict tensile creep strain rates for low stress

levels using nanoindentation creep data measured at very high compressive stress levels. With these approaches, aging effects in solder joints were quantified and correlated to the magnitudes of those observed in testing of miniature bulk specimens.

A novel sample preparation procedure was discussed for uniaxial test specimens. Uniaxial creep testing has been done on miniature bulk specimen using multifunctional microtester. Microstructural analysis was conducted using Scanning Electron Microscope (SEM) and Optical Polarize Microscope. X-ray microdiffraction technique was employed to characterize solder joints after various aging exposures.

CHAPTER 4

CHARACTERIZATION OF SAC305 SOLDER JOINTS AND PREDICTION OF UNIAXIAL CREEP USING NANOINDENTATION CREEP

4.1 Introduction

Solder joint fatigue is one of the predominant failure mechanisms in lead free electronic assemblies exposed to thermal cycling. Thus, accurate mechanical properties and constitutive equations for solder materials are needed for use in mechanical design, reliability assessment, and process optimization. However, there has been little work on mechanical properties and creep behavior in individual solder joints. Such knowledge is crucial for the optimizing the design, manufacturing, and reliability of microelectronic packages. Characterization of individual joints is quite challenging because of their extremely small size, the difficulty in gripping them and applying controlled loadings.

In this chapter, the mechanical properties and creep behavior of lead free solders are being characterized by nano-mechanical testing of single grain SAC305 solder joints extracted from PBGA assemblies. Using nanoindentation techniques, the stress-strain and creep behavior of the SAC305 solder have been explored at the joint scale. Mechanical properties characterized included the elastic modulus, hardness, and yield stress. An approach has been developed to predict tensile creep strain rates for low stress levels using nanoindentation creep data measured at very high compressive stress levels. Additional testing has been performed on very small tensile specimens and creep rate found in these specimens were on the same order of magnitude as those observed in the single grain joints.

In addition, the test results show that the modulus, hardness and creep properties of the solder joints are highly dependent on the crystal orientation.

4.2 Measurement of Elastic Modulus and Hardness

In this chapter, the results for SAC305 (96.5Sn-3.0Ag-0.5Cu) solder joints have been presented. These joints were extracted from test boards where the original components had SAC305 solder balls, the bare test boards had ENIG surface finish, and where SAC305 solder paste was used in the surface mount assembly process. The assembled PBGA components were cut out from the test boards and then cross-sectioned into samples of two joints each. Details of the sample preparation and nanoindentation procedure were described in chapter 3. The crystallographic orientation of the two solder joints were found to be (1 5 -6) and (1 5 10) plane, respectively (Figure 3.25).

Typical CSM results for the hardness and elastic modulus as a function of indentation depth for a single indent in a SAC305 solder joint are shown in Fig 4.1 (a) and (b), respectively. The results were found to stabilize and be independent of depth after approximately 1500 nm of indentation depth. So, average value were taken where they are independent of indentation depth. By taking that, surface roughness effect was eliminated.

Thus, the E and H values were determined by finding the average the values of the CSM response curves for h > 1500 nm. The results were found to stabilize and be independent of indentation depth. For the indentation test data in Figures 4.1, the extracted values were E = 50.25 GPa and H = 0.310 GPa for this solder joint on the (1 5 -6) plane. Thus, the compressive yield stress can be estimated by $\sigma_Y = H/3 = 103.33$ MPa. This is good agreement with the theoretical calculation of modulus map of β-tin crystal [Figure

1.12]. Table 4.1 summarized the derived modulus and hardness value of SAC305 solder joints at different crystallographic orientation.

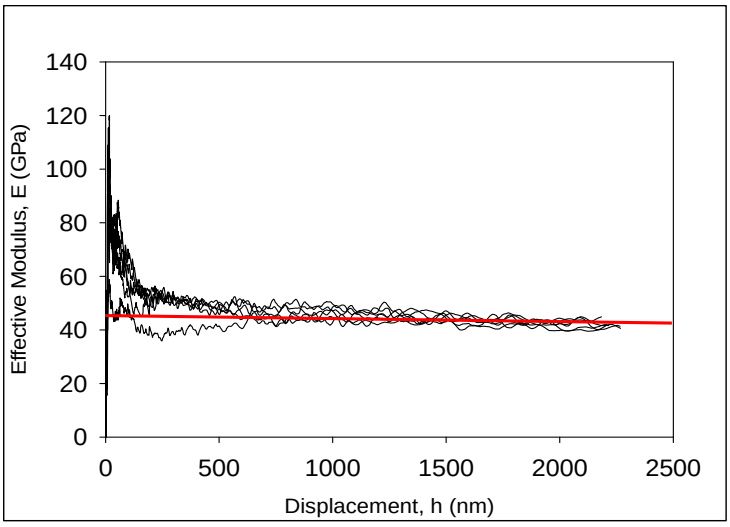

(a) Average of 6 Indents- Modulus

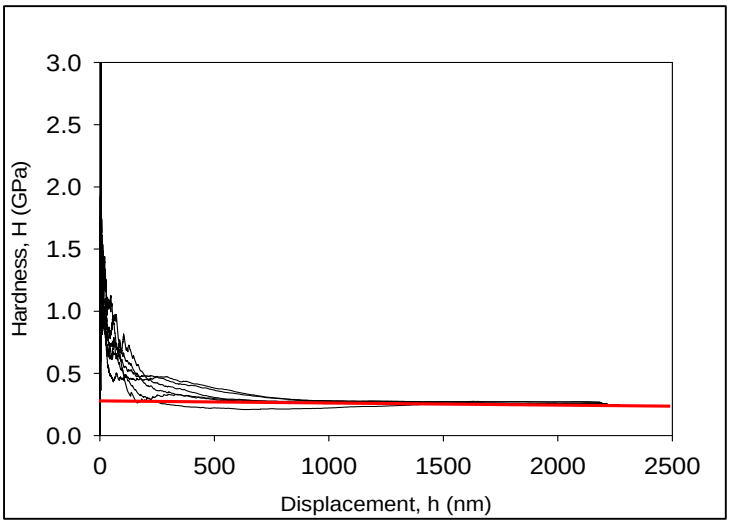

(b) Average of 6 Indents- Hardness

Figure 4.1 Nanoindentation Effective Modulus and Hardness of SAC305 Solder as a Function of Indentation Depth

Table 4.1 SAC305 Solder Ball Mechanical Properties

Property	Joint # 1	Joint # 2
Modulus (GPa)	50.25 ± 0.54	55.59 ± 1.98
Hardness (GPa)	0.310 ± 0.021	0.34 ± 0.008
Crystallographic Orientation	(1 5 -6)	(1 5 10)

As expected from the crystal orientation presented above, the mechanical properties of joint # 2 were much higher than joint # 1. So, there is a strong anisotropy in modulus and hardness found in solder joints. The crystal anisotropy of solder joint has a dominant effect on stress and strain thus damage nucleation in microelectronic packaging as there is a relationship between crystal orientation and damage nucleation [29]. This might provide a basis for identifying the reliability criteria arising from crystal anisotropy in solder joints.

4.3 Measurement of Creep Behavior

Nanoindentation creep testing was performed during the hold/dwell at the peak load of 30 mN and dwell times of 900 sec. The total displacements were measured continuously, and the creep displacement data (change in displacement) during the constant load period were extracted. For example, Figure 4.2 illustrates the measured creep displacement vs. time response for an array of 6 indents performed a single solder joint under similar conditions. The creep displacement data can be fit well with a variety of empirical models.

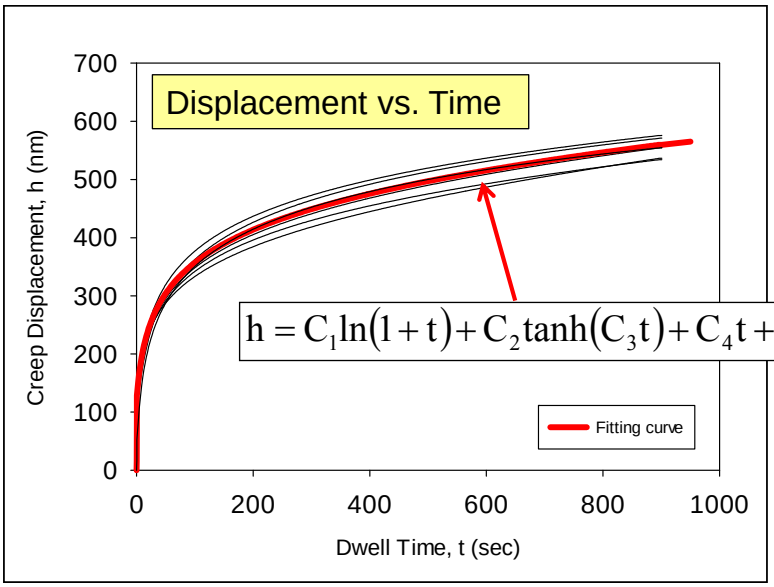

Figure 4.2 Creep Displacement Data for SAC305 Solder

In this work, log hyperbolic tangent model was used [105].

$$h(t) = C_1 \ln(1+t) + C_2 \tanh(C_3 t) + C_4 t + C_5 \tag{4.1}$$

where C_1, C_2, C_3, C_4 and C_5 are fitting constants. The red curve in Figure 4.2 is the fit of eq. (4.1) to the creep data from the 6 individual indent curves.

The creep rate (creep deformation rate) is determined by taking the derivative of the creep displacement vs. time response:

$$\dot{h} = \frac{dh}{dt} \tag{4.2}$$

Using the fitting curve in eq. (4.1), the creep rate can be easily evaluated as a function of time.

The concept of indentation creep strain rate was developed by Mayo and Nix [106-107], and is defined by dividing the creep deformation rate by the instantaneous creep deformation at each time:

$$\dot{\varepsilon} = \frac{1}{h}\frac{dh}{dt} \tag{4.3}$$

By again using the fitting curve in eq. (4.1), the creep rate can be easily evaluated as a function of time. For the creep deformation data in Figure 4.2, the creep strain rate vs. time response is plotted in Figure 4.3, and a nearly constant strain rate value of 4.3 x 10^{-5} sec^{-1} was obtained for a long creep time of 900 sec.

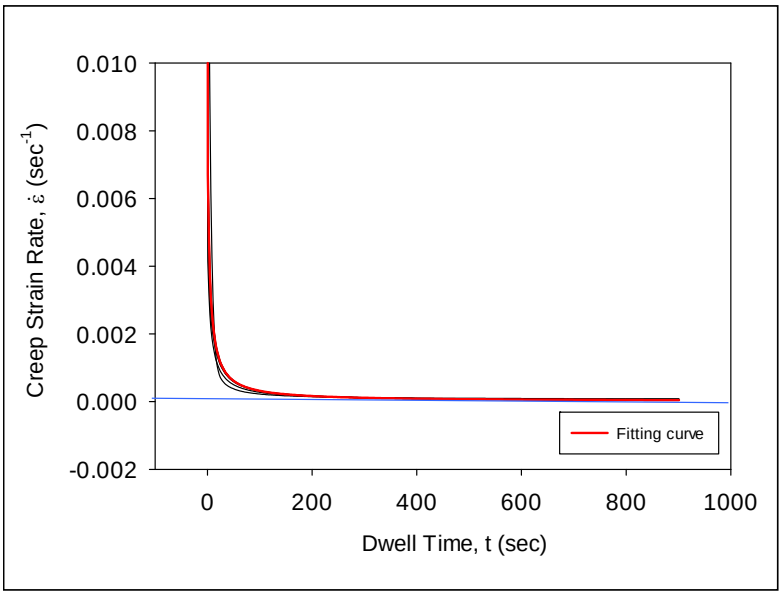

Figure 4.3 Creep Strain Rate vs. Time for SAC305 Solder

The nanoindentation creep response never actually achieves a constant strain rate due to the fact that the projected contact area, A of the indentation continues to grow during the creep deformation period (constant load region). For example, evolution of the hardness, H for the responses in Figure 4.2 were calculated using the applied constant load

of P_{max} = 30 mN, and the time evolving contact area calculated from the measured the creep deformations. Figure 4.4 illustrates the hardness vs. time response for the 6 individual indents. Using the Tabor relation , the applied compressive creep stress vs. time can be estimated using $\sigma = H/3$, and Figure 4.5 shows the stress vs. time response for the individual 6 individual indents and the fitting curve from Figure 4.2. It is seen from Figures 4.4-4.5 that the creep stress becomes fairly constant (σ = 54 MPa) after 900-1000 seconds of constant load application. Thus, the asymptotic strain rate extracted from Figure 4.3 can be estimated to be steady state strain rate for this stress level. In nanoindentation creep deformed volume under the indenter is continuously expanding so the contact area is changing. But any further increase in penetration has limited effect on contact area. So the creep stress is fairly constant at the larger depths. Thus, the asymptotic strain rate extracted also believes to be steady state strain rate for this stress level.

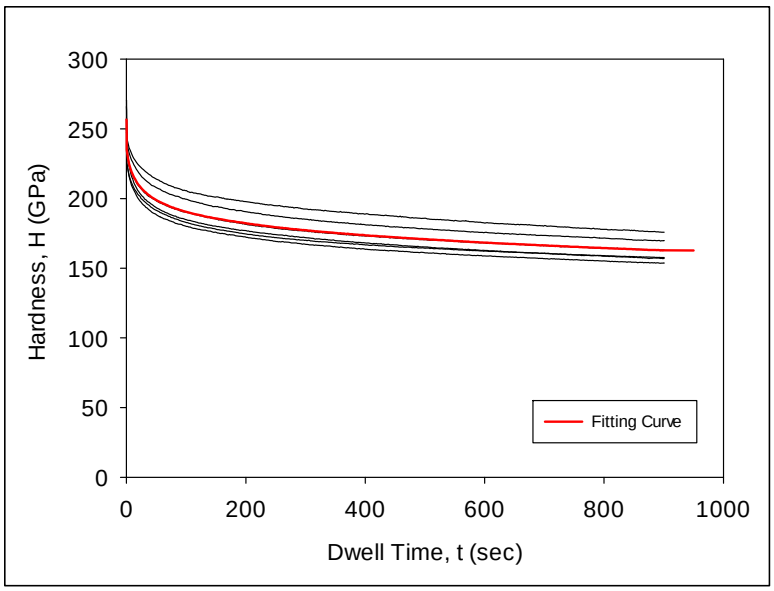

Figure 4.4 Hardness vs. Time for SAC305 Solder during the Nanoindentation Creep Loading

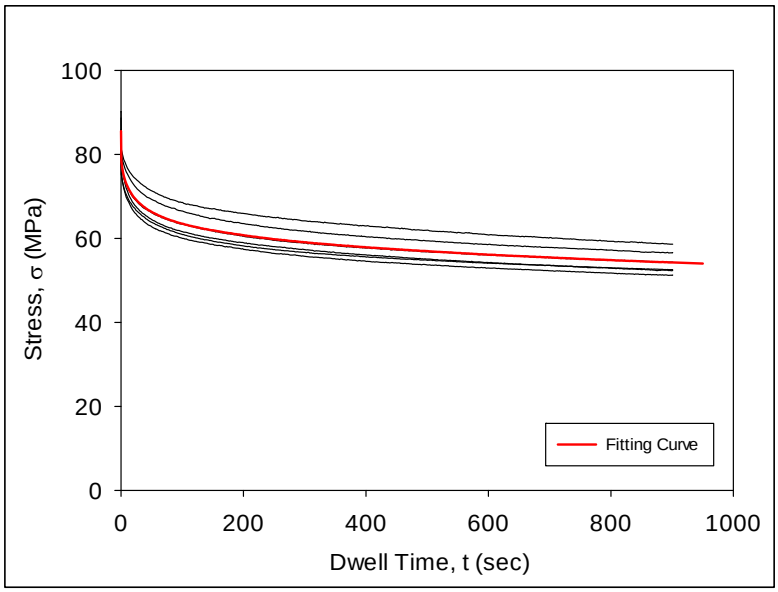

Figure 4.5 Stress vs. Time for SAC305 Solder during the Nanoindentation Creep Loading

The entire strain rate vs. applied stress response for the SAC solder can be estimated by extracting the creep rate from the fitting curve in Figure 4.3 and the applied stress from the fitting curve in Figure 4.5 for each time, and then replotting the results to eliminate time as shown in Figure 4.6. With this approach, a single nanoindentation experiment can be used to generate the complete creep strain rate vs. stress response of the material. The first point on the curve in Figure 4.6 has the coordinates $\dot{\varepsilon} = 4.3 \times 10^{-5}$ sec^{-1} and $\sigma = 54$ MPa, and are the values obtained for the long dwell time of 900 sec. Since the nanoindentation tests are compressive in nature, the applied stress levels in Figure 4.6 ($\sigma >$ 54 MPa) possible via nanoindentation are well above those that are normally possible and of interest for lead free solders in tension or shear.

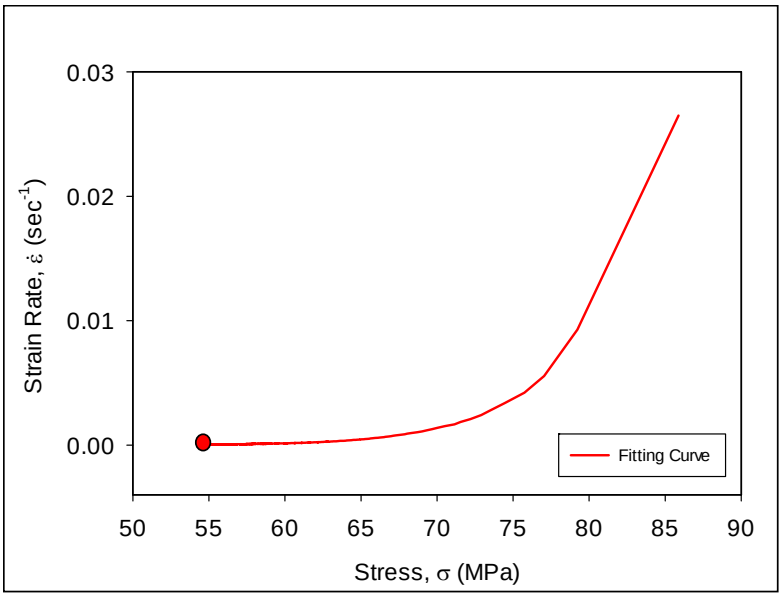

Figure 4.6 Creep Strain Rate vs. Stress for SAC305 Solder Extracted from the Nanoindentation Creep Data

For example, the tensile stress levels typically used in tensile creep testing are in the range of 10-30 MPa [38-43]. So, the concept of single strain rate may be valid at the larger depth where displacement rate is small compared to the beginning of the indentation where indentation stress and strain is very high. The low stress creep response can be extrapolated from the nanoindentation measured compressive creep response by nonlinear regression fitting of the data in Figure 4.6 using one of the popular creep models for lead free solders such as the exponential model :

$$\dot{\varepsilon} = C_1 e^{C_2 \sigma} \tag{4.4}$$

or the Garofalo model

$$\dot{\varepsilon} = C_1 [\sinh(C_2 \sigma)]^{C_3} e^{-\frac{C_4}{T}} \tag{4.5}$$

where the C_i (i = 1, 2, 3, 4) are fitting constants. These calculations have performed and the results are illustrated in the log-log plots in Figures 4.7-4.8. In each of these graphs,

the red curve is the measured nanoindentation creep response while the blue and green curves are the regression fitting results using the exponential and Garofalo models, respectively. Both creep models are able to fit the nanoindentation creep results equally well, and both give nearly the same results when extrapolated to lower stress levels.

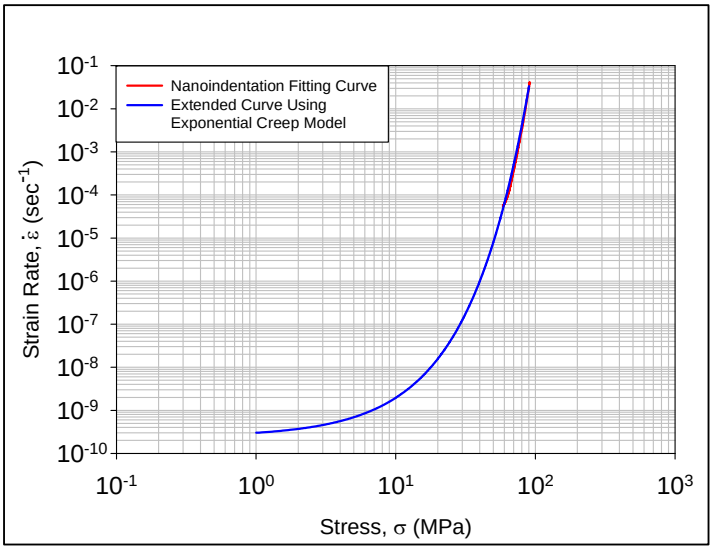

Figure 4.7 Creep Strain Rate vs. Stress for SAC305 Solder Using Exponential Creep Model

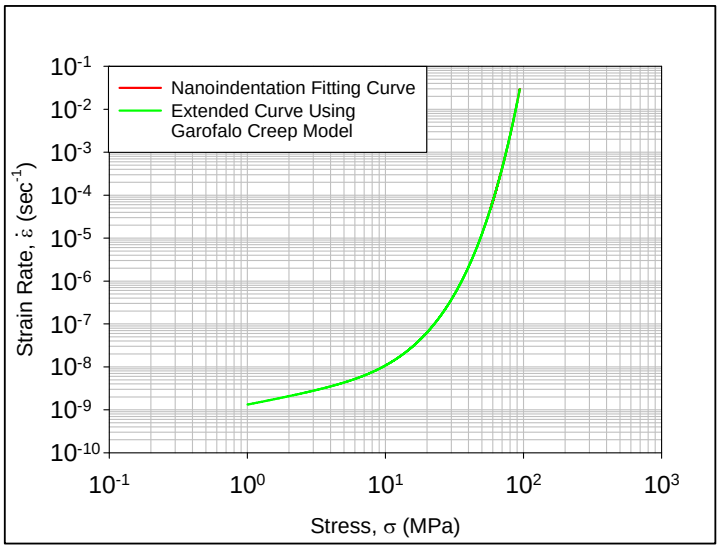

Figure 4.8 Creep Strain Rate vs. Stress for SAC305 Solder
Using Garofalo Creep Model

4.4 Comparison of Uniaxial Creep with Nanoindentation Creep

Uniaxial creep testing has been done by applied stress of σ = 5, 10, 15, 20 and 25 MPa respectively at room temperature. Sample preparation and testing procedure has been described in Chapter 3.

The raw strain vs. time data were fitted using Burgers's model [41].

$$\varepsilon(t) = C_0 + C_1 t + C_2\left(1 - e^{-C_3 t}\right) \tag{4.6}$$

Steady state creep strain rate was evaluated by calculating the minimum slope value in the secondary creep region of the strain rate versus time response. Figure 4.9 illustrates the uniaxial creep curves for the SAC305 bulk solder for the five different stress levels. Corresponding creep strain rate versus stress is fitted with the Garofalo model [23] and plotted in Figure 4.10.

$$\dot{\varepsilon} = C_1[\sinh(C_2\sigma)]^{C_3} * \exp\left(-\frac{C_4}{T}\right) \tag{4.7}$$

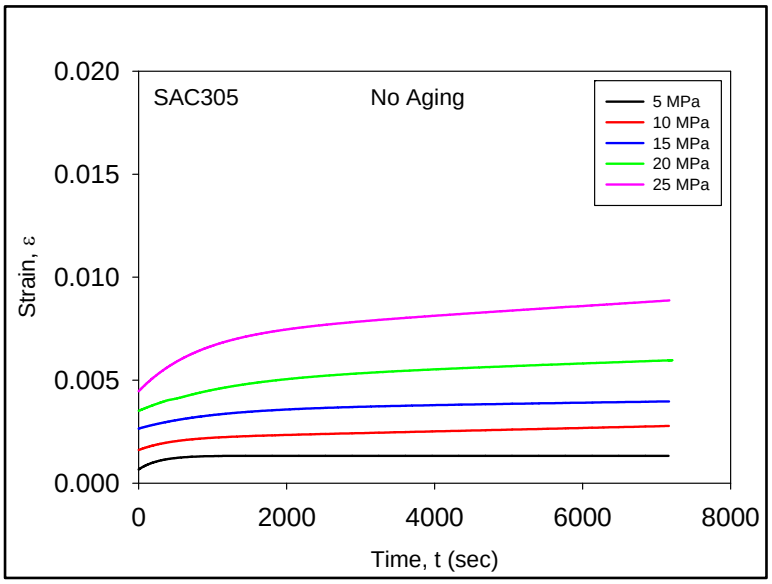

Figure 4.9 Creep Strain vs. Time for SAC305 Bulk Solder

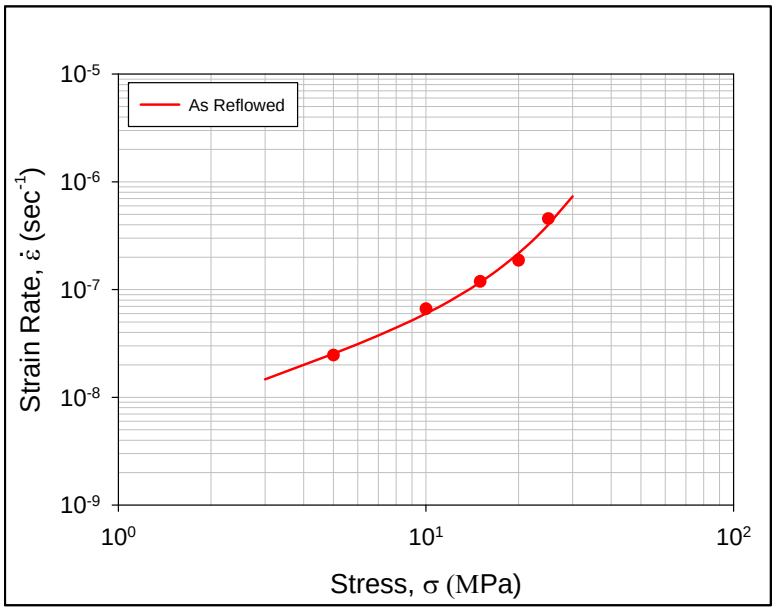

Figure 4.10 Creep Strain Rate vs. Stress for SAC305 Bulk Solder

Figure 4.11 and 4.12 (a) and (b) contain the typical strain rate vs. applied stress responses for SAC305 joints #1and #2 respectively. Each curve in these plots represents a fit of the Exponential and Garofalo creep model to the nanoindentation creep data. Since the nanoindentation compressive stress levels during the creep experiments were typically above 50 MPa, these results are extrapolations for the stress levels below this level. The red data points in each plot are creep strain rates measured by separate tensile testing of extremely small uniaxial specimens. These specimens are 1 mm wide and had a gage length of 10 mm, and polarized light microscopy revealed that they were composed of 10 or less grains (Figure 4.13). The agreement of the creep curves from nanoindentation with the small scale specimen tensile creep data is very good at the lower stress levels, suggesting that proposed extrapolation procedure has the potential to yield accurate predictions. Numerical values of the creep strain rates have been extracted from Figure 4.11 for SAC305 joints with an applied stress level of $\sigma = 15$ MPa. The results are tabulated in Table 2 along with the observed strain rates for $\sigma = 15$ MPa found through tensile creep testing of the small 10 mm uniaxial samples (data points in Figure 4.11). In addition, the creep rates we measured in prior studies [38-39 and 41] by tensile testing of longer (80-100 mm) miniature bulk uniaxial samples are also included. This can be explained from the single grain/crystal nature of the joint samples and the small number of grains (<10) present in the small tensile specimens which reduces the grain boundary sliding creep.

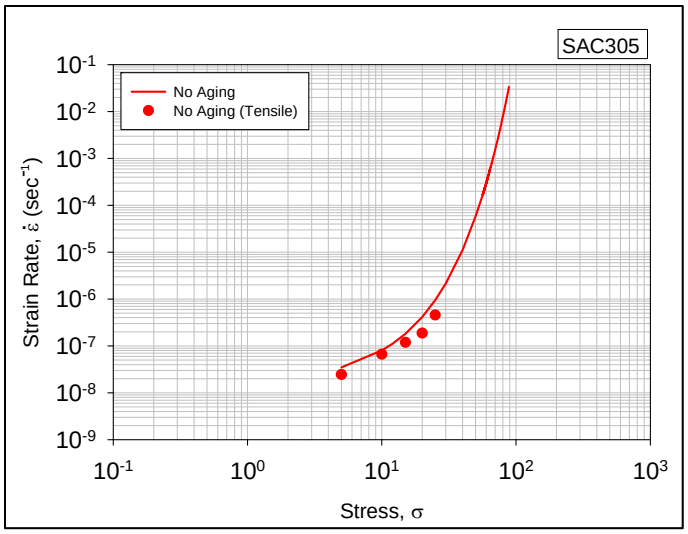

(a)

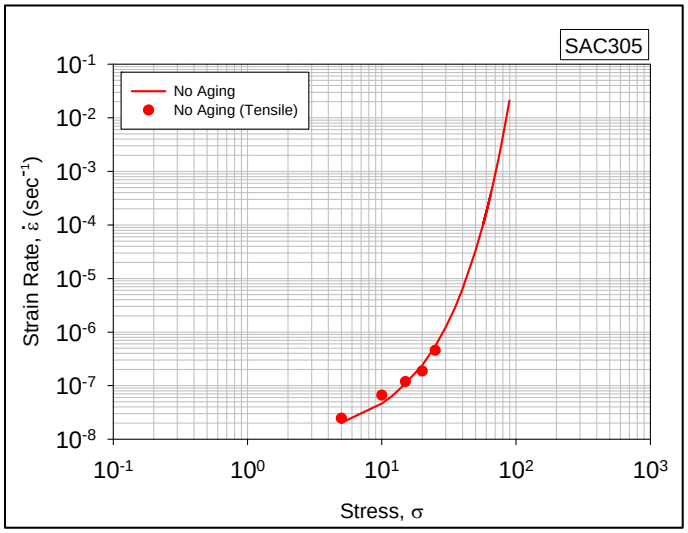

(b)

Figure 4.11 Creep Strain Rate vs. Stress for SAC305 Solder Joints # 1 and 2 using Exponential Creep Model

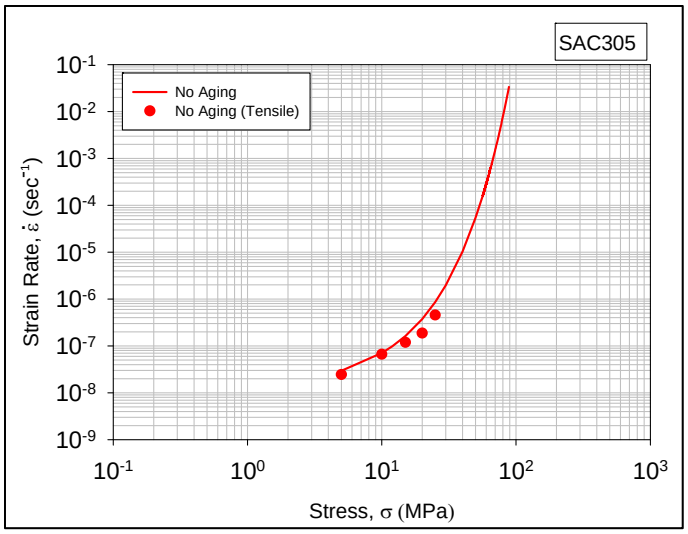

(a)

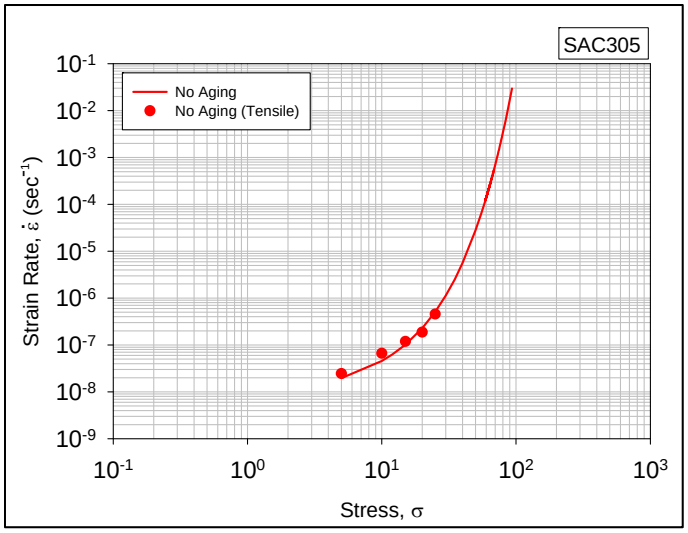

(b)

Figure 4.12 Creep Strain Rate vs. Stress for SAC305 Solder Joints # 1 and 2 using Garofalo Creep Model

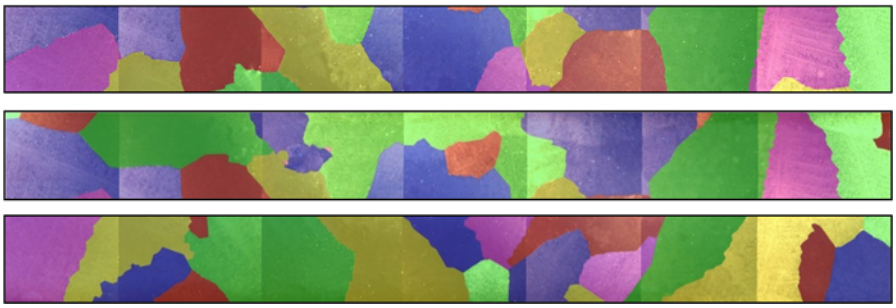

Figure 4.13 Grain Structure of Small Uniaxial Sample

Table 4.2 Nanoindentation Creep Strain Rate and Uniaxial Creep (σ = 15 MPa)

Property	Joint # 1	Joint # 2	Tensile (Small)	Tensile (Large)
Creep	1.82×10^{-7}	1.05×10^{-7}	1.19×10^{-7}	3.6×10^{-8}
Crystal Orientation	(1 5 -6)	(1 5 10)		

Another observation from creep data is that along with elastic properties plastic property and creep strain rate are also highly anisotropic. As stated earlier, two joints were tested with different orientation. However, the creep strain rate in solder joint # 1 is higher than solder joint # 2 because of their crystallographic orientation. As seen earlier the hardness in joint # 1 is much lower than joints # 2. As hardness is essentially the ability to resist plastic deformation, it can be expected that joint # 1 is more prone to plastically deformation the (1 5 -6) crystallographic plane. These findings also suggest different creep deformation behaviors for different crystal planes and may offer a practical application in designing soldering processes to obtain preferred solder joint orientations.

4.5 Creep Mechanism

Creep strain rate is plotted against the indentation stress on double logarithmic scale. The stress exponent (n) can be determined by linear regression fitting. A power law fit to the data yields a slope of 7.91 (Figure 4.14). This stress exponent for indentation creep is

consistent with the reported value from the uniaxial tensile creep [69 and 90]. It is suggested that when power law is valid under the experimental condition, stress exponent can be used to identify the mechanism controlling the creep deformation. Stress exponent value of 7.91 suggests that dislocation climb may be the operating mechanism for indentation creep [24]. And this might be true for single mechanism.

Figure 4:14 Log-log Plot of Strain Rate vs. Stress

4.6 Summary and Discussion

The relationship between crystal orientation and mechanical properties of single grain SAC305 solder joints have been quantified and correlated with the magnitudes observed in tensile testing of miniature bulk specimens using nanoindentation and EBSD. A strong anisotropy in hardness, modulus and creep was found which might help to predict the reliability of the solder joints. However, due to the single grain nature of the joints considered in this study, the creep response was significantly less in the solder joints

relative to larger uniaxial tensile specimens. The test results show that elastic, plastic and creep properties of the solder joints are highly dependent on the crystal orientation. In addition, an approach has been developed to predict tensile creep strain rates for low stress levels using nanoindentation creep data measured at very high compressive stress levels. Our findings also enlighten the interpretation of nanoindentation creep data into uniaxial creep. Dislocation climb has been suggesting the operative creep deformation mechanism.

CHAPTER 5

CHARACTERIZATION OF AGING EFFECTS IN SAC305 SOLDER JOINTS

5.1 Introduction

In this chapter, aging phenomena in actual solder joints have been explored by nano-mechanical testing of single SAC305 lead free solder joints extracted from PBGA assemblies. Using nanoindentation techniques, the stress-strain and creep behavior of the SAC305 solder materials have been explored at the joint scale for various aging conditions. Mechanical properties characterized as a function of aging include the elastic modulus, hardness, and yield stress. Using a constant force at max indentation, the creep response of the aged and non-aged solder joint materials has also been measured as a function of the applied stress level. With these approaches, aging effects in solder joints were quantified and correlated to the magnitudes of those observed in testing of miniature bulk specimens. Additional testing has been performed on very small tensile specimens with approximately 10 grains, and the aging-induced creep rate degradations in bulk samples were correlated with those observed in the nanoindentation creep data from single grain joints.

Along with the study of aging effects on mechanical properties of solder joints, it is also necessary to examine the aging induced microstructure evolution. Therefore, this chapter, microstructural coarsening during isothermal aging will be discussed also.

5.2 Aging Studies on SAC305 Solder Joints

To avoid having the nanoindentation results vary across a solder joint when making several indents under the same aging conditions, testing has been limited to single grain solder joints. In initial testing, the aging induced changes in mechanical behavior of two unique single crystal SAC 305 solder joints were examined. SEM photos of the two joints are shown in Figure 5.1. For each joint, 7 unique sets of aging conditions were explored: no aging; and 10, 30, 90, 180, 270, and 360 days of aging at T = 125 C. For each aging condition, a 2 x 3 array of indentations was performed on each joint, and Figure 5.2 illustrates the conceptual map of the 7 indentation regions for the various aging conditions across each solder joint. All of the BGA test boards were stored in a freezer at T = -10 C prior to cross-sectioning to minimize any aging effects after board assembly. Aging of the epoxy mounted samples was then performed in a box oven, and light polishing was performed to remove any oxides after each oven exposure. For each aging condition and solder joint, the individual and average results for the 6 indentations have been reported for the elastic modulus, hardness, and creep strain rate vs. stress curves. The sample preparation, testing, measurement and processing of nanoindentation load vs. displacement data for lead free solders are also discussed in detail in chapter 3 and 4.

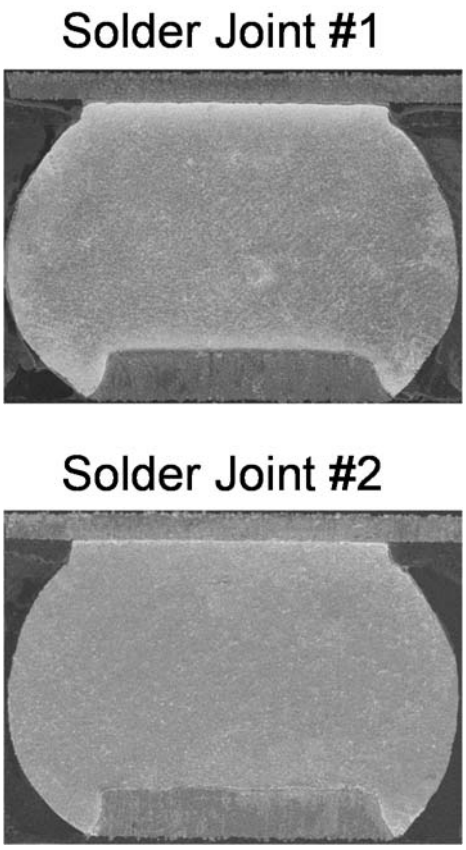

Figure 5.1 SAC305 Solder Joints Sample for Aging Studies

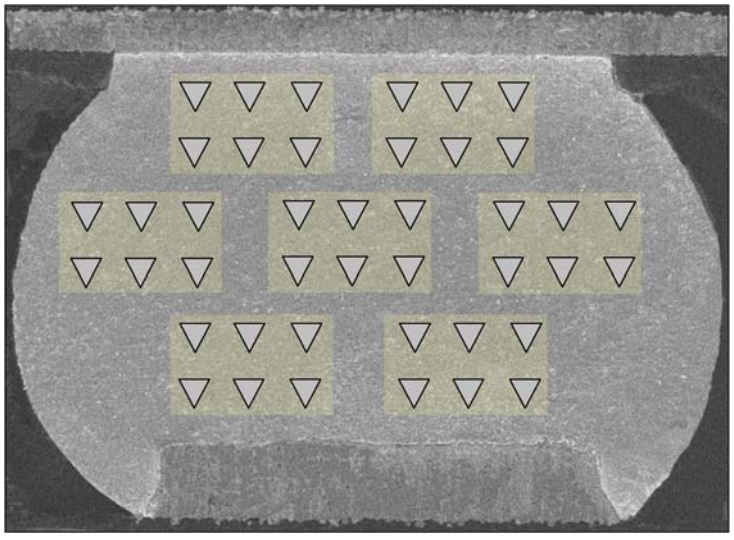

Figure 5.2 Indentation Regions for Various Aging Conditions

5.3 Effect of Aging on Elastic Modulus and Hardness

Using the nanoindentation procedures discussed in chapter 3 and 4, the CSM method was used to measure elastic modulus and hardness values for the 6 indents performed for each aging condition on each solder joint. For example, the measured average values for the two SAC305 joints are listed in table 5.1 and 5.2.

Table 5.1 Elastic Modulus Values from Nanoindentation

Aging Time (Days)	Elastic Modulus (GPa)	
	Joint #1	Joint #2
0	50.25 (0.54)	55.59 (1.98)
10	45.65 (1.45)	46.52 (2.32)
30	40.95 (0.45)	41.84 (1.33)
90	37.63 (1.79)	39.40 (1.48)
180	36.59(1.89)	38.91(0.91)
270	36.21(1.62)	38.54(1.41)
360	36.09(0.48)	38.13(2.06)

Table 5.2 Hardness Values from Nanoindentation

Aging Time (Days)	Hardness (GPa)	
	Joint #1	Joint #2
0	0.310 (0.021)	0.340 (0.008)
10	0.257 (0.015)	0.264 (0.019)
30	0.210 (0.009)	0.220 (0.018)
90	0.198 (0.013)	0.202 (0.010)
180	0.191(0.012)	0.198(0.02)
270	0.186(0.01)	0.195(0.007)
360	0.181(0.01)	0.193(.006)

As expected from the crystal orientation results presented in chapter 3, the mechanical properties of joint #2 were slightly larger than those for joint #1 for all aging times. It is observed that for 360 days of aging at 125 C, that the elastic modulus of solder balls #1 and #2 degraded by 28.2% and 31.4%, respectively. The corresponding degradations of the hardness over the same period were 41.6% and 43.2%. These

percentage reductions with 360 days of aging at 125 C are very similar to those observed for the elastic modulus (34.4%) and yield stress (44.1%) of SAC305 measured by tensile testing of larger multi-grain uniaxial samples in our prior aging investigations [38-43]. The uniaxial samples from prior investigations have been examined using polarized light microscopy, and are known to contain hundreds of grains with a variety of orientations.

Plots of the mechanical property evolution with aging time for the two SAC305 joints are presented in Figures 5.3 and 5.4. The evolutions of the mechanical properties with aging were well fit using linear and exponential decay empirical models:

$$E = C_0 + C_1 t + C_2 e^{-C_3 t} \tag{5.1}$$

$$H = C_0 + C_1 t + C_2 e^{-C_3 t} \tag{5.2}$$

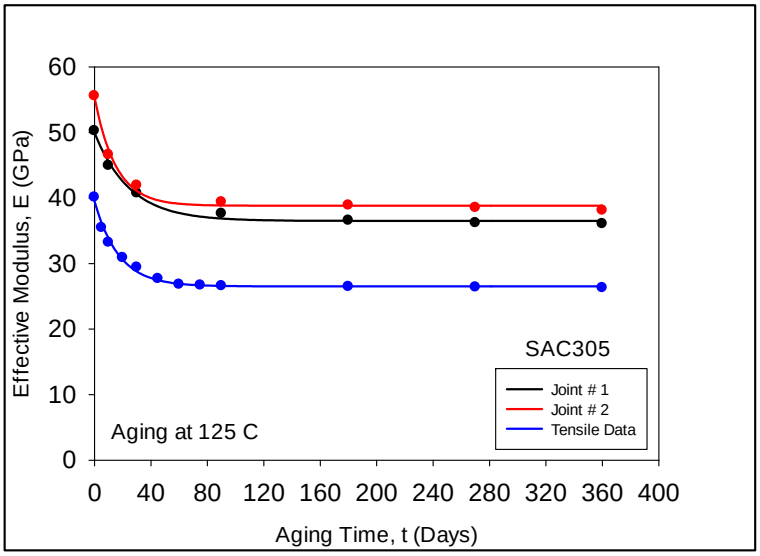

Figure 5.3 Evolution of Elastic Modulus with Aging Time
(SAC305, Aging at 125 C)
Tensile Data from Reference [41]

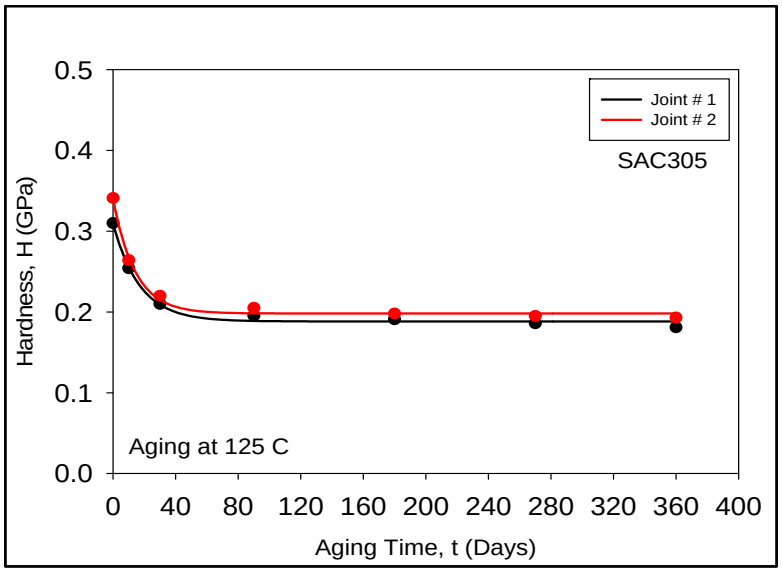

Figure 5.4 Evolution of Hardness with Aging Time
(SAC305, Aging at 125 C)

where C_0, C_1, C_2, C_3 are regression constants. The majority of the property degradations in the SAC305 solder joints occurred within the first 20-30 days of aging in an exponential manner. After this point, the variations are small and can be fit with a linear decay. These observations are in agreement with our aging results for testing of larger solder tensile specimens [38-43]. In addition to the nanoindentation results from the current paper, tensile testing results (blue curve) from prior studies have been added from multi-grain SAC305 samples to the elastic modulus and yield stress data in Figure 5.3 and 5.5. Tabor hardness formula was used to estimate the yield stress data from nanoindentation test.

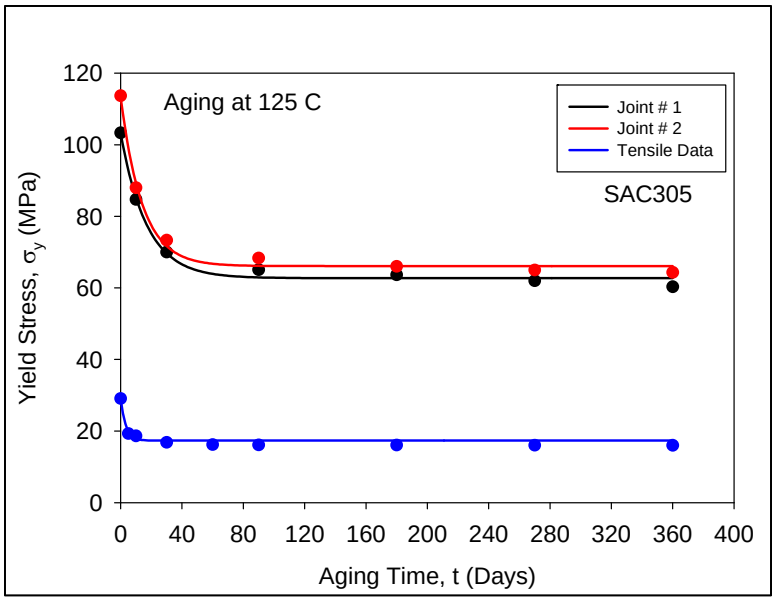

Figure 5.5 Evolution of Yield Stress Degradation with Aging

It is observed that the modulus and yield stress variations are qualitatively similar in shape. The percentage reductions are ~30-35% after 360 days of aging at 125 C for both the solder joint nanoindentation and miniature bulk tensile test results as discussed above. The magnitudes of the modulus at the joint-scale are significantly larger than those of the tensile samples for all aging times. This is not unexpected due to the single grain nature of the solder joints tested. As discussed in chapter 3, the two tested SAC305 joints both had their out-of-plane orientations near the (001) direction of β-Sn. This orientation has a modulus of 67.6 GPa, which is at the upper limit of the range ($23.6 < E < 67.6$) of values possible when considering all crystal orientations. It has been established that the miniature bulk tensile specimens (80-100 mm in length) are typically composed to hundreds of grains with a variety of orientations. Thus, the modulus of the tensile specimens will be significantly smaller and highly averaged, on the order the average/mid-

point of the modulus spectrum for β-Sn. The same is true for yield stress which is shown in Figure 5.5.

5.4 Effect of Aging on Creep Response

Using the nanoindentation creep procedures discussed above, the evolution of the creep response with aging at 125 C was characterized for each of the two solder joints. For all of the tests, a constant peak load of 30 mN and a dwell time of 900 sec were used during the hold periods. Using the recorded creep displacement vs. time data, the creep strain rate vs. applied stress curves were generated. Figure 5.6 shows the aging dependence of the maximum creep displacements in the two SAC305 joints that occurred after 900 sec of constant load. It is observed that higher creep displacements occurred in joint # 1 relative to joint # 2 for each of the aging times. This result agrees with the earlier observations that joint # 1 will have poorer mechanical properties and creep response than joint # 2 due to its single grain orientation normal to the polished surface being further away from the (001) direction of β-tin.

Figures 5.7-5.8 contain the strain rate vs. applied stress responses for SAC305 joints #1 and #2, respectively. Each curve in these plots represents a fit of the exponential creep model to the nanoindentation creep data as outlined in chapter 4. Since the nanoindentation compressive stress levels during the creep experiments were typically above 50 MPa, these results are extrapolations for the stress levels below this level. The red curves in these graphs are for the no aging case, and represent the best (lowest) creep strain rates occurring in the joints.

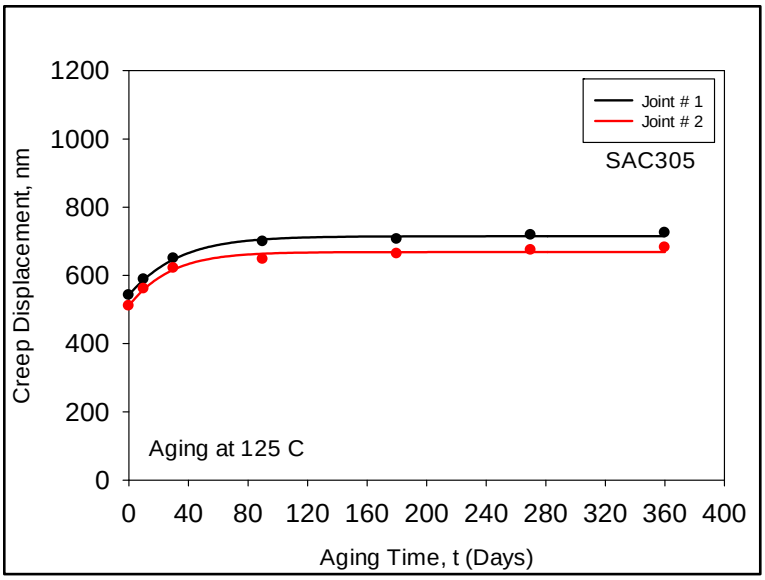

Figure 5.6 Maximum Creep Displacement vs. Aging Time (SAC305, Aging at 125 C)

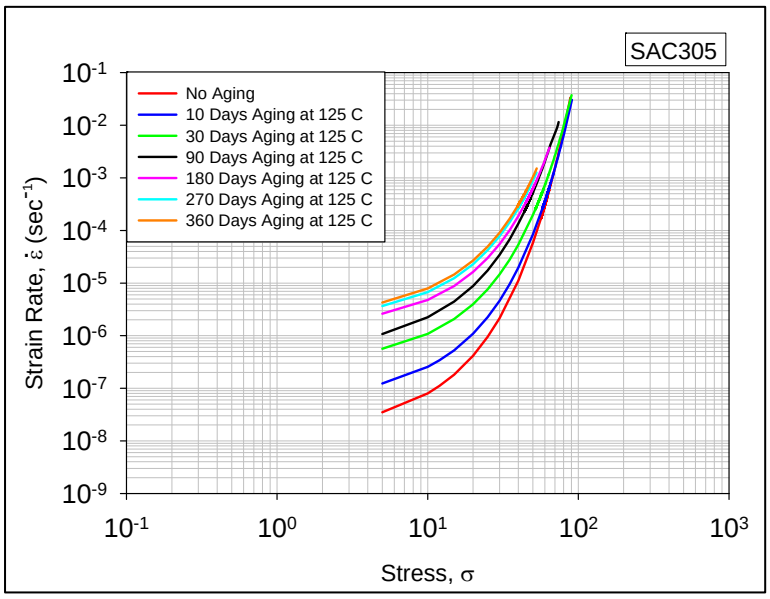

Figure 5:7 Creep Strain Rate vs. Stress for Joint #1 (SAC305, Aging at 125 C)

As aging progressed, the creep strain rates became much larger in each joint for every stress level, pushing the creep response curves significantly higher (blue, green, black, pink, light blue, and orange curves for prior aging at 125 C for 10, 30, 90, 180, 270, and 360 days).The largest changes occurred in the first 30 days of aging, and the changes between 30 and 360 days were significantly reduced.

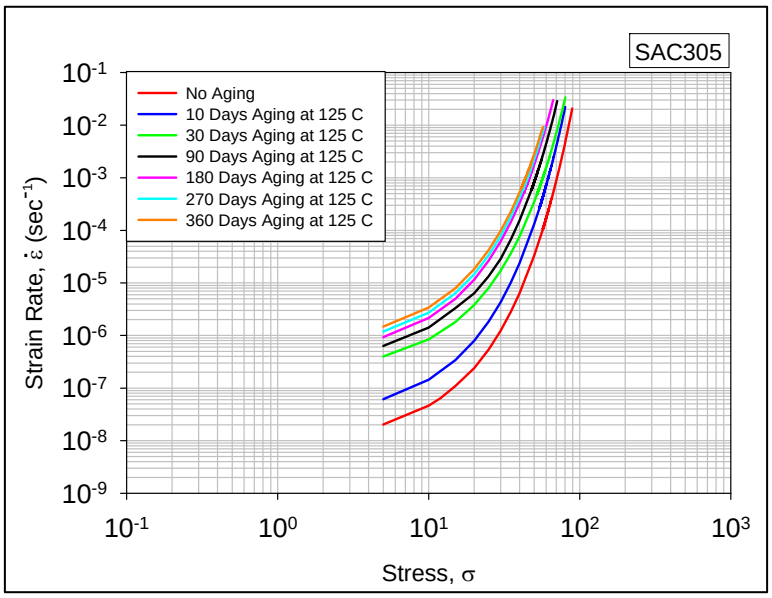

Figure 5.8 Creep Strain Rate vs. Stress for Joint #2
(SAC305, Aging at 125 C)

5.4.1 Effects of Aging on Uniaxial Creep and Correlate to Nanoindentation Creep

To validate the potential use of the creep model, uniaxial creep testing has been done by applied stress of σ = 5, 10 and 15 MPa for sample aged up to 360 days. Details of the testing procedure and data processing has been described in Chapter 3 and 4.

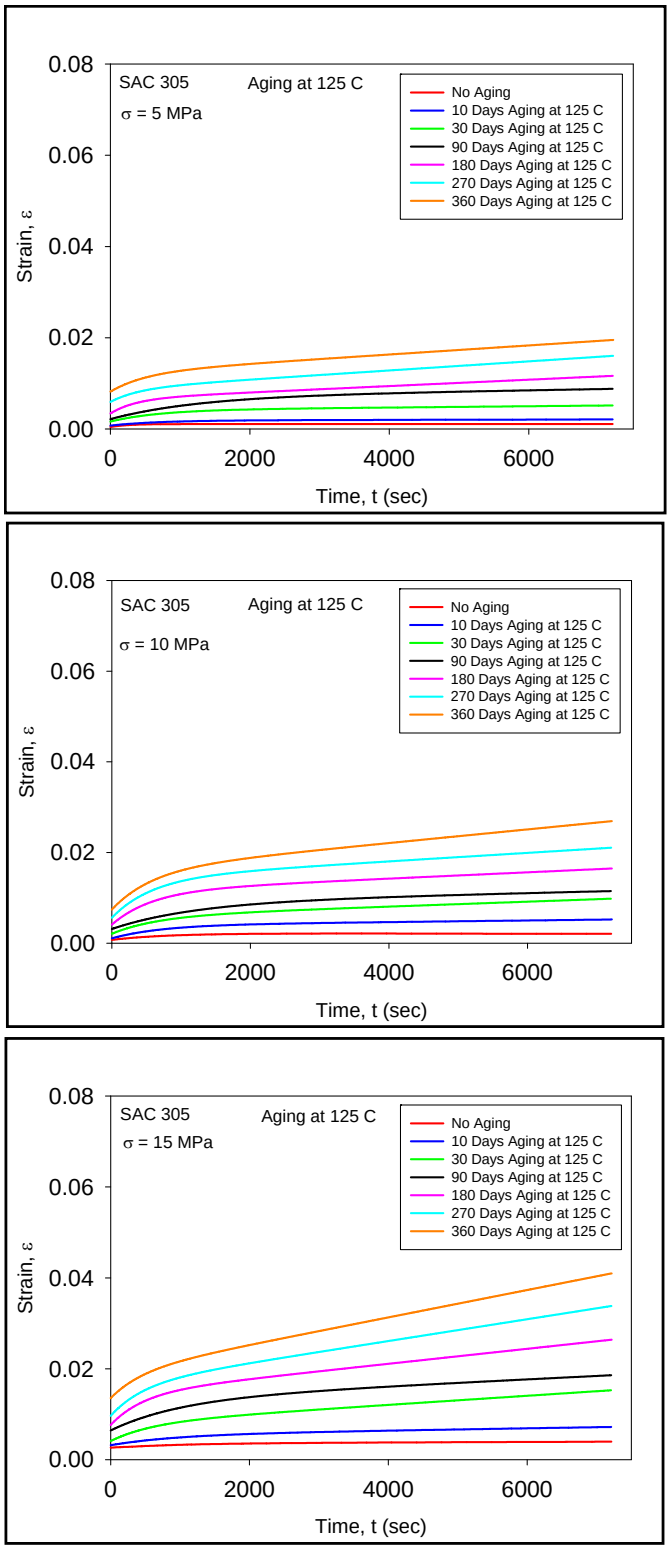

Figure 5.9 Creep Strain vs. Time data for SAC305 Bulk Solder with Aging for Different Stress Level (Sample Dimension: 10 x 3 x 0.5 mm)

Creep testing has been performed on two extremely small specimens whose dimensions are 10 x 3 x 0.5 mm and 10 x 1 x 0.5 mm, respectively. By doing that the influence of sample dimensions on the measured uniaxial creep response have been compared.

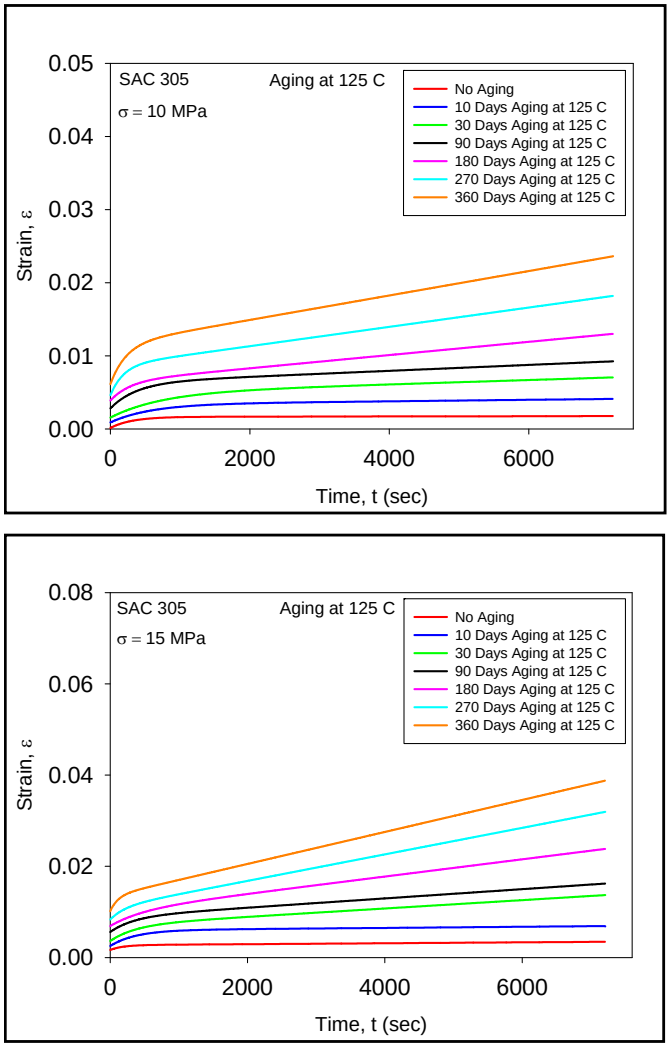

Figure 5.10 Creep Strain vs. Time data for SAC305 Bulk Solder with Aging for Different Stress Level (Sample Dimension: 10 x 1 x 0.5 mm)

Figure 5.9 and 5.10 shows the strain vs. time data for SAC305 bulk solder for the dimensions, 10 x 3 x 0.5 mm and 10 x 1 x 0.5 mm, respectively. Corresponding creep

strain rate versus stress is fitted with the Garofalo model [23] and plotted in Figure 5.11 and 5.12. A direct comparison of the creep strain vs time for the SAC305 small tensile specimens are shown in Figure 5.13 and 5.14, for stress level 10 and 15 MPa, respectively.

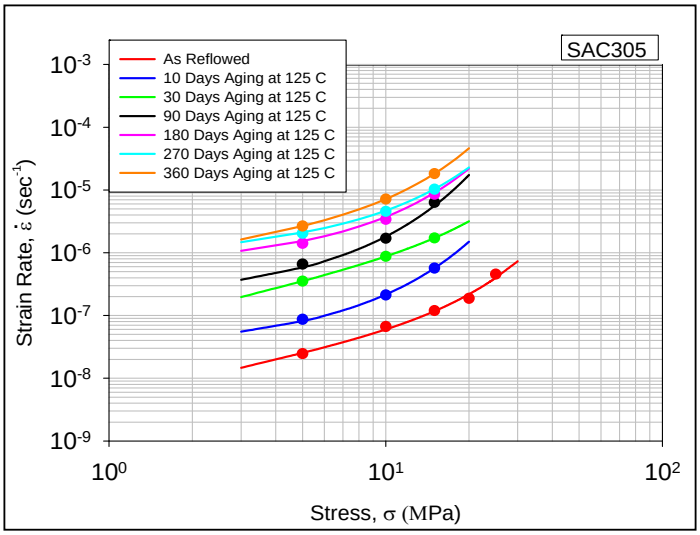

Figure 5.11 Creep Strain Rate vs. Stress data for SAC305 Bulk Solder with Aging for Different Stress Level (Sample Dimension: 10 x 3 x 0.5 mm)

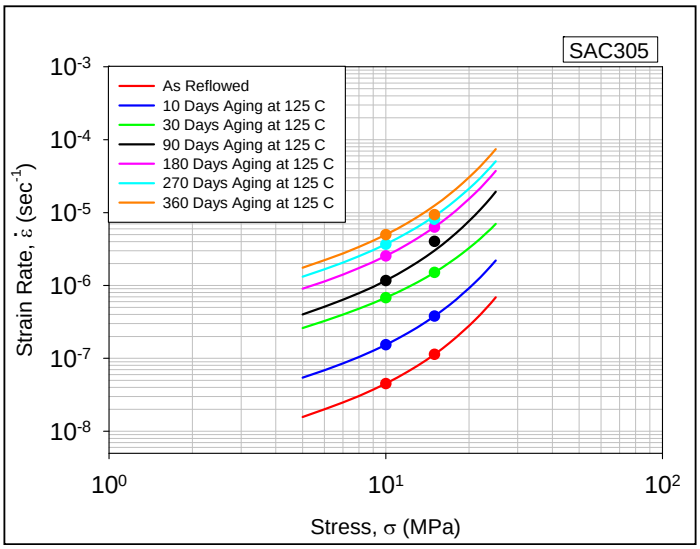

Figure 5.12 Creep Strain Rate vs. Stress data for SAC305 Bulk Solder with Aging for Different Stress Level (Sample Dimension: 10 x 1 x 0.5 mm)

It can be seen that that decreasing the sample dimension results in decreasing creep strain rate. On the other hand larger tensile specimens exhibited much larger aging induced increase in the creep rate. The observed effects of sample configuration on the creep will be explained based on increased grain boundary sliding mechanism in the following section.

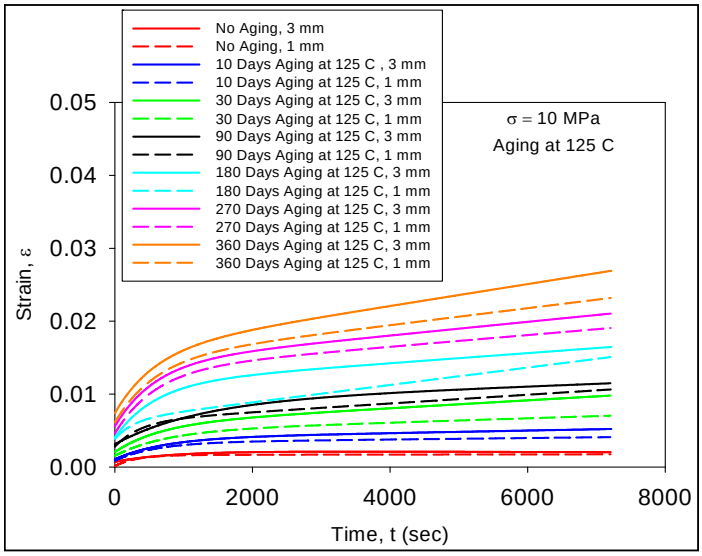

Figure 5.13 Influence of Sample Dimensions on Uniaxial Creep (σ = 10 MPa)

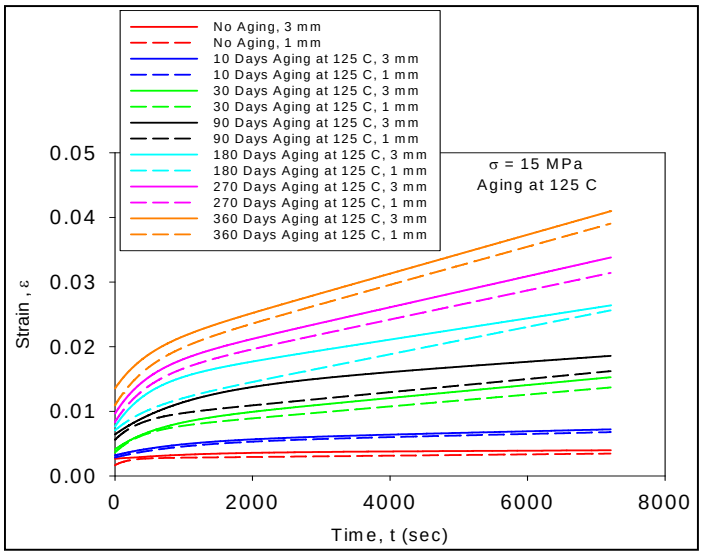

Figure 5.14 Influence of Sample Dimensions on Uniaxial Creep (σ = 15 MPa)

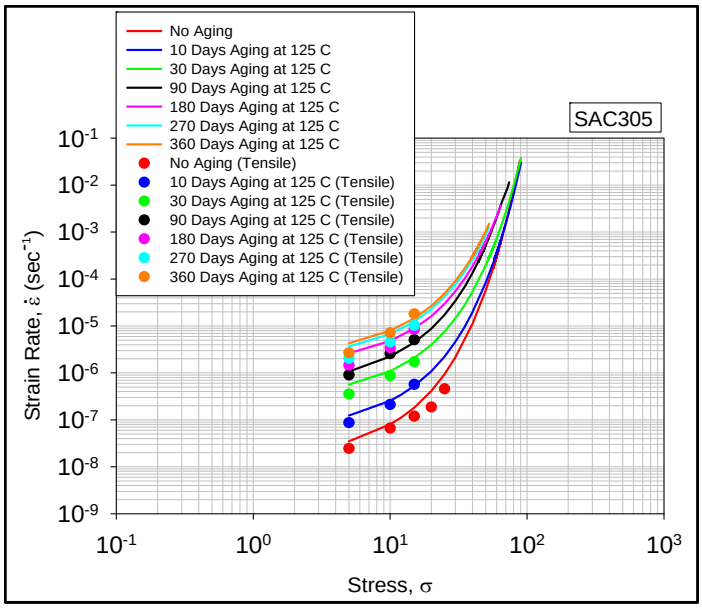

(a) Uniaxial (medium)

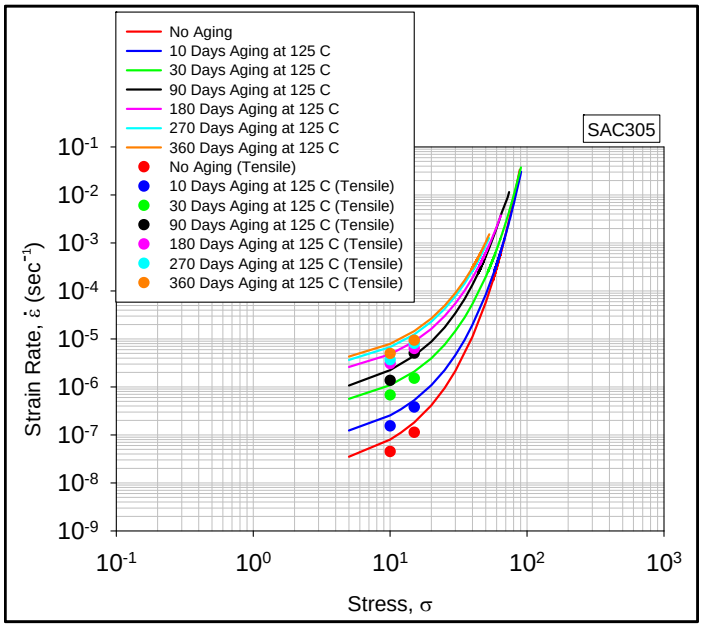

(b) Uniaxial (small)

Figure 5.15 Creep Strain Rate vs. Stress for Joint #1 (SAC305, Aging at 125 C)

Now, with those approaches aging effects in solder joints were correlated to the magnitudes of those observed in testing of miniature bulk specimens. Figures 5.15-5.16 illustrated the strain rate vs. stress responses for SAC305 joints #1 and #2 that include the uniaxial creep data for two extremely small specimens.

The red, blue, green, black, pink, light blue and orange data points in each plot are creep strain rates measured by separate tensile testing of extremely small uniaxial specimens that were aged for 0, 10, 30, 90, 180, 270 and 360 days, respectively. These specimens had a gage length of 10 mm, and polarized light microscopy revealed that they were composed of 10 or less grains.

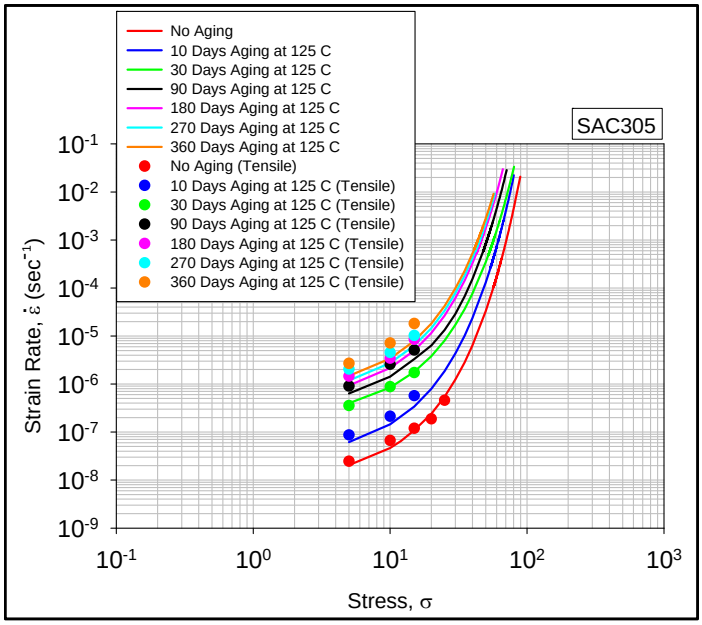

(a) Uniaxial (medium)

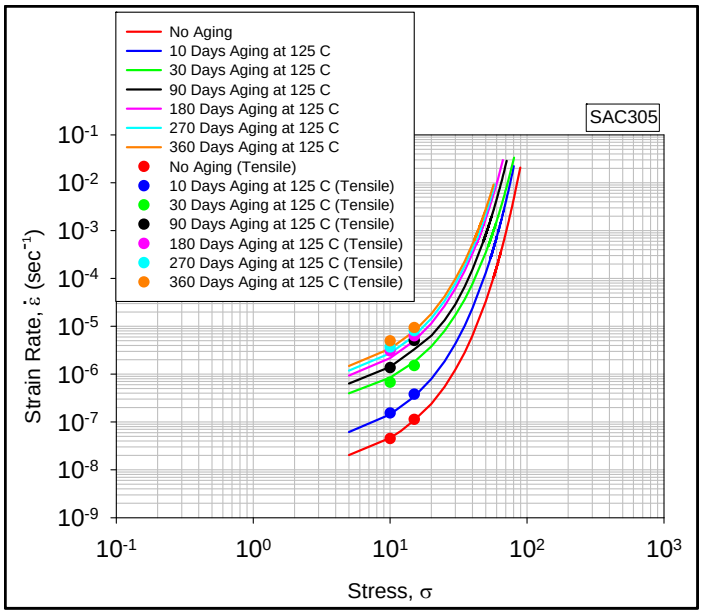

(b) Uniaxial (small)

Figure 5.16 Creep Strain Rate vs. Stress for Joint #2
(SAC305, Aging at 125 C)

The increases in the creep stain rates observed for the two joint samples were similar and on the same order as those measured for the small 10 mm tensile specimens. The agreement of the creep curves from nanoindentation with the small scale specimen tensile creep data is very good at the lower stress levels, suggesting that proposed extrapolation procedure has the potential to yield accurate predictions.

Table 5.3 Creep Rate Changes with Aging (SAC305)

Aging Time (Days)		Creep Strain Rate (sec^{-1}) for σ = 15 MPa			
	Joint #1	Joint #2	Tensile (Medium)	Tensile (Small)	Tensile (Large) Refs. [4-5]
0	1.82×10^{-7}	1.05×10^{-7}	1.19×10^{-7}	1.13×10^{-7}	0.36×10^{-7}
10	5.26×10^{-7}	3.38×10^{-7}	2.11×10^{-7}	2.99×10^{-7}	2.57×10^{-7}
Increase	2.89X	3.21X	1.77X	2.64X	7.14X
30	2.07×10^{-6}	1.79×10^{-6}	1.72×10^{-6}	1.51×10^{-6}	5.90×10^{-6}
Increase	11.4X	17.0X	14.4X	13.36X	164.9X
90	5.89×10^{-6}	3.23×10^{-6}	5.11×10^{-6}	4.02×10^{-6}	8.14×10^{-6}
Increase	32.4X	30.8X	42.94X	35.57X	226.1X
180	8.84×10^{-6}	4.98×10^{-6}	8.54×10^{-6}	6.32×10^{-6}	12.9×10^{-6}
Increase	48.57X	47.44X	71.76X	55.93X	358.3X
270	1.25×10^{-5}	6.34×10^{-6}	1.03×10^{-5}	8.07×10^{-6}	21.0×10^{-6}
Increase	66.68X	60.38X	87.33X	71.40X	583.3X
360	1.45×10^{-5}	7.90×10^{-6}	1.65 x 10-5	8.39×10^{-6}	33.0×10^{-6}
Increase	77.54X	75.23X	138.65X	74.25X	916.7X

Numerical values of the creep strain rates have been extracted from Figures 5.15-5.16 for SAC305 joints with no-aging and with 10, 30, 90, 180, 270, and 360 days aging at 125 C, and for an applied stress level of σ = 15 MPa. The results are listed in Table 5.3 along with the observed strain rates for σ = 15 MPa found through tensile creep testing of the small 10 mm uniaxial samples (data points in Figures 5.15-5.16).

In addition, the creep rates we measured in prior studies [38-39] by tensile testing of longer (80-100 mm) miniature bulk uniaxial samples are also included. The increases in the creep stain rates observed for the two joint samples were similar and on the same order as those measured for the small 10 mm tensile specimens. For example, after 90 days of aging the two joints had increases of 32.4X and 30.8X, while the creep rate of the

medium and small tensile specimens increased by 42.9X and 35.57X, respectively. However, dramatically different results were obtained for the longer miniature bulk tensile samples, where an increase in the creep rate of 226.1X was observed. Thus, there were significantly more aging induced degradations in the larger bulk solder tensile samples relative to the joint samples and small tensile specimens. As discussed below, this can be explained from the single grain/crystal nature of the joint samples and the small number of grains (<10) present in the small tensile specimens that were tested. A direct comparison of the creep rate degradations for the SAC305 solder joints (average) and the SAC305 small and medium tensile specimens is shown in Figure 5.17. Good agreement was observed for all aging times although small tensile specimens matches the solder joint creep data with little variations.

Typical sources of creep in metals are matrix creep and grain boundary creep. Since the single crystal SAC305 joints in question had no grain boundaries, they primarily experienced matrix creep. In particular, aging causes growth of the intermetallic particles (Ag_3Sn and Cu_6Sn_5) in the β-Sn matrix of a single grain SAC solder joint. As the intermetallic particles are coarsened, they cannot resist the movement of dislocations and thus there is a loss of strength.

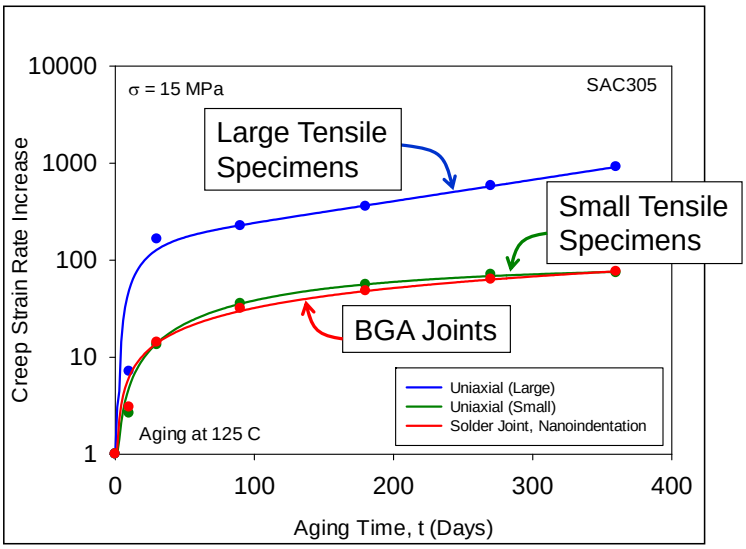

Figure 5.17 Creep Strain Rate Degradations with Aging
(SAC305, Aging at T = 125 C)
(NI and SAC305 Small Tensile Specimens)

In addition, coarsened particles are considerably softer, and as a result, the dislocations can pass the particles more easily leading to increased creep deformations. The miniature bulk tensile samples have hundreds of grains, and experience significant grain boundary creep mechanisms such as grain boundary sliding. These effects can be significantly curtailed in lead free solders by migration of intermetallic particles to the grain boundaries providing pinning. While, the presence of only a single grain in a solder joint has been shown to significantly reduce the degradations in the creep response with aging, the magnitude of aging effects in multi-grain lead free solder joints remains to be quantified.

5.5 Effects of Aging on Microstructure

Degradations of mechanical and creep properties of lead free solders are caused by microstructure evolution as illustrated in Figure 5.18 for one of the SAC305 joints in this

study. The typical microstructure of SAC joints consists of primary Sn cells with Ag_3Sn and Cu_6Sn_5 particles that result from binary eutectic decompositions at the cell boundaries.

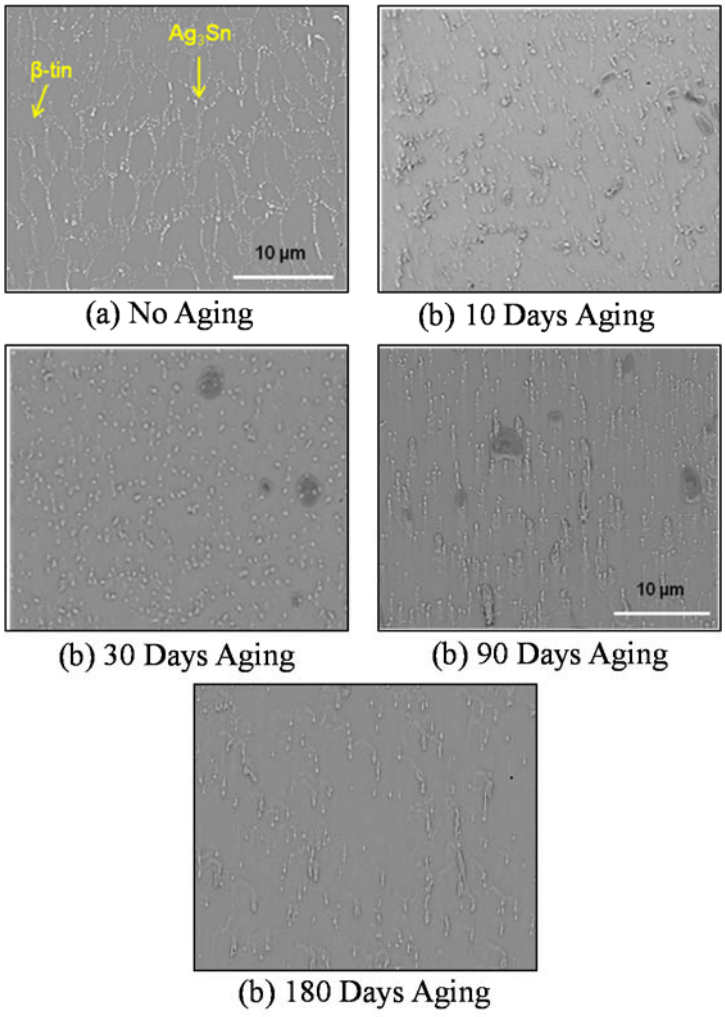

Figure 5.18 Microstructural Evolution of a SAC305 Solder Joint Subjected to Aging at 125C

During isothermal aging, Ag_3Sn precipitates coarsen or ripen, which results in fewer but larger particles. The Sn cell size grows significantly, but boundaries are no longer well defined due to coarsening. Sn cell boundaries are most likely are low angle subgrain boundary decorated by Ag_3Sn precipitates.

There are relatively few Cu_6Sn_5 particles compared to the Ag_3Sn particles, and they were observed to be distributed randomly. Coarsening of the particles is caused by the diffusion, which is accelerated during isothermal aging since diffusion is a thermally activated process. Finer scale Ag_3Sn before aging are able to interact more with dislocations and minimized grain boundary sliding. Thus, coarsening will degrade the creep behavior of the solder joints as well as the reliability of the package.

5.6 Summary and Discussion

In this chapter, nanoindentation techniques have been used to measure the elastic, plastic, and creep behavior of the SAC305 solder joint materials for various aging conditions. The measured results have demonstrated that the mechanical behavior of actual solder joints degrade significantly with aging. The results show that the aging induced degradations of the mechanical properties (modulus, hardness) in the SAC joints were of similar order (30-40%) as those seen previously in the testing of larger "bulk" uniaxial solder specimens. The creep rate of the tested SAC305 joints were found to increase by up to 75X with one year of aging. These degradations, while significant, were much less than those observed in larger bulk solder uniaxial tensile specimens with several hundred grains, where the increase was over 900X. Additional testing has been performed on very small tensile specimens with approximately 10 grains, and the aging-induced creep rate degradations found in these specimens were on the same order of magnitude as those observed in the single grain joints. Thus, the lack of the grain boundary sliding creep mechanism in the single grain joints is an important factor in avoiding the extremely large creep rate degradations occurring in larger bulk SAC samples.

The test results also show that the elastic, plastic, and creep properties of the solder joints and their sensitivities to aging are highly dependent on their crystal orientations. Polarized light microscopy and Electron Back Scattered Diffraction (EBSD) were used to identify the grain structure and crystal orientations in the tested joints. Microstructural analysis of the joints has shown that Ag_3Sn precipitates coarsen during isothermal aging, which results in fewer but larger particles. The Sn dendrite cell size also was observed to grow significantly, but the boundaries are no longer well defined due to coarsening.

CHAPTER 6

THE EFFECTS OF SILVER CONTENT ON THE AGING RESISTANCE OF SAC SOLDER JOINTS

6.1 Introduction

In this chapter, the effects of silver content on SAC solder aging has been evaluated by testing joints from SACN05 (SAC105, SAC205, SAC305, and SAC405) test boards assembled with the same reflow profile. In all cases, the tested joints were extracted from 14 x 14 mm PBGA assemblies (0.8 mm ball pitch, 0.46 mm ball diameter) that are part of the iNEMI Characterization of Pb-Free Alloy Alternatives Project (16 different solder joint alloys available). After extraction, the joints were subjected to various aging conditions (0 to 12 months of aging at T = 125 C), and then tested via nanoindentation techniques to evaluate the stress-strain and creep behavior of the aged SAC solder alloy materials at the joint scale.

The observed aging effects in the SACN05 solder joints have been quantified and correlated with the magnitudes observed in tensile testing of miniature bulk specimens performed in prior studies. Additional testing has been performed on very small tensile specimens with approximately 10 grains, and the aging-induced creep rate degradations found in these specimens were on the same order of magnitude as those observed in the single grain joints. Due to the variety of crystal orientations realized during solidification, it was important to identify the grain structure and crystal orientations in the tested joints.

Polarized light microscopy and Electron Back Scattered Diffraction (EBSD) techniques have been utilized for this purpose.

6.2 Aging Studies on SACN05 Solder Joints

Aging phenomena in lead free solder joints have been explored by nanoindentation testing of several SACN05 samples exposed to various aging conditions prior to testing. The SAC alloys considered were from BGA components fabricated using four different SACN05 ball alloys (SAC105, SAC205, SAC305, and SAC405). Using the nanoindentation methods detailed in chapter 3, 4 and 5, the stress-strain and creep behavior of the SACN05 solder joints have been explored for various aging conditions. The aging induced changes in mechanical behavior of single crystals solder joints have been examined included four SAC105 joints, three SAC205 joints, two SAC305 joints and three SAC405 joints. For each joint, different sets of aging conditions are being explored. The aging conditions completed to date include: no aging; and 10, 30, 90 and 180 days of aging at T = 125 C. For each aging condition, a 2 x 3 array of indentations was performed on each ball. The samples were stored in a freezer at T = -10 C prior to cross-sectioning to minimize any aging effects after board assembly. Aging of the epoxy mounted samples was then performed in a box oven, and light polishing was performed to remove any oxides after each oven exposure. Additional testing has been performed on very small bulk specimens (SAC105 and SAC305 (chapter 5)) to correlate the uniaxial creep with the nanoindentation creep. The sample preparation, testing, measurement and processing of nanoindentation and uniaxial creep data for lead free solders are also discussed in detail in chapter 3, 4 and 5.

6.3 Effect of Aging on Elastic Modulus and Hardness

Analogous Inverse Pole Figure (IPF) plots for the tested SAC105, SAC205, SAC305 and SAC405 solder joints were presented in chapter 3. Using the modulus map, it is expected that joint #1 and joint # 2 will have the largest modulus and hardness for the SAC105 and SAC305 joints, respectively. Likewise, joint #1 is expected to have the largest modulus and hardness for the SAC205 joints, and joint #2 is expected to have the largest modulus and hardness for the SAC405 joints.

The CSM method was used to measure elastic modulus and hardness values for the 6 indents performed for each aging condition on each solder joint. In case of SAC105 as expected from the crystal orientation results presented in chapter 3, the mechanical properties of joint #1 were slightly larger than those for other joints for all aging conditions. At the no aging condition, the effective modulus of the four joints varied from 50.66 GPa to 42.54 GPa with the different orientations, which demonstrated the strong crystal anisotropy of solder joints in electronic packaging. It was observed that for 180 days of aging at 125 C that the effective modulus of four joints #1, #2, #3, and #4 degraded by 22.72%, 30.62%, 31.38% and 32.92%, respectively. The corresponding degradations of the hardness over the same period were 39.80%, 42.06%, 43.12% and 45.92%. These percentage reductions with 180 days of aging at 125 C are very similar to those observed for the elastic modulus (51%) and yield stress (43.32%) of SAC105 measured by tensile testing of larger multi-grain uniaxial samples in our prior aging investigations [38-43]. The uniaxial samples from prior investigations have been examined using polarized light microscopy, and are known to contain hundreds of grains with a variety of orientations.

Plots of the mechanical property evolution with aging time are presented in Figures 6.1 and 6.2. The evolutions of the mechanical properties with aging were well fit using linear and exponential decay empirical models which were described in chapter 5. The majority of the property degradations in the solder joints occurred within the first 20-30 days of aging in an exponential manner. After this point, the variations are small and can be fit with a linear decay. These observations are in agreement with our aging results for testing of larger solder tensile specimens [38-43]. In addition to the nanoindentation results, prior tensile testing results (blue curve) have been added to the elastic modulus and yield stress data in Figure 6.1 and 6.3. Tabor hardness formula was used to estimate the yield stress data from nanoindentation test. It is observed that the modulus and yield stress variations are qualitatively similar in shape.

The percentage reductions of modulus are 25-30% after 180 days of aging at 125 C for both the solder joint nanoindentation and miniature bulk tensile test results whereas the yield stress reductions are ~43% as discussed above. However, the magnitudes of the modulus and yield stress at the joint-scale are significantly larger than those of the tensile samples for all aging times. This is not unexpected due to the single grain nature of the solder joints tested. As discussed above, the 4 tested SAC105 joints both had their out-of-plane orientations between the (101) and (100) direction of β-Sn. This orientation has a modulus of 67.6 GPa, which is at the upper end of the range ($23.6 < E < 67.6$) of values possible when considering all crystal orientations. It has been established that the miniature bulk tensile specimens (80-100 mm in length) are typically composed to hundreds of grains with a variety of orientations.

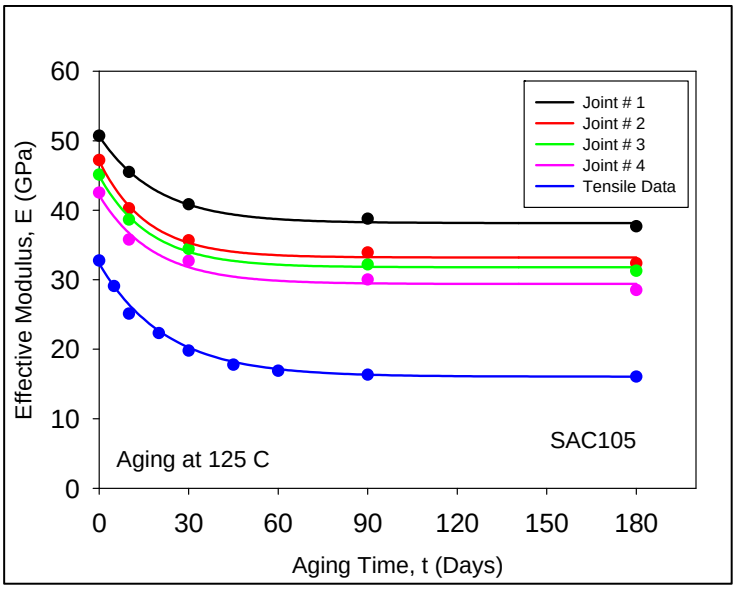

Figure 6.1 Evolution of Elastic Modulus with Aging Time
(SAC105, Aging at 125 C)

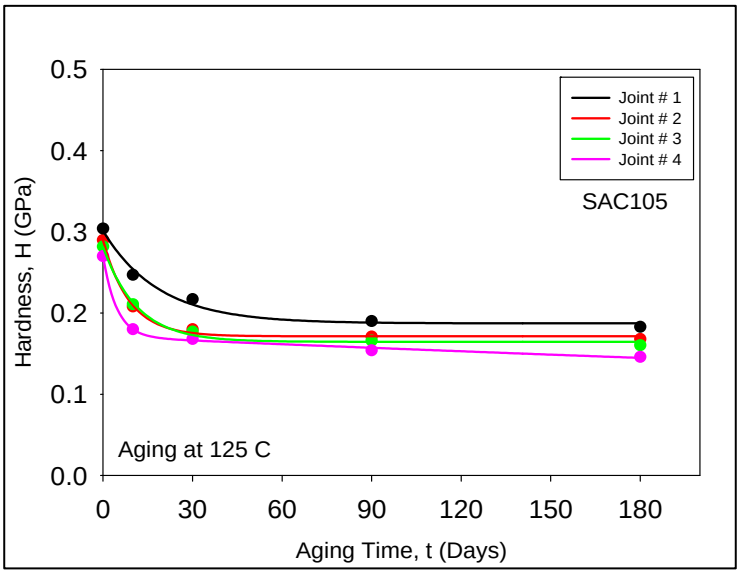

Figure 6.2 Evolution of Hardness with Aging Time
(SAC105, Aging at 125 C)

Thus, the modulus of the tensile specimens will be significantly smaller and highly averaged, on the order the average/mid-point of the modulus spectrum for β-Sn. The same is true for yield stress which is shown in Figure 6.3.

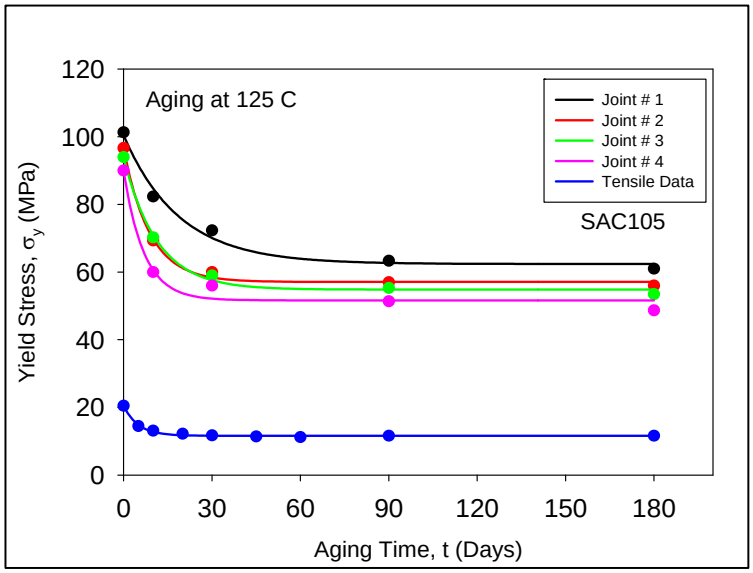

Figure 6.3 Yield Stress Degradation with Aging (SAC105)

Similar results were obtained for aging induced degradation of the three other solder alloys. The modulus, hardness and yield stress plots for the two SAC305 joints are described in chapter 5.

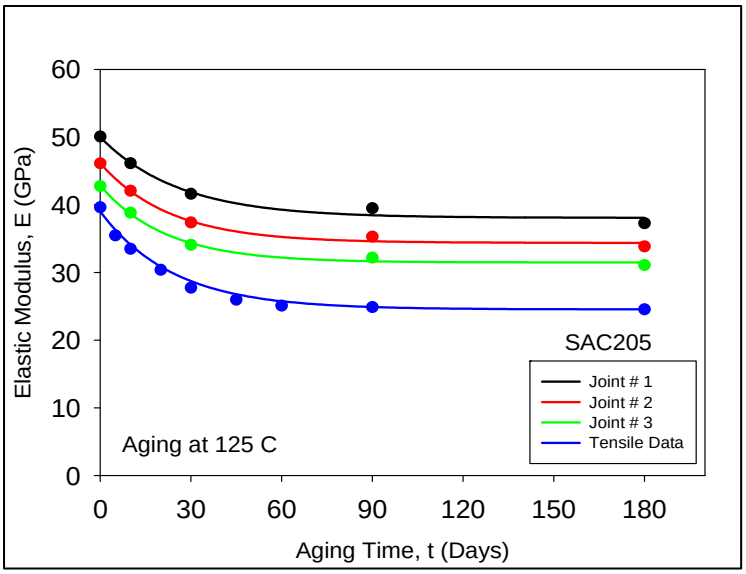

Figure 6.4 Evolution of Elastic Modulus with Aging Time (SAC205, Aging at 125 C)

For example, Figures 6.4, 6.5, and 6.6 illustrate the modulus, hardness and yield stress degradations of the three SAC205 joints with aging.

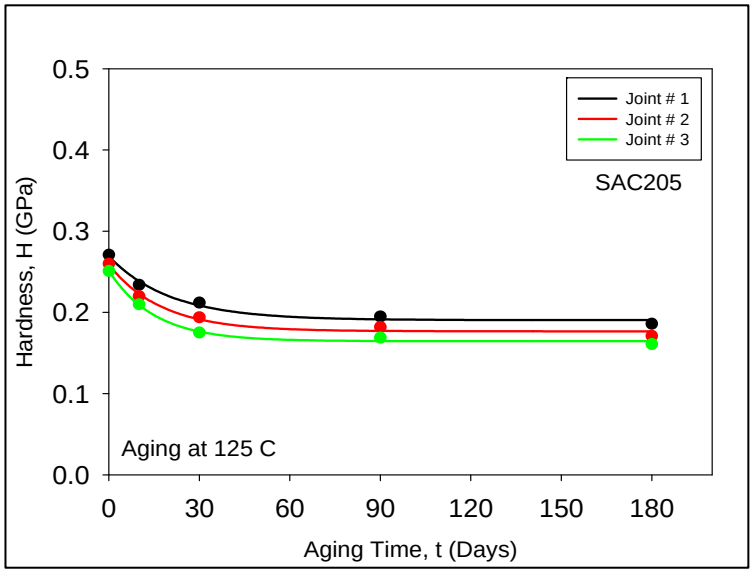

Figure 6.5 Evolution of Hardness with Aging Time (SAC205, Aging at 125 C)

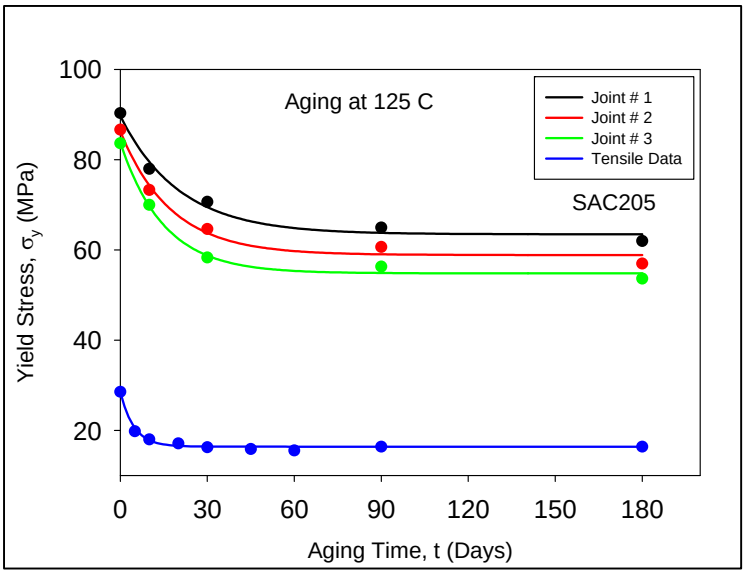

Figure 6.6 Yield Stress Degradation with Aging (SAC205)

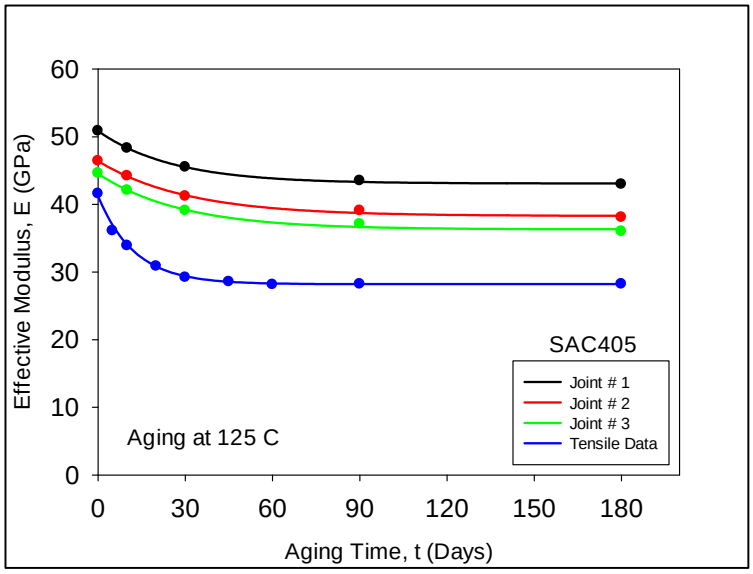

Figure 6.7 Evolution of Elastic Modulus with Aging Time (SAC405, Aging at 125 C)

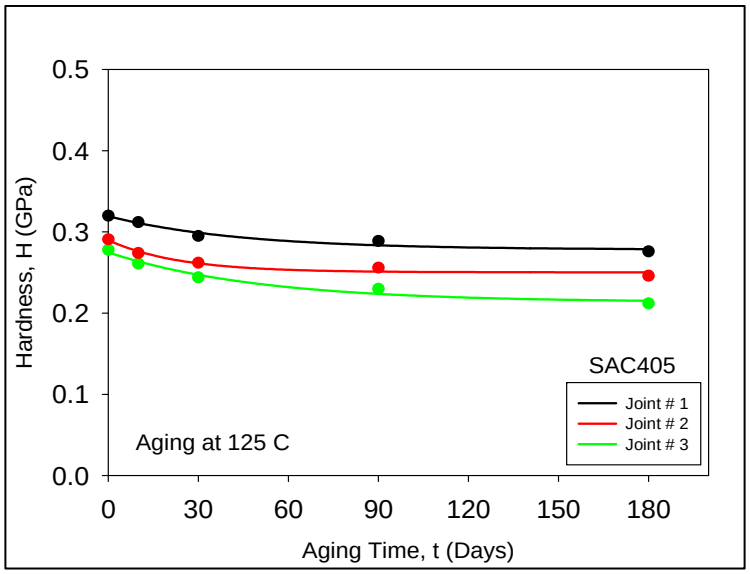

Figure 6.8 Evolution of Hardness with Aging Time
(SAC405, Aging at 125 C)

Similarly, the modulus, hardness and yield stress plots for the three SAC405 solder joints are in Figures 6.7, 6.8 and 6.9. In all cases, the single crystal joint degradations for each alloy were on the same order as those observed in tensile testing of miniature bulk solder samples of that alloy.

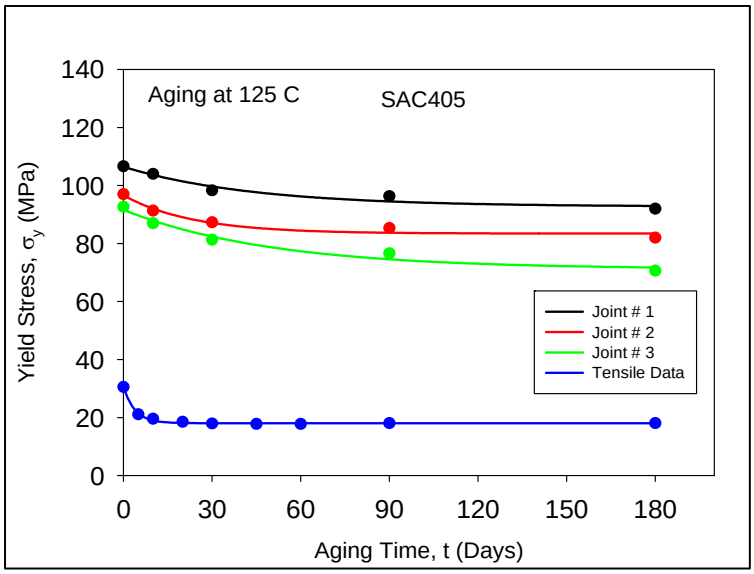

Figure 6.9 Yield Stress Degradation with Aging (SAC405)

6.4 Effect of Aging on Creep Response

As creep behavior is one of the deformation factor in solder joints in microelectronic components, it is important to investigate the creep properties of SAC solder joints under isothermal aging conditions. The creep response was evaluated with aging at 125 C using the nanoindentation. For all of the tests, a constant peak load of 30 mN and a dwell time of 900 sec were used during the hold periods. Using the recorded creep displacement vs. time data, the creep strain rate vs. applied stress curves were generated as outlined in chapter 3, 4 and 5. In addition, uniaxial creep testing of SAC105 bulk small specimens has been done by applied stress of $\sigma = 5$ and 10 MPa for sample aged up to 180 days. Figure 6.10 shows the strain vs. time data for SAC105 bulk solder and corresponding creep strain rate versus stress is fitted with the Garofalo model [23] and plotted in Figure 6.11. It can be seen that for the small uniaxial sample, creep strain rate is

increased with different aging time and stress levels. Now, aging effects in solder joints were correlated to the magnitudes of those observed in testing of miniature bulk specimens.

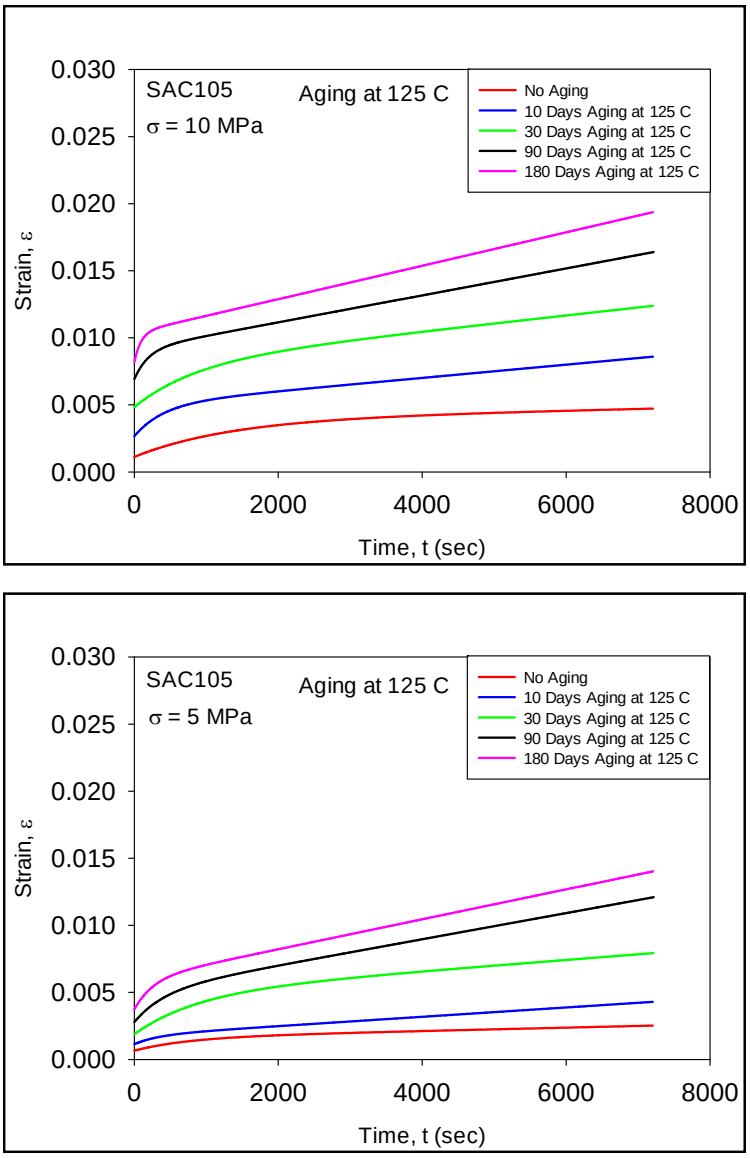

Figure 6.10 Uniaxial Creep Curves for SAC105 Bulk Small Solder with Aging

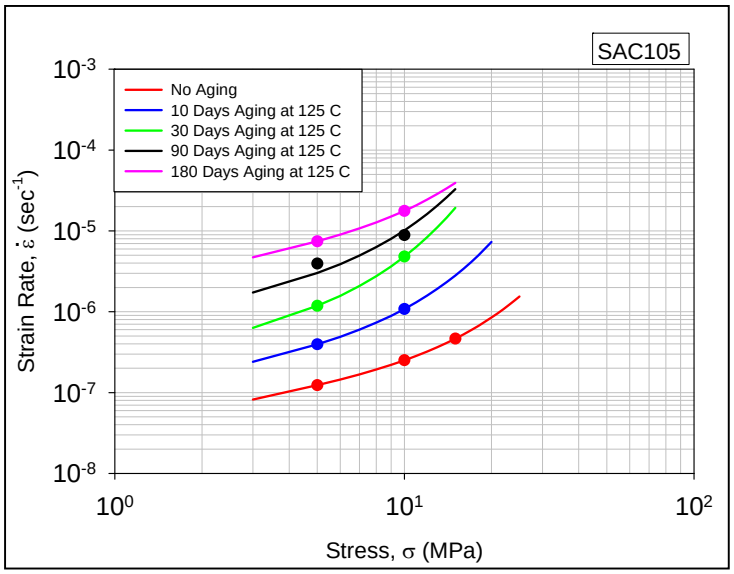

Figure 6.11 Creep Stain Rate vs. Stress for SAC105 Bulk Small Solder with Aging

Figures 6.12 contain the strain rate vs. stress responses for SAC105 joints #1, #2, #3 and #4, respectively. Each curve in these plots represents a fit of the exponential model in to the nanoindentation creep data as outlined in chapter 4 and 5. The red curves in these graphs are for the no aging case, and represent the best (lowest) creep strain rates occurring in the joints. As aging progressed, the creep strain rates became much larger in each joint for every stress level, pushing the creep response curves significantly. The largest changes occurred in the first 30 days of aging, and continues to change with slower rate. The red, blue, green, black and pink data points in each plot are creep strain rates measured by separate tensile testing of extremely small uniaxial specimens that were aged for 0, 10, 30, 90 and 180 days, respectively. The agreement of the creep curves from nanoindentation with the tensile creep data is very good at the lower stress levels.

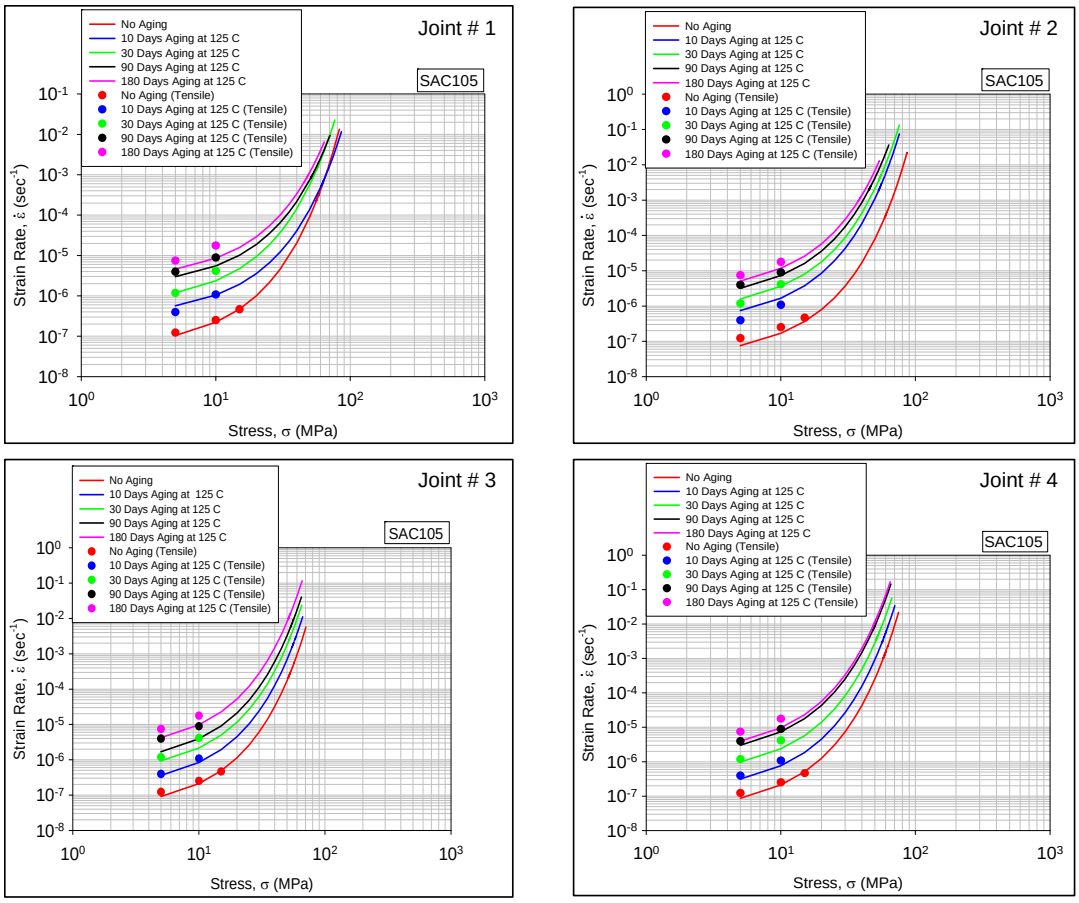

Figure 6.12 Creep Strain Rate vs. Stress for
SAC105, Aging at 125 C

Numerical values of the creep strain rates have been extracted from Figure 6.12 for an applied stress level of 15 MPa and plotted in Figure 6.13 along with tensile creep testing of the small 10 mm uniaxial samples (data points in Figures 6.12). In addition, the creep rates we measured in prior by tensile testing of longer (80-100 mm) miniature bulk uniaxial samples are also included. The increases in the creep stain rates observed for the four joint samples were very similar to those measured for the small 10 mm tensile specimens. For example, after 30 days of aging the four joints had increases of 8-19X, while the creep rate of the small tensile specimens increased by 41.38X. However, dramatically different

results were obtained for the longer miniature bulk tensile samples, where an increase in the creep rate of 3200X was observed. Thus, there were significantly more aging induced degradations in the larger bulk solder tensile samples relative to the joint samples and small tensile specimens. As discussed in chapter 5, this can be explained from the single grain/crystal nature of the joint samples and the small number of grains present in the small tensile specimens that were tested.

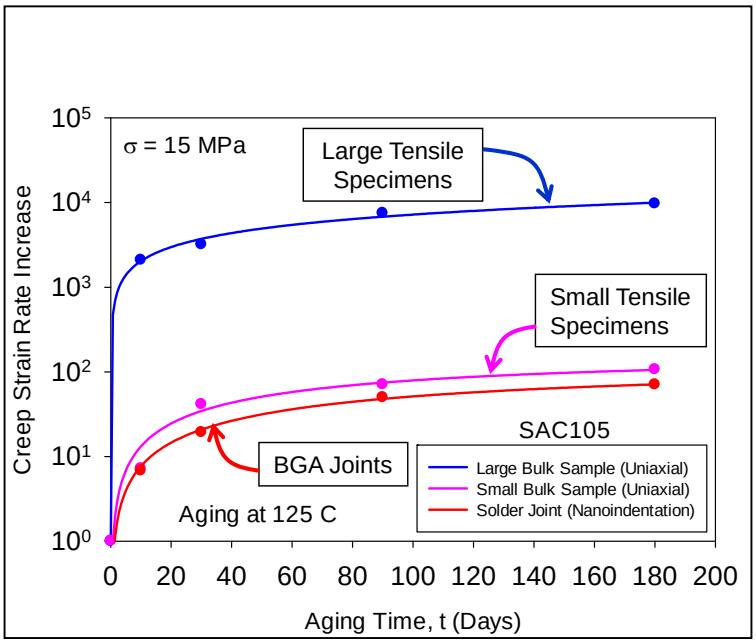

Figure 6.13 Creep Rate Changes with Aging (SAC105)

Similar results were obtained for the aging induced degradation of the creep response of the three other SACN05 solder alloys. For example, Figures 6.14 illustrate the creep rate vs. stress response of the three SAC205 joints for various aging times. These results are plotted in Figure 6.15 for σ = 15 MPa, along with the observed strain rates measured in prior studies by tensile testing of longer miniature bulk uniaxial samples.

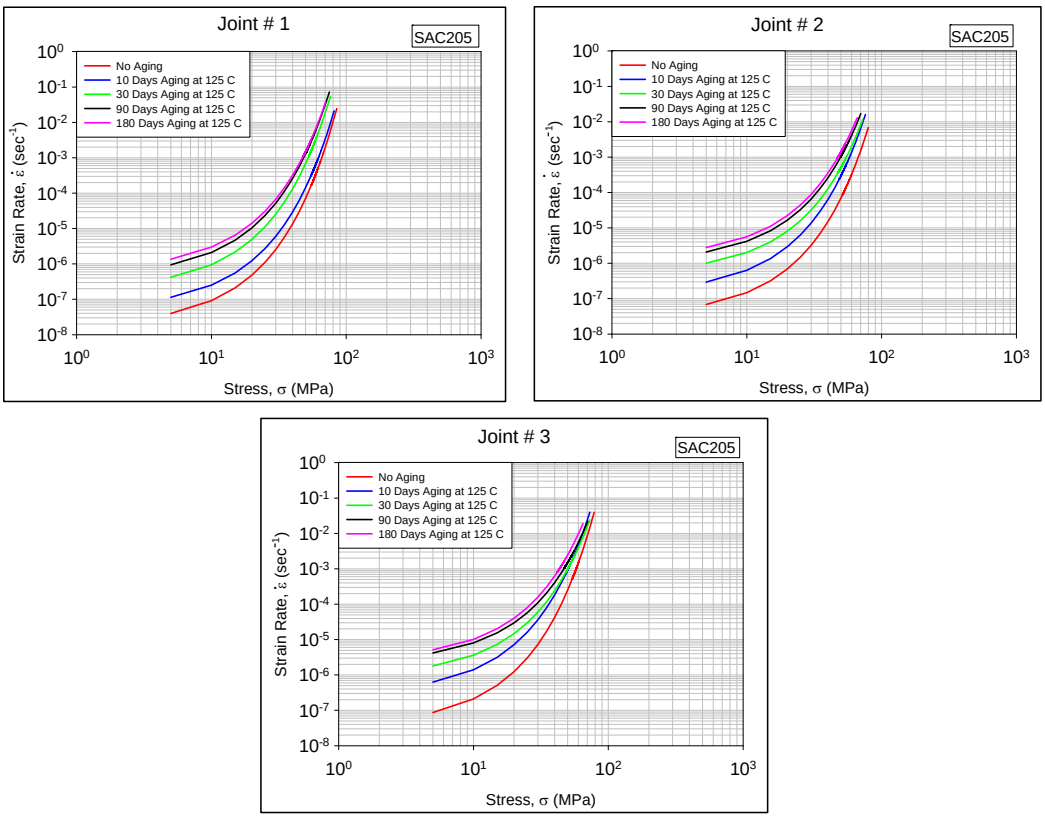

Figure 6.14 Creep Strain Rate vs. Stress for SAC205, Aging at 125 C

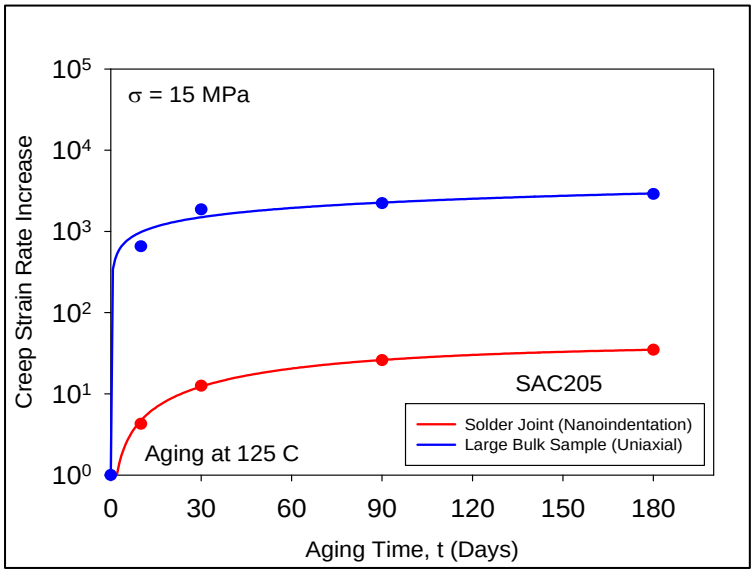

Figure 6:15 Creep Rate Changes with Aging (SAC205)

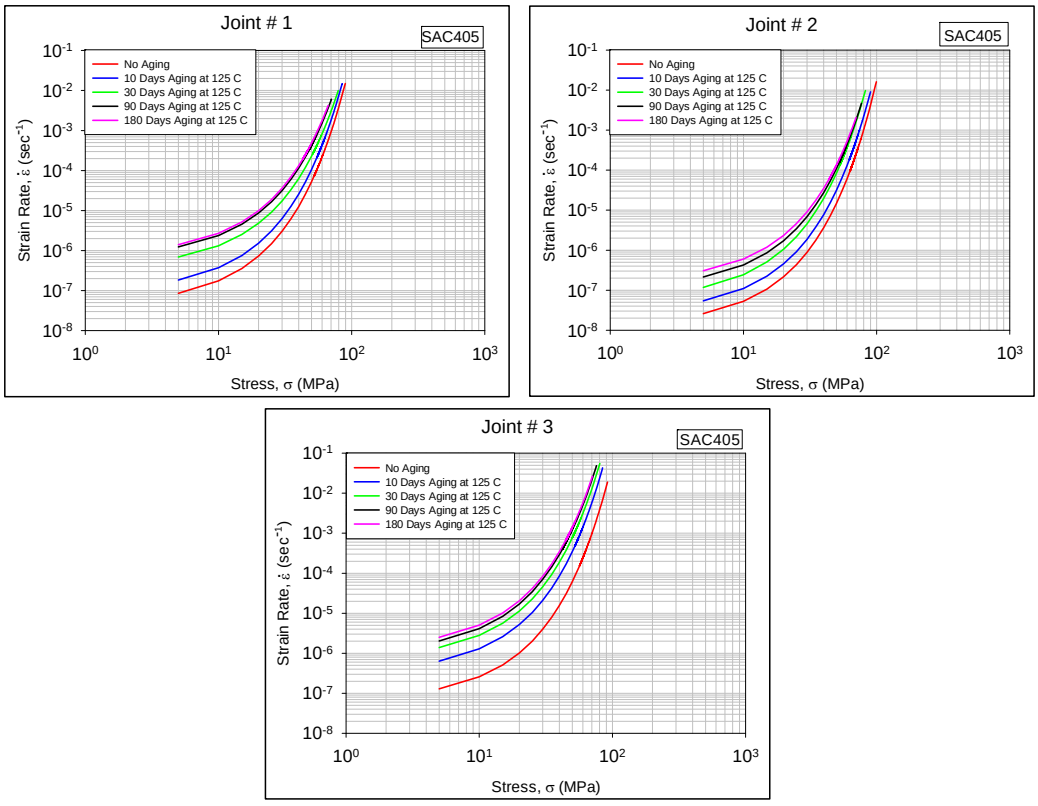

Figure 6.16 Creep Strain Rate vs. Stress for SAC405, Aging at 125 C

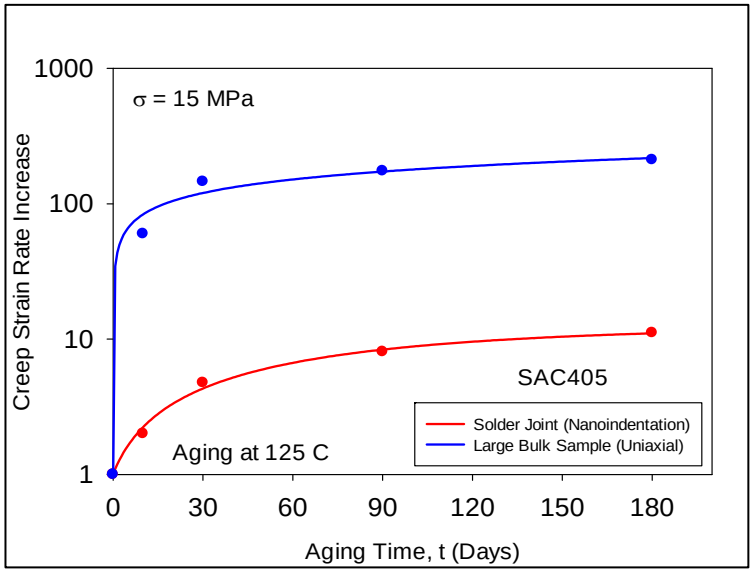

Figure 6.17 Creep Rate Changes with Aging (SAC405)

Finally, the creep rate vs. stress response plots for the three SAC405 joints are contained in Figure 6.16 and the extracted values for σ = 15 MPa are plotted in Figure 6.17.

6.5 Effect of Aging on Solder Alloy Compositions

It is well understood from prior investigations that lowering the silver content of SAC alloy tends to decrease the stiffness and strength, and increase the creep strain rate. Our aging studies using large tensile specimens with hundreds of grains also have suggested the alloys with lower silver content are more susceptible to aging induced degradations in their mechanical properties and increases in their creep strain rates [41-43]. The same conclusions can be made qualitatively using the aging data for single crystal SACN05 solder joints presented above. However, it is difficult to make precise quantitative comparisons of joints for the four alloys because the properties are also strongly dependent on the crystal orientation. As seen from Inverse Pole Figure (Chapter 3), there does not exist a set of four tested joints, one from each alloy, that have similar crystal orientations. Thus, it is difficult to separate the relative performance of the joints from different alloys.

In the discussion below, the relative changes due to aging have been compared for four joints, one from each SACN05 alloy. Aging data for up to 180 days at T = 125 C have been analyzed. The particular joints considered were SAC105 joint #2, SAC205 joint #2, SAC305 joint #3, and SAC405 joint #1. Figure 6.18 illustrates a plot of the percentage reduction in the effective modulus occurring in the four joints as a function of the aging time:

$$\text{Reduction Modulus}(\%) = \left| \frac{E_{\text{Aged}} - E_{\text{NoAging}}}{E_{\text{NoAging}}} \right| \times 100 \qquad (6.1)$$

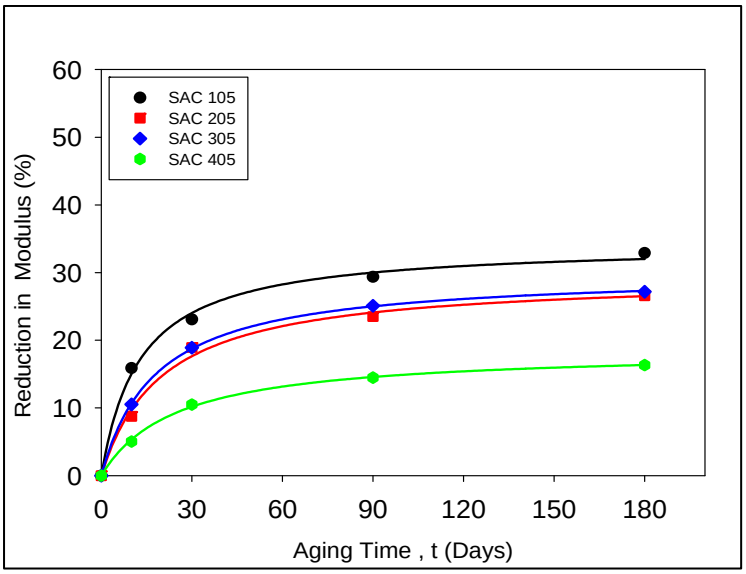

Figure 6.18 Effect of Silver Content on SACN05 Joint Elastic Modulus Change (Aging at 125 C)

Likewise, Figure 6.19 illustrates a plot of the percentage reduction in the hardness occurring in the four joints as a function of the aging time:

$$\text{ReductionHardness}(\%) = \left| \frac{H_{\text{Aged}} - H_{\text{NoAging}}}{H_{\text{NoAging}}} \right| \times 100 \qquad (6.2)$$

The joint data presented in these graphs suggest that lowering the silver content tends to increase the normalized reduction in the mechanical properties (elastic modulus and hardness). The highest percentage changes (degradations) were observed for the SAC105 joint for all aging times, while the lowest changes (degradations) were seen in the SAC405 joint for all aging times.

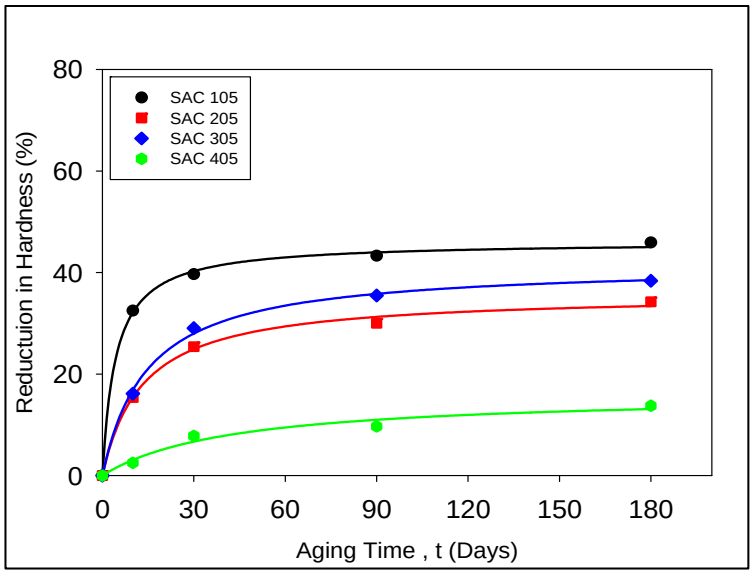

Figure 6.19 Effect of Silver Content on SACN05 Joint Hardness Change (Aging at 125 C)

A similar comparison was made in Figure 6.20 for the degradation of the creep response of the four joints with aging. In this case the increase in the creep strain rate was plotted as a function of aging time:

$$\text{Creep Rate Increase} = \frac{\dot{\varepsilon}_{\text{Aged}}}{\dot{\varepsilon}_{\text{NoAging}}} \tag{6.3}$$

As observed previously, the largest creep rate increase (50X) was found in SAC105 (joint #2), while the smallest creep increase (8X) was found in SAC405 (joint #1). The presence of more Ag content in the SACN05 alloy gives additional precipitates in the form of Ag_3Sn IMC particles, which are responsible for hardening of Sn matrix. In addition, the lower silver content alloys (e.g. SAC105) showed larger coarsening of Ag_3Sn particles relative to the higher silver content alloys (e.g. SAC405).

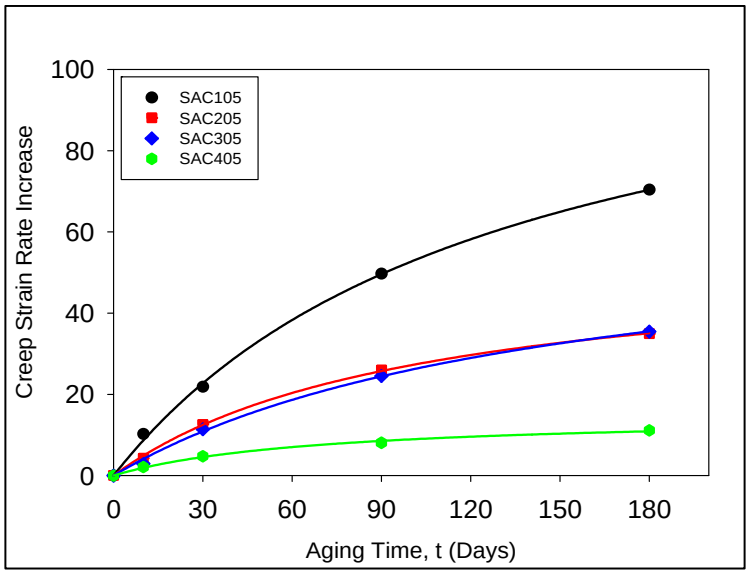

Figure 6.20 Effect of Silver Content on SACN05 Joint Creep Strain Rate Change (Aging at 125 C)

6.6 Summary and Discussion

The effects of silver content on SAC solder aging has been evaluated by testing joints from SACN05 test boards. The results show that the aging induced degradations of the mechanical properties (modulus, hardness) in the SACN05 joints were of similar order (30-40%) as those seen previously in the testing of larger "bulk" uniaxial solder specimens. The creep rates of the various tested SACN05 joints were found to increase by 8-50X due to aging. These degradations, while significant, were much less than those observed in larger bulk solder uniaxial tensile specimens with several hundred grains, where the increases ranged from 200X to 10000X for the various SACN05 alloys. All of the aging effects observed in the SACN05 joints were found to be exacerbated as the silver content in the alloy was reduced.

CHAPTER 7

REDUCTION OF AGING EFFECTS USING MICROALLOY ADDITIONS

7.1 Introduction

The mechanical behavior and reliability of solder materials can be greatly influenced by the addition of microalloying elements (dopants) such as Ni, Bi, In, Mn, etc. Addition of small quantities of these elements to the solder alloy can modify its microstructure, alter its bulk alloy characteristics, increase the volume fraction of eutectic phases, and alter the crack pattern to improve the drop and shock reliability performance. It can also enhance the interfacial IMC layer properties by improving their ductility and toughness. Nogita, et al. [75-76] found that addition of Ni reduce the creep of Cu_6Sn_5 which play a determinant role in the overall deformation of solder joint. It is also found that addition of Ni reduce the thermal expansion of IMC and stabilize the hexagonal IMC down to room temperature [77]. Furthermore, the solubility of Ni modifies the growth texture of IMC [92]. Witkin, et al. [82] have found that the addition of Bi improve the drop shock performance by controlling the IMC thickness and has a significant grain refining effect thus improves the temperature cycling performance. Cai, et al. [17] have observed that several doped alloys are more resistant to aging effects relative to their non-doped versions.

In this chapter, the ability of microalloy additions (dopants) was examined to reduce aging effects in solder joints by nanoindentation testing of several sets of doped/non-doped

alloys. The investigated solder joint alloys included: (1) SAC105, SAC205, SAC105+Ni, SAC105+Mn and SAC205+Ni and (2) Low silver doped alloys, SAC0307, SAC0307+Bi (SACX) and SN100C. For the doped alloys, the base SAC solder in the PBGA component solder balls was modified by microalloying an additional small amount (< 0.05%) of the dopant material (Ni, Mn, Bi etc.). After extraction, the joints were then subjected to various aging conditions at high temperature (0-6 months aging at T = 125 C). After aging, the joints were loaded in the nanoindentation system, and the load-deformation behavior during indentation was used to characterize the mechanical properties of the solder joints for various aging conditions including modulus, hardness, and yield stress. With this approach, aging effects in solder joints were quantified and compare the behavior of the standard and doped alloys.

All components with SAC and SAC+X ball alloys were assembled to test boards with ENIG surface finish using SAC305 paste. With the use of this single paste alloy, the composition of the final joints was slightly different from the component ball alloys. A variety of samples with different component solder ball alloys are being studied and listed in Table 7.1.

Table 7.1 BGA Ball Alloys (SAC and SAC+X

No.	BGA Ball Alloy (Standard)
1	Sn-1.0Ag-0.5Cu (SAC105)
2	Sn-2.0Ag-0.5Cu (SAC205)
3	Sn-0.3Ag-0.7Cu (SAC0307)
No.	BGA Ball Alloy (Doped)
4	Sn-1.0Ag-0.5Cu-0.05Ni (SAC105+Ni)
5	Sn-1.0Ag-0.5Cu-0.03Mn (SAC105+Mn)
6	Sn-2.0Ag-0.5Cu-0.05Ni (SAC205+Ni)
7	Sn-0.3Ag-0.7Cu +Bi (SACX0307)
8	Sn-0.7Cu+0.05Ni+Ge (SN100C)

The aging induced changes in mechanical behavior of single crystals doped/non-doped solder joints have been examined included four SAC105 joints, three SAC205 joints, three SAC0307 joints, four 105+Ni joints, four 105+Mn joints, three SAC205+Ni joints, three SAC0307+Bi joints and three SN100C joints. For each joint alloy, different sets of aging conditions were explored including: no aging; and 10, 30, 90, and 180 days of aging at T = 125 ^{o}C. For each aging duration, six indentations (2 x 3 array) were performed on each ball. The samples were stored in a freezer at T = -10 C prior to cross-sectioning to minimize any aging effects after board assembly. Aging of the epoxy mounted solder joints was then performed in a box oven, and light polishing was performed to remove any oxides after each thermal exposure. The sample preparation, testing, measurement and processing of nanoindentation data for lead free solders are discussed in detail in chapter 3, 4, 5 and 6. The measured data for the doped alloys have been compared to nanoindentation results for the standard (non-doped) alloys to quantify any advantages of the microalloy additions.

7.2 Effect of Dopants on Aging Resistance

The corresponding Inverse Pole Figures for all the tested solder joints were presented in chapter 3. For each alloy, the joint orientations were unique for each joint in the set. For example, using the modulus map, it was expected that joint #1 will have the largest modulus and hardness for the both SAC105+Ni and SAC105+Mn joints. Likewise, joint #1 is expected to have the largest modulus and hardness for the SAC205+Ni joints, SACX0307 joint and SN100C joints.

7.2.1 Effects of Aging on Doped SAC-X Joints Modulus and Hardness

The CSM method was used to measure elastic modulus and hardness values for the 6 indents performed for each aging condition on each solder joint. Plots of the mechanical property evolution with aging time for the SAC105 joints were presented in Figures 6.1 and 6.2 in chapter 6. It was observed that for 180 days of aging at 125 C that the effective modulus of SAC105 joints #1, #2, #3 and #4 degraded by 22.72%, 30.62%, 31.38% and 32.92%, respectively. The corresponding degradations of the hardness over the same period were 39.80%, 42.06%, 43.12% and 45.92%. For example, the measured average values for the first two SAC105 joints are listed in table 7.2 and 7.3. The details of the degradation process for SAC105 solder joints were discussed in chapter 6.

Table 7.2 Elastic Modulus Values from Nanoindentation (SAC105)

Aging Time (Days)	Elastic Modulus (GPa)		
	Joint #1	Joint #2	Tensile
0	50.72	45.12	32.77
10	45.50	38.67	25.10
30	40.86	34.45	19.79
90	38.78	32.20	16.32
180	37.68	31.30	16.06

Table 7.3 Hardness Values from Nanoindentation (SAC105)

Aging Time (Days)	Hardness (GPa)	
	Joint #1	Joint #2
0	0.304	0.282
10	0.247	0.210
30	0.217	0.177
90	0.190	0.166
180	0.183	0.160

Analogous experiments and analysis have been performed for the other doped alloys. For example, the measured average values of modulus and hardness for the first two SAC105+Ni joints are summarized in table 7.4 and 7.5.

Table 7.4 Elastic Modulus Values from Nanoindentation (SAC105+Ni)

Aging Time (Days)	Elastic Modulus (GPa)	
	Joint #1	Joint #2
0	41.39	35.14
10	40.24	33.39
30	39.20	32.19
90	38.76	30.96
180	38.49	30.18

Table 7.5 Hardness Values from Nanoindentation (SAC105+Ni)

Aging Time (Days)	Hardness (GPa)	
	Joint #1	Joint #2
0	0.220	0.210
10	0.211	0.204
30	0.206	0.192
90	0.196	0.189
180	0.194	0.186

These values are similar to those for SAC105 listed in table 7.2 and 7.3. However, the relative modulus and hardness changes with aging for the doped alloy were significantly less. This fact can be observed graphically from the plots of the mechanical property evolution with aging time for the SAC105+Ni joints that are presented in Figures 7.1 and 7.2. Comparing the curves in these graphs to those in Figures 6.1 and 6.2, it can be seen that the mechanical property degradations of the doped alloy were less severe, and that they stabilized more quickly with aging. After 30 days of aging, the modulus and hardness were nearly constant for the doped SAC105+Ni alloy, while the analogous curves for the non-doped SAC105 alloy continued to degrade more significantly with longer aging

times. Similar results were obtained for the aging induced degradations of modulus and hardness for SAC105+Mn as shown in Figures 7.3-7.4.

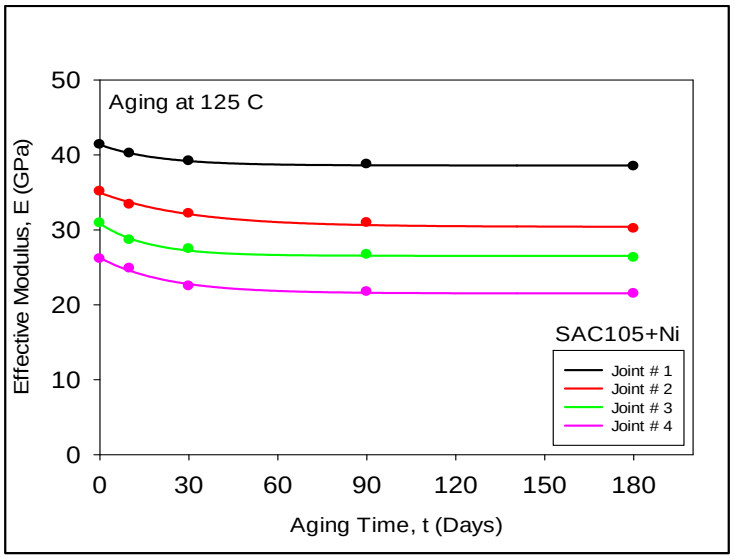

Figure 7.1 Evolution of Modulus with Aging (SAC105+Ni)

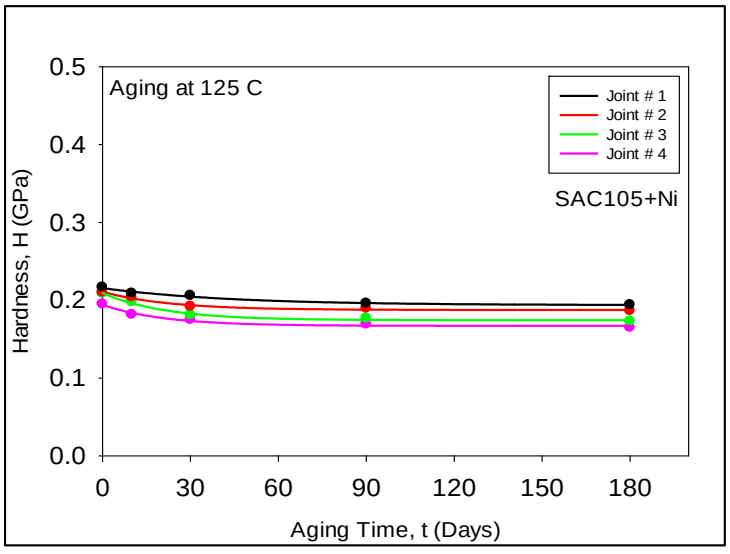

Figure 7.2 Evolution of Hardness with Aging (SAC105+Ni)

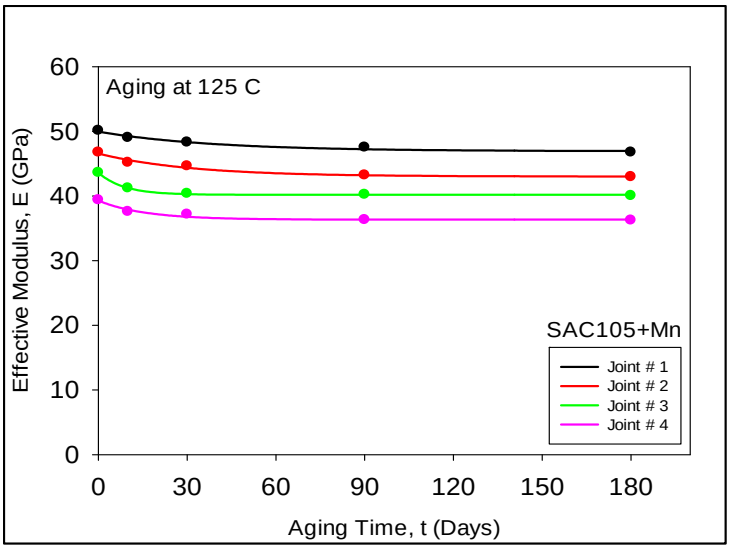

Figure 7.3 Evolution of Modulus with Aging (SAC105+Mn)

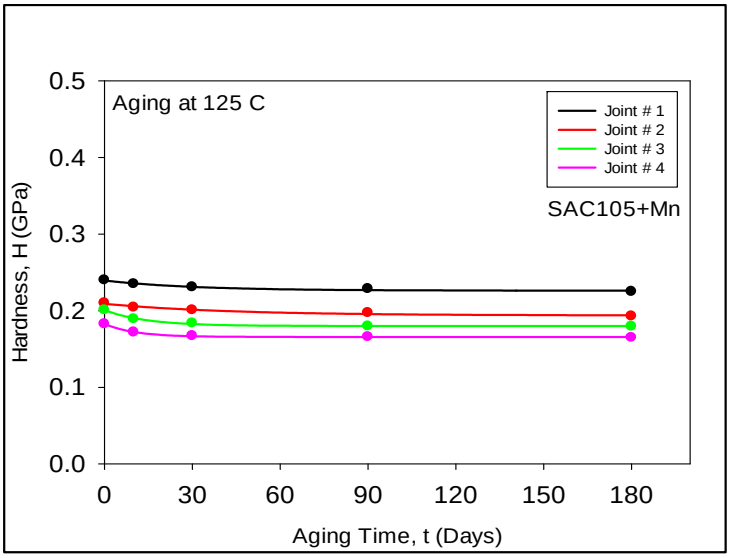

Figure 7.4 Evolution of Hardness with Aging (SAC105+Mn)

Analogous results were obtained for aging induced degradation of other solder alloys. For example, Figure 7.5-7.10 shows the modulus and hardness degradation of SAC205+Ni, SAC0307 and SACX0307 solder joints with different crystal orientation.

The modulus and hardness degradation of SAC205 has been presented in chapter 6 (Figure 6.4-6.5).

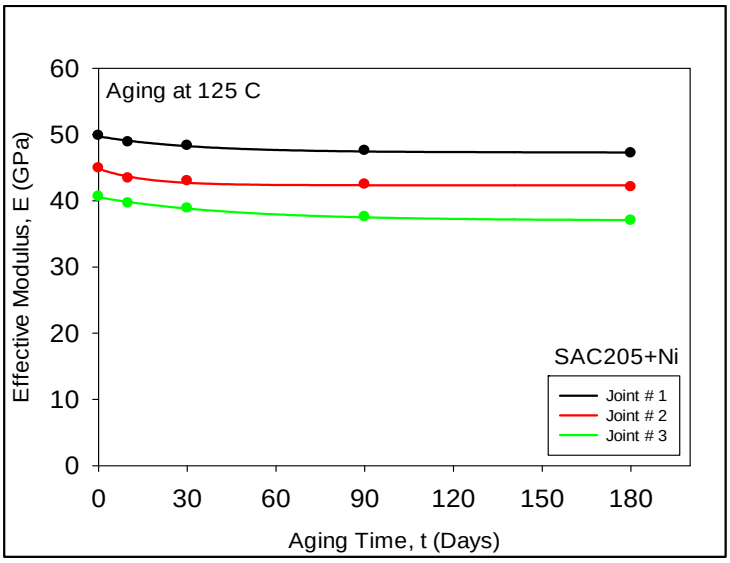

Figure 7.5 Evolution of Modulus with Aging (SAC205+Ni)

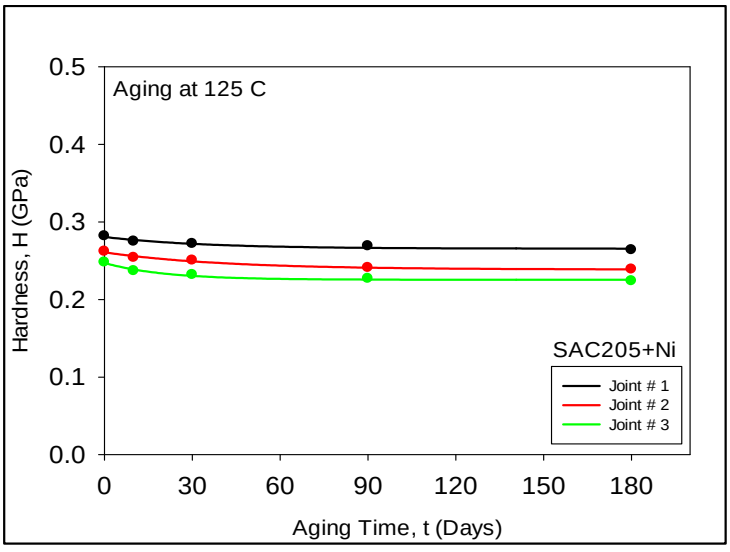

Figure 7.6 Evolution of Hardness with Aging (SAC205+Ni)

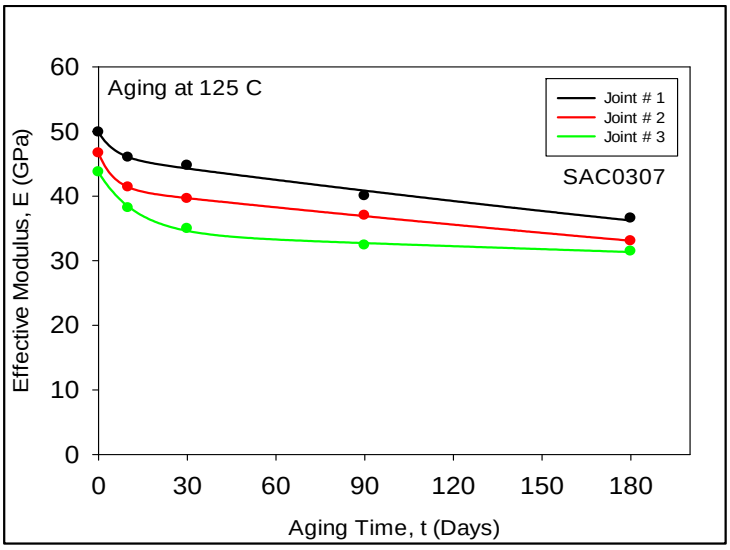

Figure 7.7 Evolution of Modulus with Aging (SAC0307)

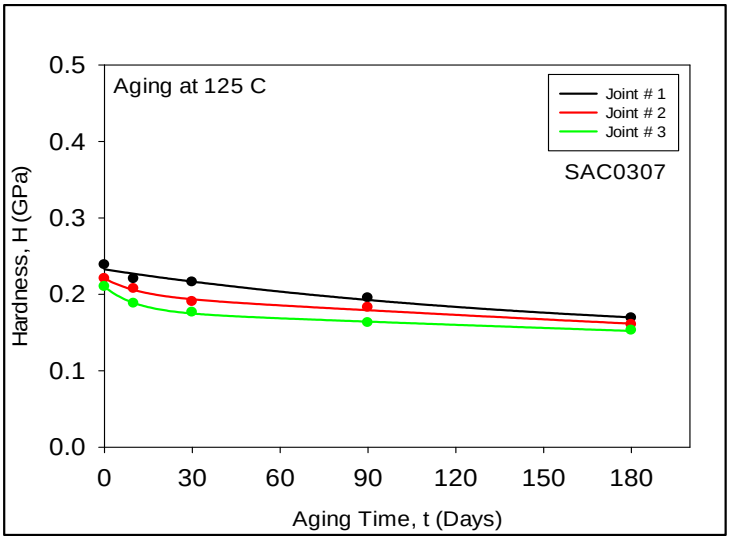

Figure 7.8 Evolution of Hardness with Aging (SAC0307)

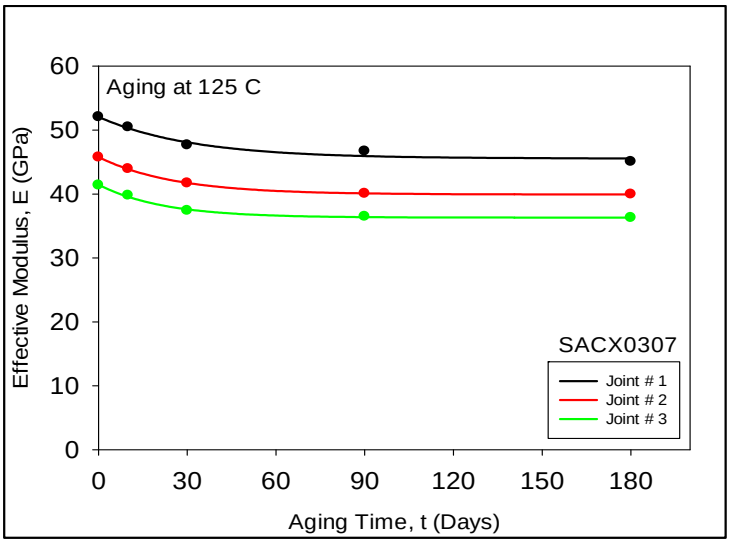

Figure 7.9 Evolution of Modulus with Aging (SACX0307)

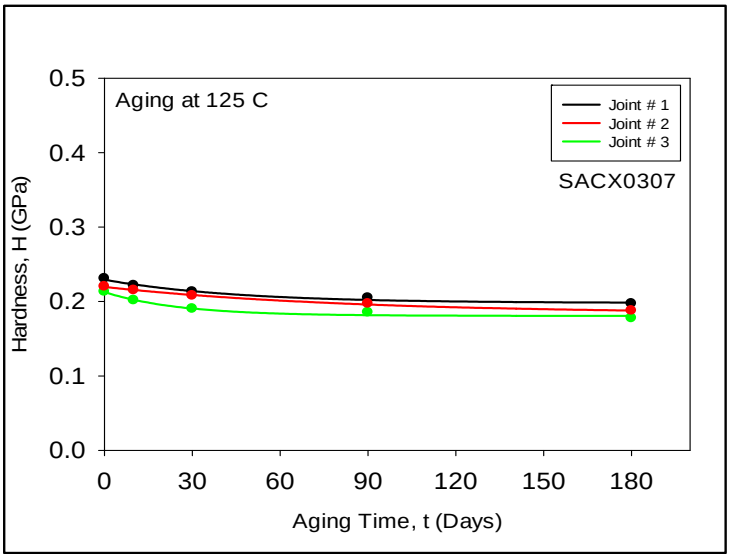

Figure 7.10 Evolution of Hardness with Aging (SACX0307)

7.2.2 Reduction of Aging Effects - SAC105+X (X = Ni, Mn)

As the solder joints tested had a variety of different orientations, it is difficult to make direct quantitative comparisons of the results for non-doped and doped SAC105

joints because the properties are also strongly dependent on the crystal orientations. To better visual the results, the relative changes due to aging have been compared for three joints, one from each alloy (SAC105, SAC105+Ni, and SAC105+Mn). Aging data for up to 180 days at T = 125 C have been analyzed.

Figure 7.11 illustrates a plot of the percentage reduction in the effective modulus occurring in the three joints as a function of the aging time:

$$\text{Reduction Modulus}(\%) = \left| \frac{E_{\text{Aged}} - E_{\text{NoAging}}}{E_{\text{NoAging}}} \right| \times 100 \tag{7.1}$$

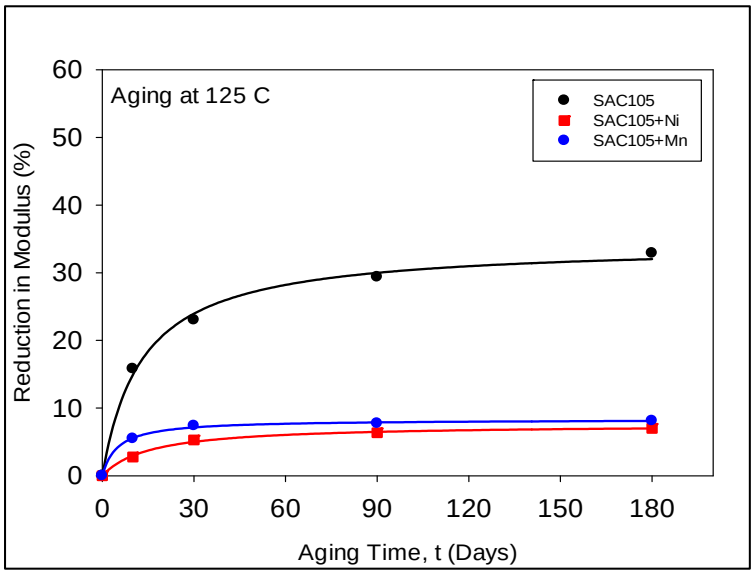

Figure 7.11 Modulus Reduction (SAC105 and SAC105+X)

Likewise, Figure 7.12 illustrates a plot of the percentage reduction in the hardness occurring in the three joints as a function of the aging time:

$$\text{Reduction Hardness}(\%) = \left| \frac{H_{\text{Aged}} - H_{\text{NoAging}}}{H_{\text{NoAging}}} \right| \times 100 \tag{7.2}$$

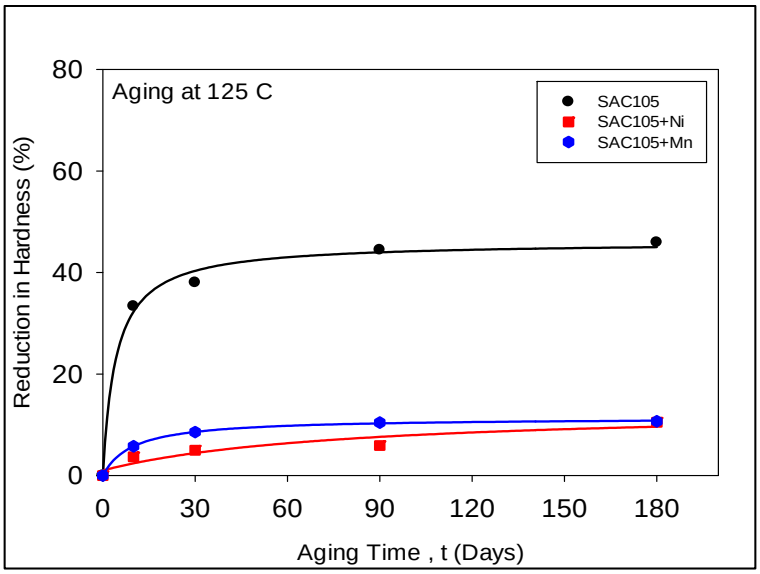

Figure 7.12 Hardness Reduction (SAC105 and SAC105+X)

The data from Figures 11-12 are summarized in table 7.6 and 7.7.

Table 7.6 Modulus Reductions (SAC105 and SAC105+X)

Aging Time (Days)	Elastic Modulus Degradation (%)		
	SAC105	SAC105+Ni	SAC105+Mn
0	0	0	0
10	15.79	2.77	5.47
30	23.01	5.29	7.38
90	29.38	6.35	7.72
180	32.91	7.00	8.11

Table 7.7 Hardness Reductions (SAC105 and SAC105+X)

Aging Time (Days)	Hardness Degradation (%)		
	SAC105	SAC105+Ni	SAC105+Mn
0	0	0	0
10	33.33	3.69	5.77
30	38.03	4.98	8.55
90	44.44	5.90	10.44
180	45.92	10.51	10.69

The results in Figures 7.11-7.12 have shown that addition of the microalloy elements significantly reduced the aging degradations of the effective modulus and hardness in the joints. For example, the average reduction of the effective elastic modulus of the SAC105 joints was 32.9% with 180 days of aging, while the analogous average reductions were 7.0% and 8.1% for the SAC105+Ni and SAC105+Mn joints. Similarly, the average hardness (yield stress) degradation for the SAC105 joints was 45.9%, while those for the SAC105+Ni and SAC105+Mn were 10.5% and 10.7%, respectively.

7.2.3 Reduction of Aging Effects – SAC205+X (X = Ni)

Analogous results were found for SAC205 alloy modified with the addition of nickel micro alloy. The relative changes due to aging have been compared for two joints, one from each alloy (SAC205, SAC205+Ni). Figure 7.13-7.14 illustrates the percentage reduction in the effective modulus and hardness occurring in the two joints as a function of the aging time.

Using similar approach, it was found that after 180 days of aging, the reduction of the effective modulus of SAC205 joint was 25.52 % while reduction was 5.32 % for SAC205+Ni joints. Similarly, hardness reduction was 31.36 % for the SAC205 joints, while for SAC205+Ni was 6.36 %.

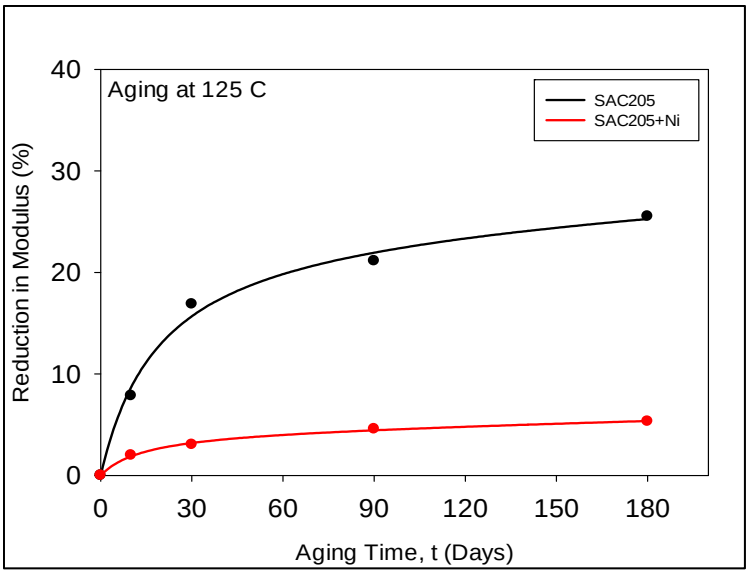

Figure 7.13 Modulus Reduction (SAC205 and SAC205+X)

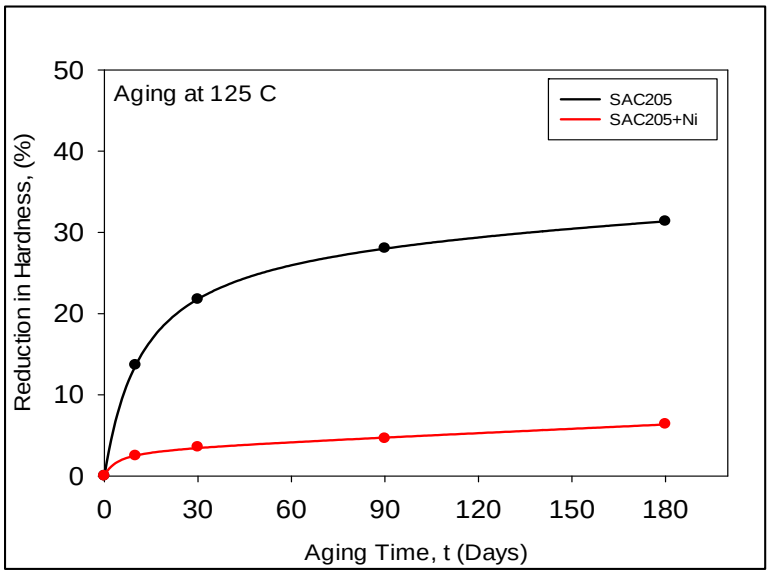

Figure 7.14 Hardness Reduction (SAC205 and SAC205+X)

7.2.4 Reduction of Aging Effects – SAC0307 and SACX0307 (X = Bi)

SAC0307-X alloy modified with addition of bismuth, a low silver alloy use for enhance drop reliability. Three different solder joints were tested with lowest modulus

found in (301) direction with value of 36.30 GPa and largest modulus found in (101) direction with the value of 45.08 GPa. The relative changes due to aging have been compared for two joints, one from each alloy (SAC0307, SAC0307+Bi). Figure 7.15-7.16 illustrates the percentage reduction in the effective modulus and hardness occurring in the two joints as a function of the aging time. After 180 days of aging, the reduction of the effective modulus of SAC0307 joint was 28.07 % while reduction was 12.30 % for SAC0307+Bi joints and hardness reduction was 27.61 % for the SAC0307 joints, while for SAC0307+Bi was 6.36 % .

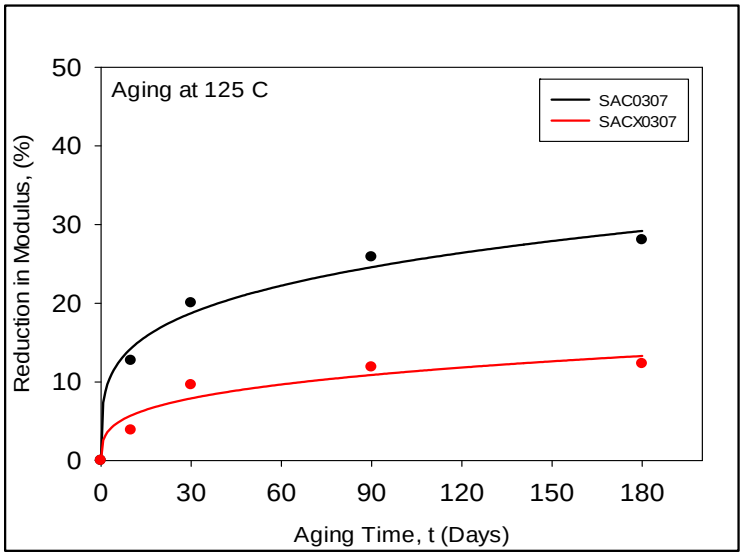

Figure 7.15 Modulus Reduction (SAC0307 and SACX0307)

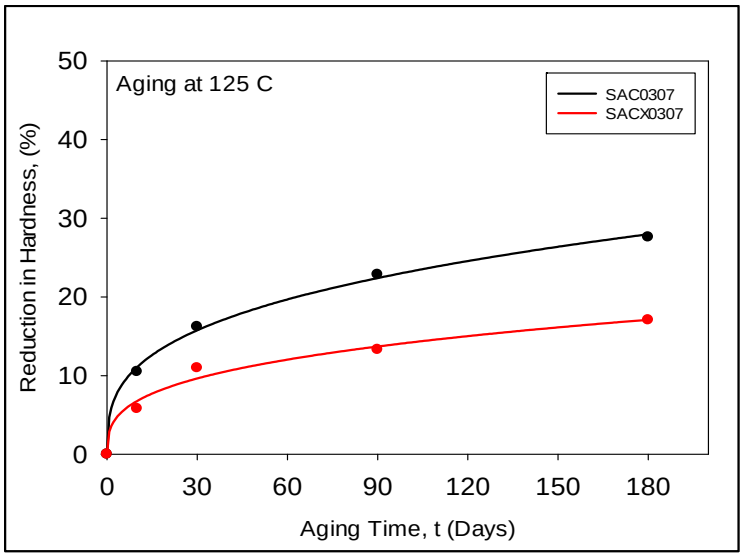

Figure 7.16 Hardness Reduction (SAC0307 and SACX0307)

7.2.5 SN100C

SN100C is low silver alloy doped with nickel. It has high ductility means it can accommodate substantial strain without embrittlement and cracking and that is apparent in the results of the cyclic strain test, thermal cycling test, impact test and vibration test. A great advantage of SN100C is that slower growth of interfacial intermetallic during aging. Figure 7.17-7.18 illustrated the measured average values of modulus and hardness for the SN100C joints. However, after 180 days of aging the relative modulus and hardness changes with aging for the doped alloy were significantly less.

7.3 Effect of Aging on Doped alloy Creep Behavior

Creep testing was performed using Nanoindentation on aged doped solder joints and creep strain rate was modeled as a function of aging time. As previously stated solder joints were tested with different crystallographic orientation.

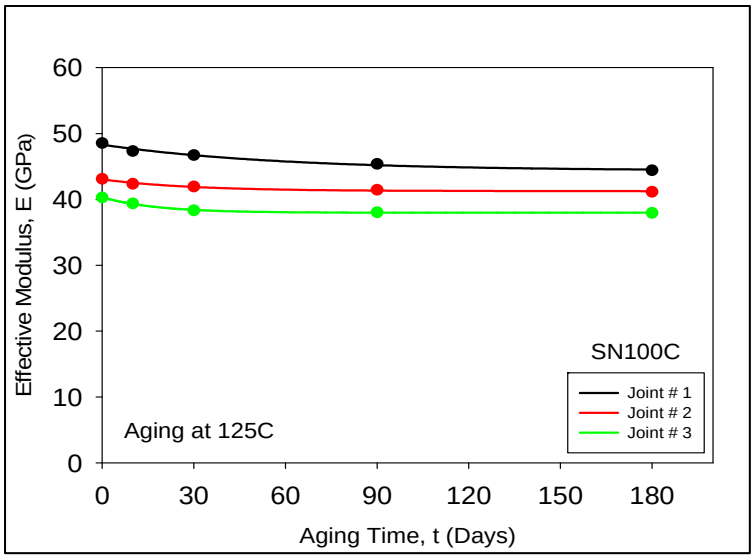

Figure 7.17 Evolution of Modulus with Aging (SN100C)

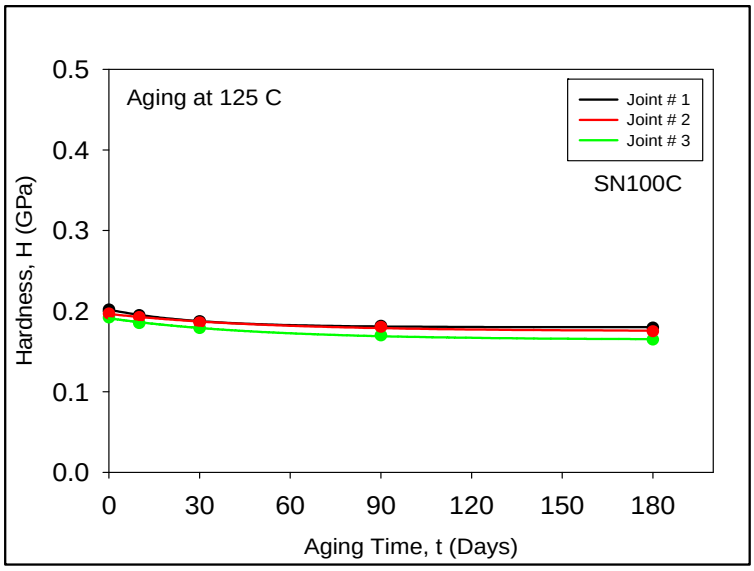

Figure 7.18 Evolution of Hardness with Aging (SN100C)

The developed exponential model was used to fit the data and extrapolated back to lower stress levels. So, similar comparison of degradation of creep response was made

with doped and non-doped alloy. In this case the increase in the creep strain rate was plotted as a function of aging time:

$$\text{Creep Rate Increase} = \frac{\dot{\varepsilon}_{\text{Aged}}}{\dot{\varepsilon}_{\text{NoAging}}} \tag{7.3}$$

Figure 7.19 -7.20 contains the strain rate vs. applied stress response for SAC105+Ni and SAC105+Mn alloy, respectively for various prior aging conditions. The corresponding strain rate vs. applied stress responses for SAC105 joints #1, #2, #3 and #4 for various prior aging conditions are demonstrated in figure 6.12. The results for the SAC105+X joints look similar to the data shown in Figure 6.12 for the SAC105 joints. However, the spacing for the various curves at different aging conditions is smaller for the doped alloy joints (relative to the non-doped joints), suggesting that the doped joints experience smaller aging induced degradations in their creep responses. This observation can be further visualized by graphing the creep rate increase factor using equation 7.3.

Plots of the creep rate increase as a function of aging time are shown in Figure 7.21. Numerical values of the creep strain rate have been extracted from the curves in Figures 7.21 for an applied stress level of 15 MPa and summarized in table 7.8.

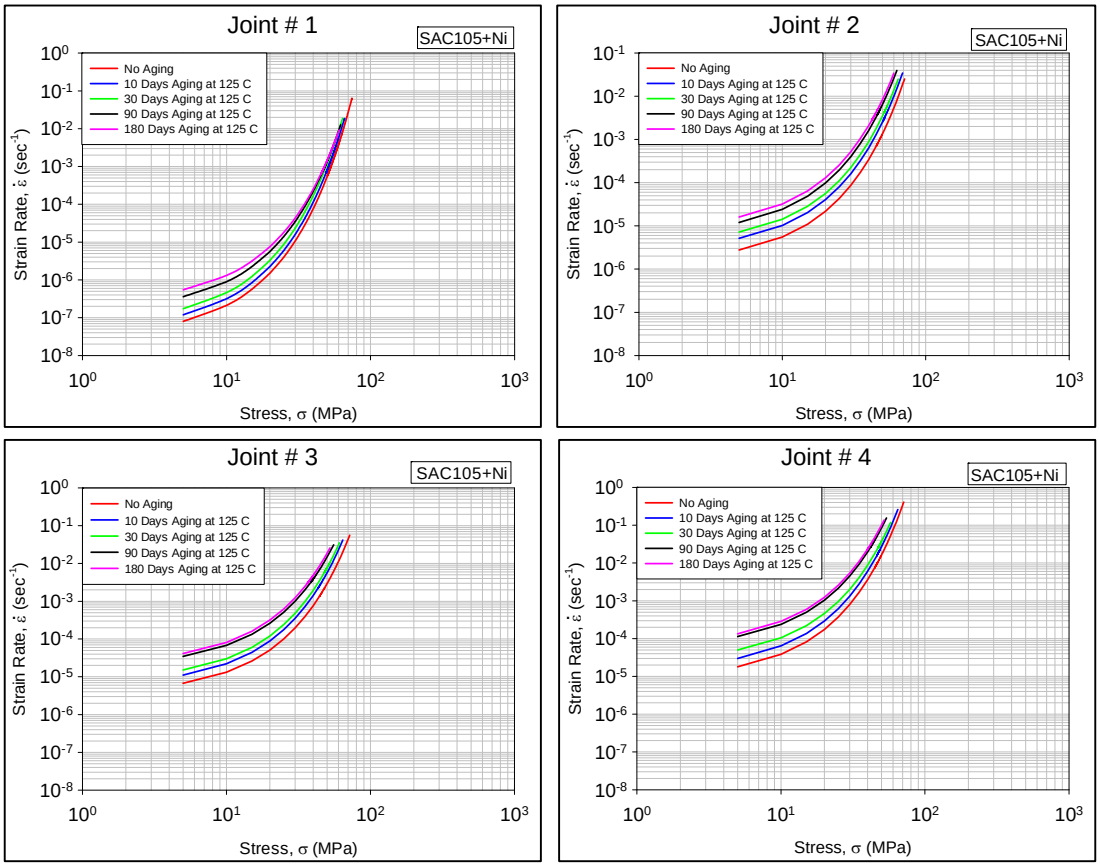

Figure 7.19 Creep Strain Rate vs. Stress (SAC105+Ni)

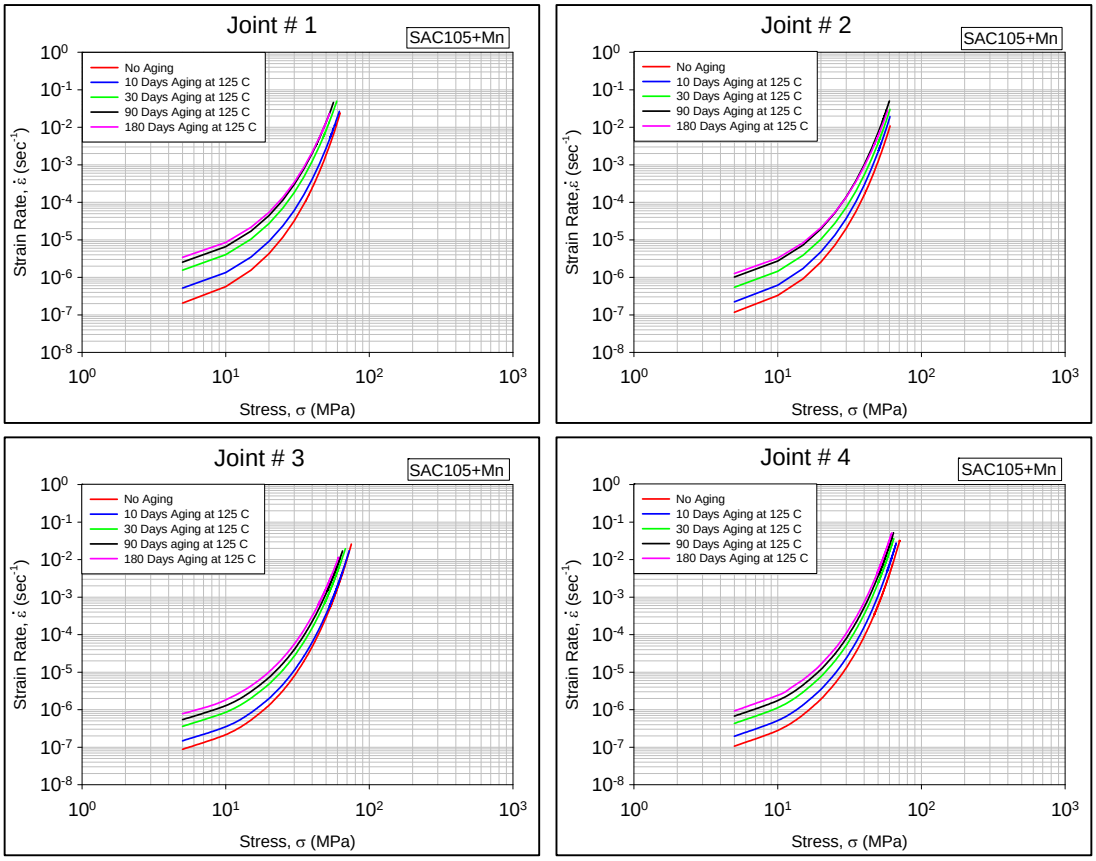

Figure 7.20 Creep Strain Rate vs. Stress (SAC105+Mn)

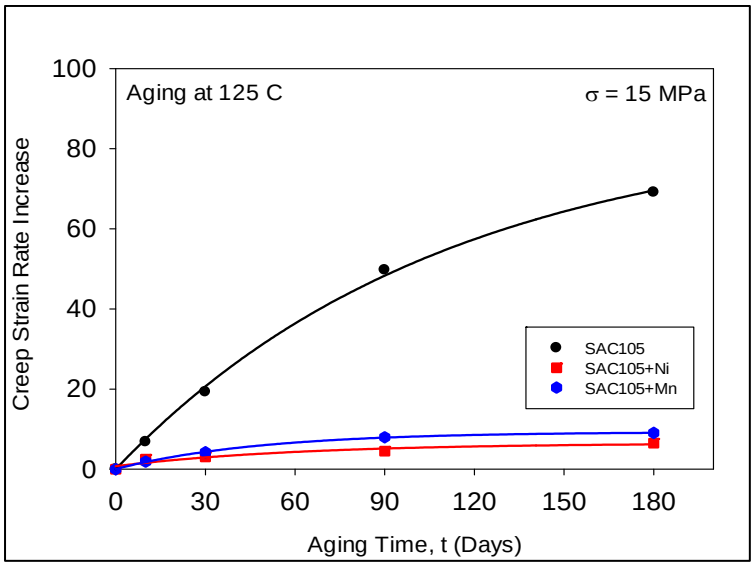

Figure 7.21 Creep Rate Increases with Aging (SAC105 and SAC105+X)

Table 7.8 Creep Rate Increases with Aging (SAC105 and SAC105+X)

Aging Time (Days)	Creep Strain Rate Change, σ = 15 MPa		
	SAC105	SAC105+Mn	SAC105+Ni
0	1X	1X	1X
10	6.78X	1.87X	2.50X
30	19.26X	4.22X	3.07X
90	49.73X	7.95X	4.51X
180	69.12X	9.04X	6.50X

The reduction of creep degradation during aging is quite dramatic for SAC105+Ni and SAC105+Mn doped alloy. After 6 month of aging, creep stain rate increased by 70X for SAC105. On the other hand that increased by 6.5X and 9.05X for SAC105+Ni and SAC105+Mn alloy, respectively. Thus, the creep rate degradations for the SAC105+X alloys were approximately an order of magnitude smaller than that for the non-doped SAC105 alloy. Previous research has suggested that addition of Ni and Mn microalloys disperses the fine distributions of intermetallic compounds, which leads to an increased creep resistance under aging [81].

The analogous creep curves for SAC205+Ni was observed for comparison with the non-doped alloy. However, at aging progress, the creep strain rate increases at a slower rate. Plots of the creep rate increase as a function of aging time are shown in Figure 7.22 for SAC205+X alloy. The creep strain rate increased by 30.90X time for SAC205 while the creep rate increased by 6.03X for SAC205+Ni alloy. Numerical values of the creep strain rate have been extracted from the curves in Figures 7.22 for an applied stress level of 15 MPa and summarized in table 7.9.

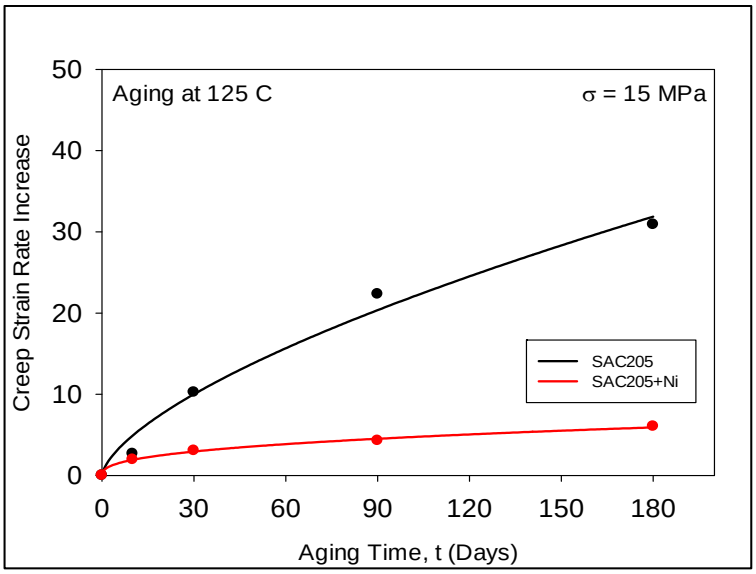

Figure 7.22 Creep Rate Increases with Aging
(SAC205 and SAC205+X)

Table 7.9 Creep Rate Increases with Aging (SAC205 and SAC205+X)

Aging Time (Days)	Creep Strain Rate Change, σ = 15 MPa	
	SAC205	SAC205+Ni
0	1X	1X
10	2.66X	1.95X
30	10.24X	3.05X
90	22.33X	4.28X
180	30.90X	6.03X

The creep degradation of SAC-X alloy have been investigated for the longer aging time. Plots of the creep rate increase as a function of aging time are shown in Figure 7.23. After 6 month of aging, creep stain rate increased by 50.47X for SAC0307 alloy. On the other hand that increased by 27.22X for SAC0307+Ni alloy. The addition of Bi believe to improve the drop shock performance by controlling the intermetallic thickness as well as the creep resistance under aging condition. The corresponding creep strain rate for applied stress of 15 MPa are summarized in table 7.10.

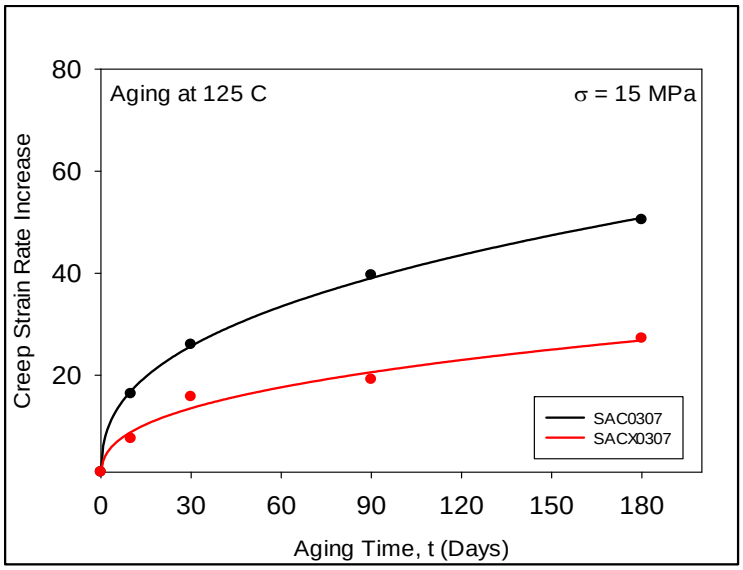

Figure 7.23 Creep Rate Increases with Aging (SAC0307 and SACX0307)

Table 7.10 Creep Rate Increases with Aging (SAC0307 and SAC0307X)

Aging Time (Days)	Creep Strain Rate Change, σ = 15 MPa	
	SAC0307	SAC0307+Bi
0	1X	1X
10	16.33X	7.56X
30	25.99X	15.76X
90	39.62X	19.14X
180	50.47X	27.22X

Similarly, the creep rate degradations for the SN100C alloys were illustrated in Figure 7.24. However, the creep strain rate increases is very slow with prolong aging. Numerical values of the creep strain rate for an applied stress level of 15 MPa are summarized in table 7.11.

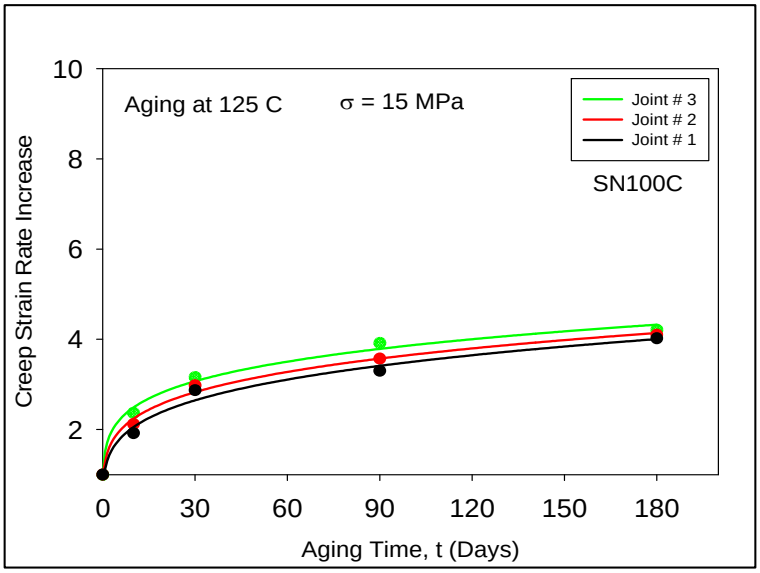

Figure 7.24 Creep Rate Degradations of SN100C Alloys

Table 7.11 Creep Rate Increases with Aging (SN100C)

(Days)	Joint # 1	Joint # 2	Joint # 3
0	1X	1X	1X
0	2.37X	2.12X	1.92X
30	3.16X	2.98X	2.87X
90	3.92X	3.57X	3.30X
180	4.21X	4.10X	4.02X

However, it has been observed that effect of dopant was dramatic and significant to lessen the aging effect. Our results have also confirmed the findings of prior studies by other researchers where it was shown that the addition of microalloy elements improves the ductility and toughness of the interfacial intermetallic layers at the PCB and component

pads, which further enhances drop, shock, and thermal cycling reliability [81, 83, and 85]. For example, addition of Ni has been shown to increase the mechanical properties of bulk solder and better creep performance under harsh environment [80-81]. The addition of Ni was also found to reduce the thermal stress of solder joints [75] and promote the creep strength [81] which was attributed to our findings. The reduction of aging effects with addition of microalloys can be attributed to a refinement of microstructure. It is believed that the microalloys are precipitating within and at the boundaries of the SAC solder subgrains leading to a combination of solid solution and particle strengthening. Aging leads to coarsening of Ag_3Sn intermetallic particles but the redistribution of the dopants results in finer dispersion throughout the interior of the grain and grain boundaries, which diminishes the loss of particle reinforced eutectic regions. It was also found that addition of microalloys has a significant grain refining effect and can decrease the growth of IMC which can possibly inhibit the Sn diffusion along the grain boundary [77]. Thus, aging resistance is improved and the degradations in modulus, hardness, and creep resistance are reduced. Among all the dopants, Ni found to be more superior to counterpart the degradation of aging effect in lead free solder. It has also noticed that rapid degradation is stopped with the addition of doping alloy.

7.4 Summary and Conclusions

In this chapter, the ability of microalloy additions (dopants) to reduce aging effects in solder joints was characterized. Addition of dopants found to be significant to lower the aging effects in solder joints. Addition of these trace elements significantly improved creep resistance under isothermal aging. For example, the average reduction of the effective elastic modulus of SAC105 joints was 32% with 6 month of aging, while the analogous

average reductions were 7% and 8% for the SAC105+Ni and SAC105+Mn alloy. Similarly, the average hardness (yield stress) degradation for the SAC105 joints was 46%, while those for the SAC105+Ni and SAC105+Mn were 10.5% and 10.7%, respectively. Finally, the creep rate increased 70X for the aged SAC105 joints, while the creep rate degradations for the SAC105+Ni (6.5X) and SAC105+Mn (9X) were an order of magnitude smaller. Our findings so far have suggested that the addition of Ni was slightly more effective than the other microalloys in mitigating the effects of aging. It was also confirmed the findings of prior studies, where it was shown that the addition of microalloy elements increase the creep resistance, improves the ductility and toughness of the interfacial intermetallic layers at the PCB and component pads, which further enhances drop, shock, and thermal cycling reliability.

CHAPTER 8

STUDY OF AGING EFFECTS IN LEAD FREE SOLDER JOINTS USING SYNCHROTRON X-RAY MICRODIFFRACTION

8.1 Introduction

In this research, it has been demonstrated and characterized the large changes that occur in the mechanical (constitutive) response and failure behavior of lead free solder joints after exposure to isothermal aging. The observed mechanical behavior changes in joints are due to evolution in the microstructure and residual strains/stresses in the solder material, and measurements of these evolutions are critical to developing a fundamental understanding of solder joint aging phenomena. In this chapter, an initial study of aging effects in the same SAC305 solder joints have been performed that were tested using nanoindentation. The enhanced x-ray microdiffraction technique at the Advanced Light Source (Synchrotron) at the Lawrence Berkeley National Laboratory was employed to characterize several joints after various aging exposures (0, 1, and 7 days of aging at T = 125 C). With such an approach, aging-induced changes in the Sn grain orientation, Sn grain distribution, and residual strain distribution will be measured in the solder joints. These results will be then be correlated with changes in the mechanical response of the joint specimens measured in our laboratory using nanoindentation. With the increase in fundamental understanding of aging induced changes in solder joint mechanical behavior and microstructure, it will be well positioned to develop engineering approaches for predicting and optimizing lead free solder joint reliability.

8.2 X-Ray Microdiffraction Study

As modern electronics devices are increasingly made in smaller and smaller scales, so a thorough understanding of the materials structure-properties-performance relationship at such length scales (0.1 – 10 μm) has become critical. With the recent availability synchrotron sources, X-ray microdiffraction technique can characterize materials at such small scales. X-ray microdiffraction can measure local variations in stress, orientation, and plastic deformation between grains and within individual grains, helping us understand mechanical properties at this critical length scale. In microelectronics industries, the dimensions of the constitutive devices range from a few microns to submicron. Confinement and interfaces make thin film mechanical properties drastically different than bulk materials. With x-ray microdiffraction, we can measure local characteristics such as texture and stress within individual devices, offering an experimental counterpart to computer simulations.

Wu, et al. [108] and Chen, et al. [109] have used x-ray microdiffraction to study the microstructure and plastic deformation in microelectronic interconnect materials under electromigration. They have found the grain growth involves grain boundary migration and rotation of neighboring high resistance grains due to electromigration. In addition, the grain orientation and stress distributions were calculated. They also studied the bending in large grains by looking the shifting of the Laue pattern which provides grain rotation information. Microdiffraction provided the insight into the mechanism of plastic deformation by grain rotation [109].

Kunz, et al. [110] have studied the evidence of residual strain in deformed natural quartz by microdiffraction. In addition, they calculated the individual strain components of the strain tension along the sample axis.

Sarobol, et al. [111] have used microdiffraction to study the effect of grain misorientation and elastic anisotropy on tin whisker and hillock formation. They reported that local elastic strain energy density, grain misorientation, and elastic strain gradients influence the formation process. In another study [112], subgrain formation and recrystallization were identified in thin solder films due to thermal cycling.

8.3 Microdiffraction Experiment

The x-ray microdiffraction measurements were performed on beamline 12.3.2 at the Advanced Light Source (ALS) in Lawrence Berkeley Laboratory (LBNL). The energy range of the x-ray beam varied from 5 keV to 24 keV. The x-ray beam was focused by Kirkpatrick-Baez (KB) mirrors, and the beam size was approximately 1 μm x 1 μm. To understand the effects of aging, the same region on a joint was scanned for different aging times. A 150 μm x 150 μm square area was analyzed, and Focused Ion Beam milling was used to mark this square area on each joint.

The Focused Ion Beam (FIB) instrument uses Dual-Beam (FIB-SEM) systems and it consists of a vacuum system and chamber, a liquid metal ion source, an ion column, a sample stage, detectors, gas delivery system. The schematic and deposition procedure is shown in Figure 8.1. Electron beam deposition of materials can be used to produce very low energy deposition that will not affect the underlying surface of interest. Pt was deposited by ion beam assisted chemical vapor deposition of a precursor organometallic gas. Figure 8.2 illustrated the FIB deposited and scan area. The solder joint samples were

placed on a high precision stage and scanned through the x-ray beam at its focus spot. Each sample was raster scanned with 1 μm step size and a 1 sec exposure time. After initial scanning, the samples were isothermally aged at 125 C for 1 day and then scanned again. Finally, the samples were aged another 6 days at 125 C (for a total aging time of 7 days), and scanned a final time. At each scanning step, the Laue diffraction patterns were collected in reflection geometry, using a MAR133 x-ray CCD detector mounted at 90º to the incident beam. This basic illustration of this experiment is shown in Figure 8.3. Prior to that a rough elemental map of the sample is created using scanning X-ray fluorescence, so that the region of interest can be more precisely pinpointed. If the visual alignment was inaccurate, the scan area is adjusted and redone. The sample can then be positioned even more precisely by using the piezoelectric positioning stage. The map can then be used to determine the coordinates to scan over while collecting Laue patterns from each discrete area in the coordinates of interest.

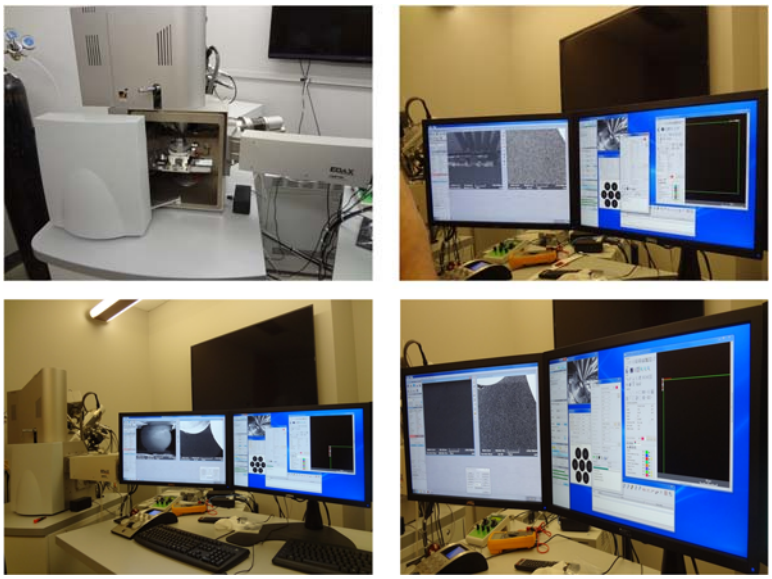

Figure 8.1 Focused Ion Beam Schematic and Deposition Procedure

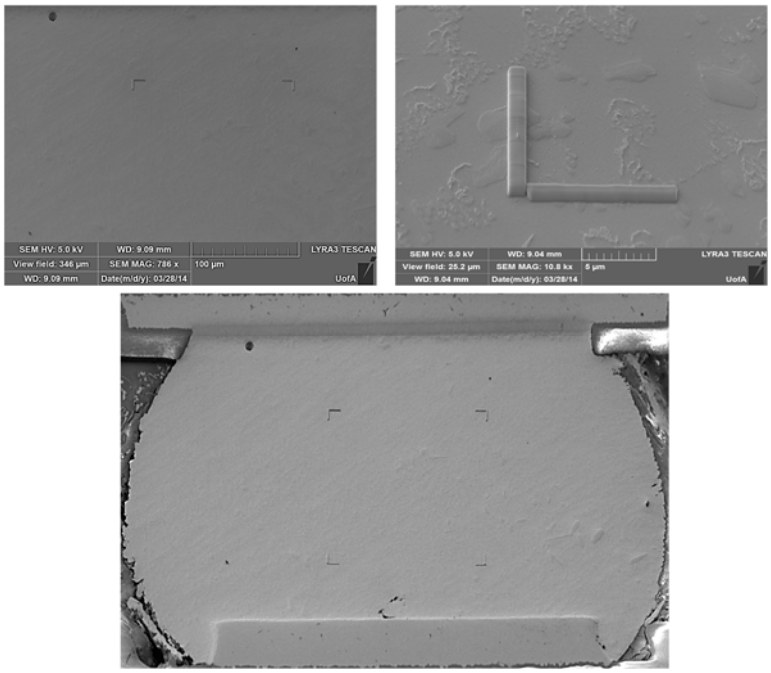

Figure 8.2 Focused Ion Beam Deposited and Scan Area

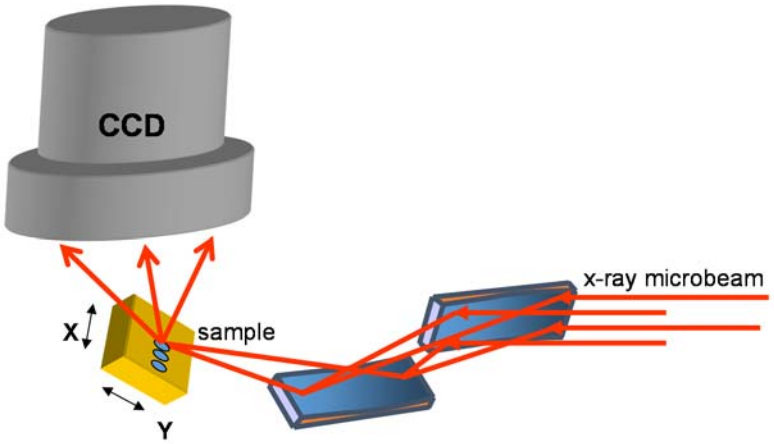

Figure 8.3 Basic Illustration of Experimental Setup

8.3.1 Data Analysis using XMAS

A single white-beam Laue diffraction pattern contains a wealth of information about crystallographic orientation, stress/strain and dislocation structure/density in each

individual crystal of the typically polycrystalline samples. The Laue patterns were analyzed and post processed using the in-house XMAS software. The software allows for automated indexing and strain refinement of the Laue patterns collected during our experiments. The three key step for Laue data analysis involves: (1) Laue peak searching and indexing (2) Crystal unit cell parameter determination and (3) Stress/strain tensor calculation.

1. Laue Peak searching and Indexing

The first step we need to do is to process the image file as captured by the CCD detector. Figure 8.4 shows Laue patterns collected from SAC305 solder joint. The XMAS software reads the CCD file and automatically finds peaks using a peak-searching routine. The peaks are classified by their integrated intensity and fit with a 2D Gaussian, Lorentzian, or Pearson VII function. Once the peak positions are established, Laue pattern can be index with Miller indices.

It is important to define the exact geometry of the experimental system. To do that first, collect a Laue pattern from a calibration sample and use a non-linear least square refinement to extract the necessary geometrical parameters. The ideal calibration sample is an unstrained large single crystal with no defects.

2. Crystal Unit Cell Parameter Determination

The unit cell parameters for a single crystalline grain can be calculated using the same minimization procedure used to calibrate the geometrical parameters of the instrumentation system.

3. Stress/Strain Tensor Calculation

The deviatoric strain tensor is a representation of the unit cell distortion and is calculated by comparing the deviations in the positions of the Laue reflections in an experimental Laue pattern with those in an unstrained Laue pattern. If an arbitrary strain state is applied to this unit cell, the strain will consist of both deviatoric strains and dilatational strain. The deviatoric strains include both simple shear strains and relative tensile/compressive strains. Because deviatoric strains involve changes in angles between atomic planes, the deviatoric strain tensor can be calculated from the angular displacements of the Laue spots in an experimental Laue pattern. The accuracy of the measurement of the deviatoric strain tensor is dependent on the number of Laue reflections used in the strain refinement.

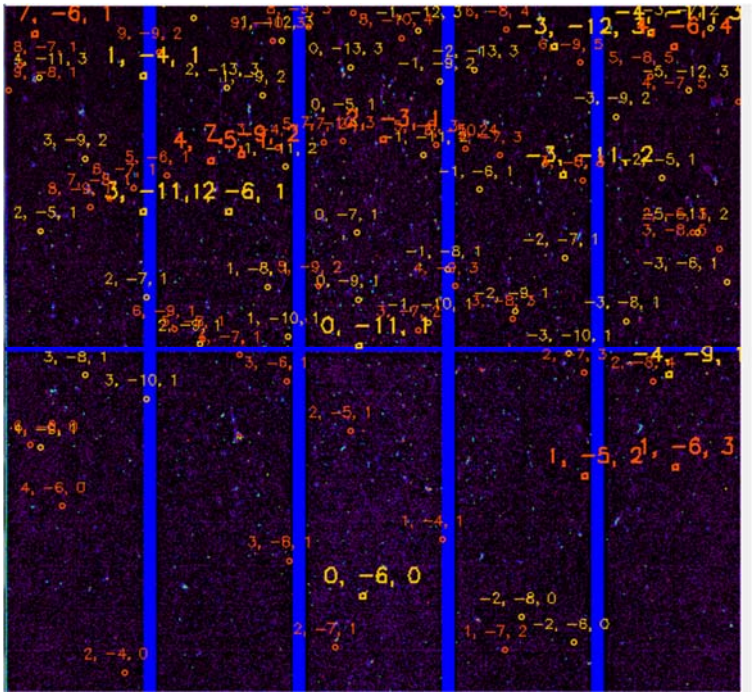

Figure 8.4 Laue Pattern from SAC305 Solder Joint

Laue patterns from multiple grains also can be indexed by an iterative process which compares possible indices for several reflections with the observed angles between the reflections. Once the reflections are indexed, the unit cell parameters and crystal orientations can be determined. From the deviation between the observed Laue pattern and that of the unstrained crystal, deviatoric strain tensor, and thus deviatoric stress tensor can be calculated.

8.4 Microdiffraction Results

Figure 8.5 shows the square area where all the scanned were don't to collect the Laue patterns. Figure 8.6 shows the evolution of the grain orientations of the solder joint with aging. From these orientation maps, it appears that the grains did not grow significantly for seven days of aging. By tracking a particular example grain, it was found that after 7 days of aging, the grain rotated from 0.2644 deg to 0.4602 deg, which is believed to due to shear stress gradient. Grain rotations involve the rearrangement of dislocations that leads to subgrain formation and local plastic deformations.

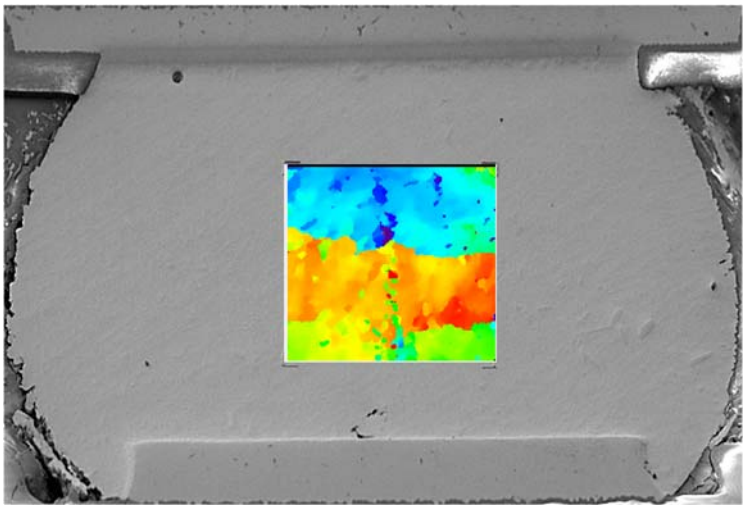

Figure 8.5 Region of Scanned Area

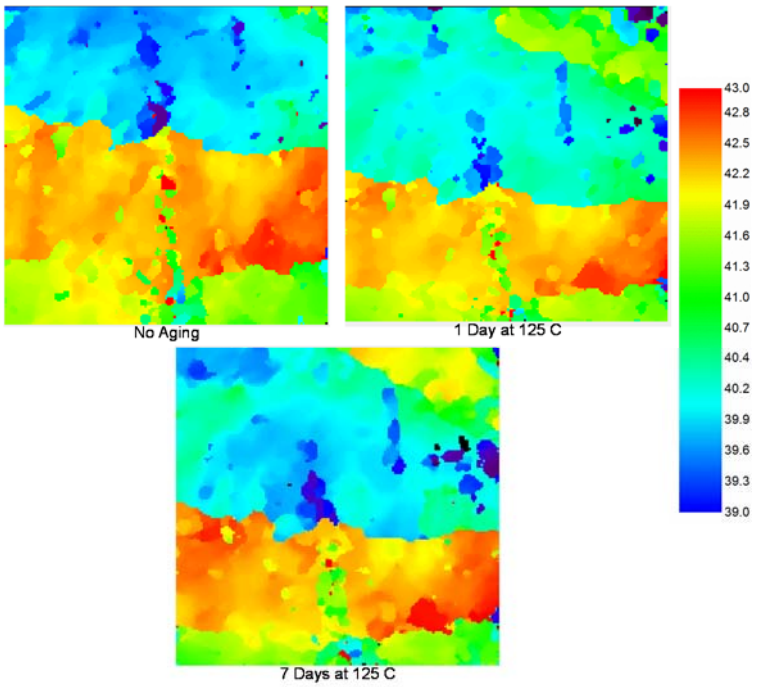

Figure 8.6 Grain Orientation Distribution from Microdiffraction (SAC305)

Subgrain Formation and Evolution with Aging

Figure 8.7 illustrate the typical subgrain in SAC solder joints and how they rotate with isothermal aging. The change in the absolute position of the Laue peak gives the rotation matrix in the deformed crystal body. Using microdiffraction, it is demonstrated that subgrain (subgrain, 1, 2 and 3) rotate notably as aging progress. It is also observed from the orientation map that the subgrain size coarsened with aging. Rotation and formation of subgrain lead to local plastic deformation, which is diffusion controlled and requires higher temperature. However, deformation mechanisms can be driven by local stresses and stress gradients that cause the creep deformations in a material.

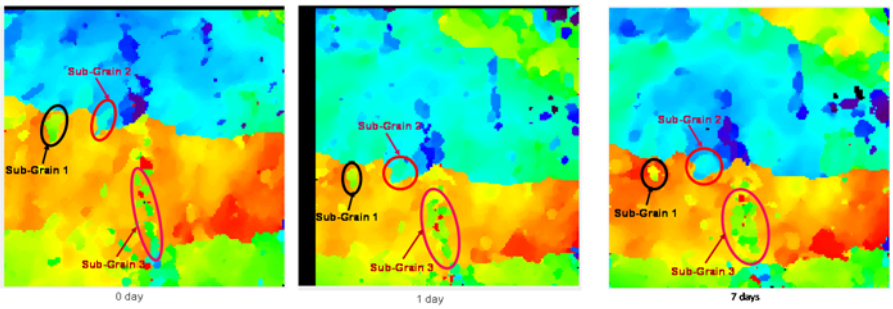

Figure 8.7 Subgrain Evolution with Aging

Using the microdiffraction data, deviatoric stress and strain components were calculated, and demonstrated how they changes with isothermal aging. For example, Figure 8.8 shows a typical result for the deviatoric normal and shear stress components. In all cases, the shear and normal strain components are changing with isothermal aging, and can create stress gradients within the surrounding grains to change the strain energy. This might be the driving force to rotate the grains, cause local changes in the mechanical behavior, and lower the solder joints strength with isothermal aging. Figure 8.9 shows the

variation of equivalent strain with isothermal aging. The strain distribution shows a considerable changes with aging. An increasing trend in equivalent strain also indicates the plastic deformation.

Using Nanoindentation, it has been estimated the degradation of mechanical properties of solder joints which cannot be compared directly. But microdiffraction result confirms that due to isothermal aging local strain and stress components are changing, creating stress gradient, grains are rotating and forming a subgrain which leads to deformation of the solder joints. This might be reason for lowering solder joints strength with isothermal aging.

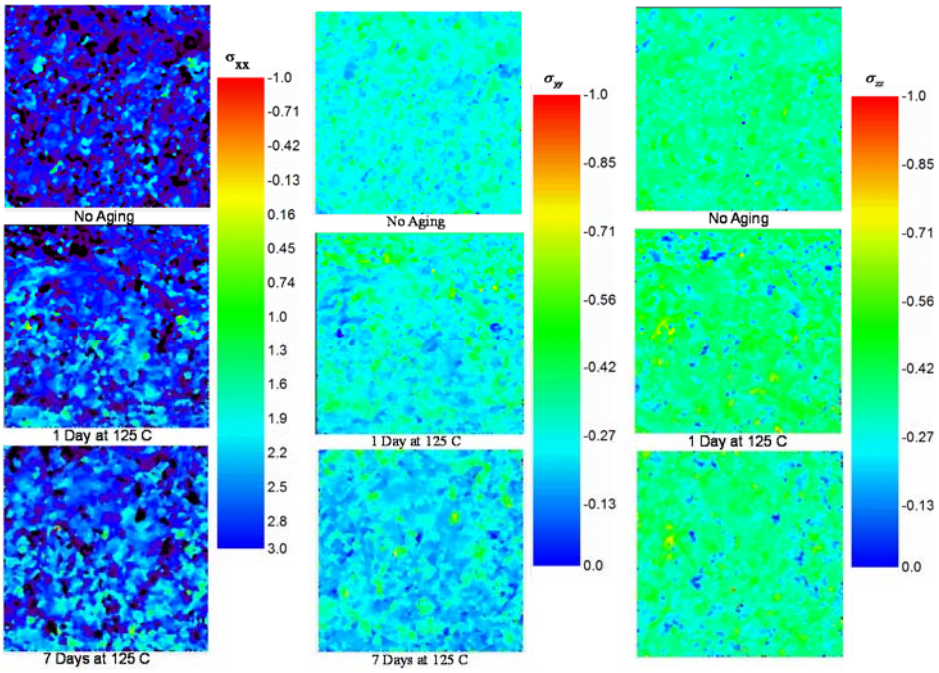

(a)

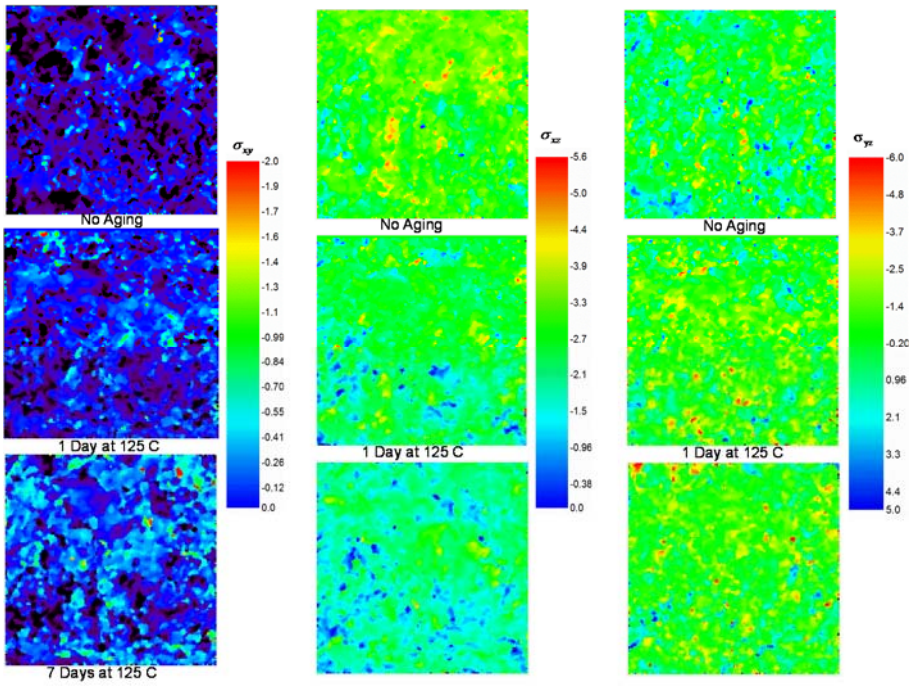

(b)

Figure 8.8 Deviatoric (a) Normal and (b) Shear Stress Distribution from Microdiffraction (SAC305)

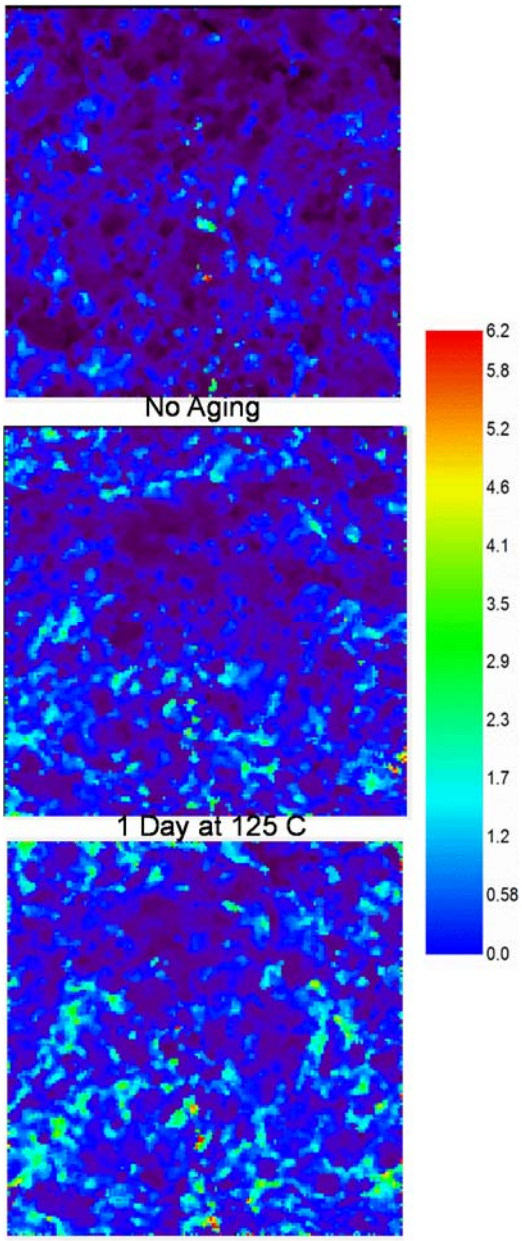

Figure 8.9 Equivalent Strain Distribution from Microdiffraction (SAC305)

8.5 Summary and Conclusions

The observed mechanical behavior changes in joints are due to evolution in the microstructure and residual strains/stresses in the solder material, and measurements of these evolutions are critical to developing a fundamental understanding of solder joint

aging phenomena. The enhanced x-ray microdiffraction beamline at the Advanced Light Source (Synchrotron) at the Lawrence Berkeley National Laboratory was employed to characterize solder joints after various aging exposures (0, 1, and 7 days of aging at T = 125 C). For each case, microdiffraction was used to examine grain growth, grain rotation, sub-grain formation, and residual strain and stress evolution as a function of the aging exposure. Microdiffraction analysis has shown that due to isothermal aging local strain and stress components are changing creating stress gradient, grains are rotate and forming a subgrain which leads to deformation of the solder joints.

CHAPTER 9

SUMMARY AND CONCLUSIONS

9.1 Literature Review

The effects of aging on the constitutive and failure behavior of lead free solder has been extensively reviewed. Due to aging phenomena, the microstructure, mechanical response, and failure behavior of lead free solder joints in electronic assemblies are constantly evolving when exposed to isothermal aging and/or thermal cycling environments. Such aging effects are greatly exacerbated at higher temperatures typical of thermal cycling qualification tests. However, significant changes occur even with aging at room temperature. There is an extensive literature has been discussed that documents the large changes in the microstructure and mechanical behavior that occur in bulk lead free solder specimens during isothermal aging. There have also been some limited investigations on the effects of aging on mechanical properties and creep behavior of solder joint arrays.

While there are clearly aging effects in SAC solder materials, there have been no prior mechanical loading studies on aging effects in actual solder joints extracted from area array assemblies (e.g. PBGA or flip chip). This is due to the extremely small size of the individual joints, and the difficulty in gripping them and applying controlled loadings (tension, compression, or shear). Thus, the following question often comes up: do the large

aging induced mechanical behavior degradations seen in the miniature tension/shear solder specimens match the aging effects experienced in real solder joints.

Nanoindentation techniques have been widely used to probe the mechanical properties and deformation behavior of extremely small material samples. In addition, nanoindentation has been utilized to study aging induced changes in the mechanical properties of intermetallic compound layers in solder joints. In order to correlate the nanoindentation creep results with those from convention creep such as uniaxial creep, researcher have made several attempts.

Isothermal aging also leads to phase coarsening of both β-Sn and precipitates, the dispensing and coalescing of IMC particles, as well as the accelerated growth of grains, and the interfacial IMC thickness between Cu trace and bulk solder joints.

The mechanical behavior and reliability of solder materials can be greatly influenced by the addition of micoalloying elements (dopants) such as Ni, Bi, In, Mn, etc. Addition of small quantities of these elements to the solder alloy can modify its microstructure, alter its bulk alloy characteristics, increase the volume fraction of eutectic phases, and alter the crack pattern to improve the drop and shock reliability performance. It can also enhance the interfacial IMC layer properties by improving their ductility and toughness.

Due to the highly anisotropic nature of Sn crystals, a variety of mechanical properties can be found in a single joint that contains multiple grains. The crystal orientation of tin phase in lead free solder has significant effect on mechanical properties, stress state as well as the reliability of solder joints.

9.2 Sample Preparation and Experimental Procedure

The lead free solder joints in this study were extracted from PBGA assemblies (Amkor CABGA, 14 x 14 mm, 192 balls, 0.8 mm ball pitch, 0.46 mm ball diameter). The test boards were assembled as part of the iNEMI Characterization of Pb-Free Alloy Alternatives Project, and a variety of samples with 10 different solder ball alloys are being studied. The assembled PBGA components were cut out from the test boards and mounted in an epoxy molding compound suitable for SEM microscopy, and then polished to a level appropriate for nanoindentation. Using nanoindentation techniques, the stress-strain and creep behavior of the SAC solder materials have been explored at the joint scale for various aging conditions.

A novel specimen preparation procedure was developed to make the uniaxial specimens. Uniaxial creep testing has been performed on very small bulk specimens to correlate with the nanoindentation creep. In this study, three different dimensions of uniaxial creep sample including 60 x 3 x 0.5 mm (large), 10 x 3 x 0.5 mm (medium) and 10 x 1 x 0.5 mm (small) have been used. In addition, an approach has been developed to predict tensile creep strain rates for low stress levels using nanoindentation creep data measured at very high compressive stress levels.

Due to the variety of crystal orientations realized during solidification, it was important to identify the grain structure and crystal orientations in the tested joints. Polarized light microscopy and Electron Back Scattered Diffraction (EBSD) techniques have been utilized for this purpose.

Microstructural analysis was conducted using Scanning Electron Microscope (SEM). Finally, x-ray microdiffraction technique at the Advanced Light Source

(Synchrotron) at the Lawrence Berkeley National Laboratory was employed to characterize several joints after various aging exposures.

9.3 Characterization of SAC Solder Joints

The mechanical properties and creep behavior of lead free solders are being characterized by nano-mechanical testing of single grain SAC305 solder joints extracted from PBGA assemblies. Using nanoindentation techniques, the stress-strain and creep behavior of the SAC305 solder have been explored at the joint scale. The relationship between crystal orientation and mechanical properties of single grain SAC305 solder joints have been quantified and correlated with the magnitudes observed in tensile testing of miniature bulk specimens using nanoindentation and EBSD. A strong anisotropy in hardness, modulus and creep was found which might help to predict the reliability of the solder joints. An approach has been developed to predict tensile creep strain rates for low stress levels using nanoindentation creep data measured at very high compressive stress levels. Additional testing has been performed on very small tensile specimens and creep rate found in these specimens were on the same order of magnitude as those observed in the single grain joints. These findings also enlighten the interpretation of nanoindentation creep data into uniaxial creep. Dislocation climb has been suggesting the operative creep deformation mechanism.

9.4 Aging Effects in SAC Solder Joint

Aging phenomena in actual solder joints have been explored by nano-mechanical testing of single SAC lead free solder joints extracted from PBGA assemblies. The measured results have demonstrated that the mechanical behavior of actual solder joints

degrade significantly with aging. The results show that the aging induced degradations of the mechanical properties (modulus, hardness) in the SAC joints were of similar order (30-40%) as those seen previously in the testing of larger "bulk" uniaxial solder specimens. For example, the creep rate of the tested SAC305 joints were found to increase by up to 75X with one year of aging. These degradations, while significant, were much less than those observed in larger bulk solder uniaxial tensile specimens with several hundred grains, where the increase was over 900X. Additional testing has been performed on very small tensile specimens with approximately 10 grains, and the aging-induced creep rate degradations found in these specimens were on the same order of magnitude as those observed in the single grain joints. The agreement of the creep curves from nanoindentation with the small scale specimen tensile creep data is very good at the lower stress levels, suggesting that proposed extrapolation procedure has the potential to yield accurate predictions. Thus, the lack of the grain boundary sliding creep mechanism in the single grain joints is an important factor in avoiding the extremely large creep rate degradations occurring in larger bulk SAC samples.

Microstructural analysis of the joints has shown that Ag_3Sn precipitates coarsen during isothermal aging, which results in fewer but larger particles. The Sn dendrite cell size also was observed to grow significantly, but the boundaries are no longer well defined due to coarsening.

9.5 Effects of Silver Content on SAC Solder Aging Resistance

The effects of silver content on SAC solder aging has been evaluated by testing joints from SACN05 (SAC105, SAC205, SAC305, and SAC405) test boards assembled with the same reflow profile. In all cases, the tested joints were extracted from 14 x 14

mm PBGA assemblies. The observed aging effects in the SACN05 solder joints have been quantified and correlated with the magnitudes observed in tensile testing of miniature bulk specimens performed in prior studies. The results show that the aging induced degradations of the mechanical properties (modulus, hardness) in the SACN05 joints were of similar order (30-40%) as those seen previously in the testing of larger "bulk" uniaxial solder specimens. The creep rates of the various tested SACN05 joints were found to increase by 8-50X due to aging. These degradations, while significant, were much less than those observed in larger bulk solder uniaxial tensile specimens where the increases ranged from 200X to 10000X for the various SACN05 alloys. All of the aging effects observed in the SACN05 joints were found to be exacerbated as the silver content in the alloy was reduced.

9.6 Reduction of Aging Effects using Microalloy Addition

The ability of microalloy additions (dopants) to reduce aging effects have been evaluated in solder joints by nanoindentation testing of several sets of doped/non-doped alloys. The investigated solder joint alloys included: (1) SAC105, SAC205, SAC105+Ni, SAC105+Mn and SAC205+Ni and (2) Low silver doped alloys, SAC0307, SAC0307+Bi (SACX) and SN100C. For the doped alloys, the base SAC solder in the PBGA component solder balls was modified by microalloying an additional small amount (< 0.05%) of the dopant material (Ni, Mn, Bi etc.). Our results have shown that addition of the microalloy elements significantly reduced the aging degradations of the mechanical properties and creep resistance in the joints. For example, the average reduction of the effective elastic modulus of SAC105 joints was 32% with 6 month of aging, while the analogous average reductions were 7% and 8% for the SAC105+Ni and SAC105+Mn alloy. Similarly, the

average hardness (yield stress) degradation for the SAC105 joints was 46%, while those for the SAC105+Ni and SAC105+Mn were 10.5% and 10.7%, respectively. Finally, the creep rate increased 70X for the aged SAC105 joints, while the creep rate degradations for the SAC105+Ni (6.5X) and SAC105+Mn (9X) were an order of magnitude smaller. Our findings so far have suggested that the addition of Ni was slightly more effective than the other microalloys in mitigating the effects of aging. The reduction of aging effects with addition of microalloys can be attributed to a refinement of microstructure. It is believed that the microalloys are precipitating within and at the boundaries of the SAC solder subgrain leading to a combination of solid solution and particle strengthening.

9.7 X-ray Microdiffraction to Study Aging Effect in Solder Joints

The observed mechanical behavior changes in joints are due to evolution in the microstructure and residual strains/stresses in the solder material, and measurements of these evolutions are critical to developing a fundamental understanding of solder joint aging phenomena. The enhanced x-ray microdiffraction beamline at the Advanced Light Source (Synchrotron) at the Lawrence Berkeley National Laboratory was employed to characterize solder joints after various aging exposures (0, 1, and 7 days of aging at T = 125 C). For each case, microdiffraction was used to examine grain growth, grain rotation, sub-grain formation, and residual strain and stress evolution as a function of the aging exposure. From the results, it is observed that the grains did not grow significantly after 7 days of aging. However, it was found that after 7 days of aging, the grain rotated from 0.2644 deg to 0.4602 deg, which is believed to due to shear stress gradient. Microdiffraction analysis has shown that due to isothermal aging local strain and stress

components are changing creating stress gradient, grains are rotating and forming a subgrain which leads to deformation of the solder joints.

CHAPTER 10

FUTURE WORK

Aging effects are universally detrimental to reliability, degrade microstructure and material properties thus shorten the service life of a package. Isothermal aging on solder materials research is active in the microelectronic packaging reliability. However, there are some issues still need to be addressed in great detail to improve the mechanical design, reliability assessment, and process optimization of microelectronic packaging. In this chapter some future work is suggested to extend the findings in the dissertation.

- Using Nanoindentation of multigrain samples to measure the 6 compliance coefficient of tin-based materials, allowing the calculation of the orientation dependent elastic modulus.
- Using Nanoindentation how the compliance coefficient of tin-based materials changes with aging and temperature.
- Evaluation of details evolution of microstructure of doped alloy with aging.
- High temperature nanoindentation of actual solder joints with aging.
- Incorporate the aging effects on actual solder joints into reliability models.
- Investigating the effect of anisotropic and crystal orientation on solder joint reliability using crystal plasticity finite element model.
- Compare the nanoindentation of solder joint results with nanoindentation of small miniature bulk specimens.

REFERENCES

1. Vianco, P. T., "Development of Alternatives to Lead-Bearing Solders," No. SAND-93- 0225C; CONF-9308126-1. Sandia National Labs, Albuquerque, NM, USA; *National Center for Mfg. Sciences*, Ann Arbor, MI, USA, 1993.
2. Wood, E. P., and Nimmo, K. L., "In Search of New Lead-Free Electronic Solders," *Journal of Electronic Materials*, Vol. 23(8), pp. 709-713, 1994.
3. Abtew, M., and Guna, S., "Lead-Free Solders in Microelectronics," *Materials Science and Engineering Reports*, Vol. 27(5), pp. 95-141, 2000.
4. Lee, N-C., "Getting Ready for Lead-free Solders," *Soldering & Surface Mount Technology*, Vol. 9(2), pp. 65-69, 1997.
5. https://www.ameslab.gov/files/LeadFreeSolder_Foundation.pdf.
6. Loomans, M. E., and Fine, M. E., "Tin-Silver-Copper Eutectic Temperature and Composition," *Metallurgical and Materials Transactions A*, Vol. 31(4), pp. 1155-1162, 2000.
7. Liu, P. L., and Shang, J. K., "Interfacial Embrittlement by Bismuth Segregation in Copper/Tin–Bismuth Pb-Free Solder Interconnect," *Journal of Materials Research*, Vol. 16(6), pp. 1651-1659, 2001.
8. McCormack, M., and Jin, S., "Improved Mechanical Properties in New, Pb-Free Solder Alloys," *Journal of Electronic Materials*, Vol. 23(8), pp. 715-720, 1994.

9. McCormack, M., Jin, S., Kammlott, G. W., and Chen, H. S., "New Pb-Free Solder Alloy with Superior Mechanical Properties," *Applied Physics Letters*, Vol. 63(1), pp. 15-17, 1993.

10. Ohnuma, I., Cui, Y., Liu, X. J., Inohana, Y., Ishihara, S., Ohtani, H., Kainuma, R., and Ishida, K., "Phase equilibria of Sn-In based micro-soldering alloys," *Journal of electronic materials*, Vol. 29(10), pp. 1113-1121, 2000.

11. Moon, K-W., Boettinger, W. J., Kattner, U. R., Biancaniello, F. S., and Handwerker, C. A., "Experimental and Thermodynamic Assessment of Sn-Ag-Cu Solder Alloys," *Journal of Electronic Materials*, Vol. 29(10), pp. 1122-1136, 2000.

12. Zhu, Q., Zhang, L., Wang, Z., Wu, S., and Shang, J., "Effect of Intermetallics Ag~ 3Sn on the Tensile Property of Sn3.8Ag0.7Cu Solder Alloy," *Acta Metallurgica Sinica*, Vol. 43(1), pp. 41-46, 2007.

13. Pang, H. L., Xu, L., Shi, X. Q., Zhou, W., and Ngoh, S. L., "Intermetallic Growth Studies on Sn-Ag-Cu Lead-Free Solder Joints," *Journal of Electronic Materials*, Vol. 33(10), pp. 1219-1226, 2004.

14. Henderson, D. W., Woods, J. J., Gosselin, T. A., Bartelo, J., King, D. E., Korhonen, T. M., Lehman, L. P., Cotts, E. J., Lauro, P., Shih, D. Y., Goldsmith, C., and Puttlitz, K. J., "The Microstructure of Sn in Near-Eutectic Sn–Ag–Cu Alloy Solder Joints and its Role in Thermo-Mechanical Fatigue," *Journal of Materials Research*, Vol. 19(6), pp. 1608-1612, 2004.

15. Lehman, L. P., Kinyanjui, R. K., Zavalij, L., Zribi, A., and Cotts, E. J., "Growth and Selection of Intermetallic Species in Sn-Ag-Cu No-Pb Solder Systems based on Pad

Metallurgies and Thermal Histories," *Proceedings of the 53rd Electronic Components and Technology Conference*, pp. 1215-1221, New Orleans, LA, 2003.

16. Ma, H. T., Suhling, J. C., "A Review of Mechanical Properties of Lead-Free Solders for Electronic Packaging," *Journal of Materials Science*, Vol. 44(5), pp. 1141-1158, 2009.
17. Cai, Z., Zhang, Y., Suhling, J. C., Lall, P., Johnson, R. W., Bozack, M. J., "Reduction of Lead Free Solder Aging Effects using Doped SAC Alloys," *Proceedings of the 60th Electronic Components and Technology Conference*, pp. 1493-1511, Las Vegas, NV, 2010.
18. Korhonen, T. K., Turpeinen, P., Lehman, L. P., Bowman, B., Thiel, G. H., Parkes, R. C., Korhonen, M. A., Henderson, D. W., and Puttlitz, K. J., "Mechanical Properties of Near-Eutectic Sn-Ag-Cu Alloy over a Wide Range of Temperatures and Strain Rates," *Journal of Electronic Materials*, Vol. 33(12), pp. 1581-1588, 2004.
19. Weertman, J., "Theory of Steady-State Creep based on Dislocation Climb," *Journal of Applied Physics*, Vol. 26(10), pp. 1213-1217, 1955.
20. Kerr, M., and Chawla, N., "Creep Deformation Behavior of Sn–3.5 Ag Solder/Cu Couple at Small Length Scales," *Acta Materialia*, Vol. 52(15), pp. 4527-4535, 2004.
21. Shen, Y-L., Abell, K. C. R., and Garrett, S. E., "Effects of Grain Boundary Sliding on Microstructural Evolution and Damage Accumulation in Tin-Lead Alloy," *International Mechanical Engineering Congress and Exposition (IMECE)*, pp. 71-78, New Orleans, LA, 2002.

22. Ochoa, F., Deng, X., and Chawla, N., "Effects of Cooling Rate on Creep Behavior of a Sn-3.5 Ag alloy," *Journal of Electronic Materials*, Vol. 33(12), pp. 1596-1607, 2004.

23. Garofalo, F., "An Empirical Relation Defining the Stress Dependence of Minimum Creep Rate in Metals," *Transactions of the Metallurgical Society of AIME*, Vol. 227, pp. 351-355, 1963.

24. Frost, H. J., and Ashby, M. F., "*Deformation Mechanism Maps: The Plasticity and Creep of Metals and Ceramics*," Pergamon Press.

25. Lee, B-Z., and Lee, D. N., "Spontaneous Growth Mechanism of Tin Whiskers," *Acta Materialia*, Vol. 46(10), pp. 3701-3714, 1998.

26. Erinc, M., Schreurs, P. J. G., and Geers, M. G. D., "Intergranular Thermal Fatigue Damage Evolution in SnAgCu Lead-Free Solder," *Mechanics of Materials*, Vol. 40(10), pp. 780-791, 2008.

27. Ubachs, R. L. J. M., Schreurs, P. J. G., and Geers, M. G. G., "Elasto-Viscoplastic Nonlocal Damage Modelling of Thermal Fatigue in Anisotropic Lead-Free Solder," *Mechanics of Materials*, Vol. 39(7), pp. 685-701, 2007.

28. Park, S., Dhakal, R., Lehman, L., and Cotts, E., "Measurement of Deformations in SnAgCu Solder Interconnects under In Situ Thermal Loading," *Acta Materialia*, Vol. 55(9), pp. 3253-3260, 2007.

29. Bieler, T. R., Jiang, H., Lehman, L. P., Kirkpatrick, T., Cotts, E. J., Nandagopal, B., "Influence of Sn Grain Size and Orientation in the Thermomechanical Response and Reliability of Pb-Free Solder Joints," *IEEE Transactions on Components and Packaging Technologies*, Vol. 31(2), pp. 370-381, 2008.

30. Villain, J., Mueller, W., Saeed, U., Weipeert, C., Ulrike, C., Artur, S., "Mechanical Behaviour of SAC-Lead Free Solder Alloys with Regard to the Size Effect and the Crystal Orientation," *European Microelectronics and Packaging Conference*, pp. 1-4, 2009.
31. Arfaei, B., Mahin-Shirazi, S., Joshi, S., Anselm, M., Borgesen, P., Cotts, E., Wilcox, J., and Coyle, R., "Reliability and Failure Mechanism of Solder Joints in Thermal Cycling Tests," *Proceedings of the 63rd Electronic Components and Technology Conference*, pp. 976-985, Las Vegas, NV, 2013.
32. Zamiri, A., Bieler, T. R., and Pourboghrat, F., "Anisotropic Crystal Plasticity Finite Element Modeling of the Effect of Crystal Orientation and Solder Joint Geometry on Deformation after Temperature Change," *Journal of Electronic Materials*, Vol. 38(2), pp.231-240, 2009.
33. Jing, H. A. N., Hongtao, C. H. E. N., and Mingyu, L. I., "Role of Grain Orientation in the Failure of Sn-Based Solder Joints under Thermo-Mechanical Fatigue," *Acta Metallurgica Sinica*, Vol. 25(3), pp. 214-224, 2012.
34. Fischer-Cripps, A. C., "*Nanoindentation*," Third Edition, Springer, 2011.
35. Hay, J., Agee, P., Herbert, E., "Continuous Stiffness Measurement during Instrumented Indentation Testing," *Experimental Techniques*, Vo. 34(3), pp. 86-94, 2010.
36. Medvedev, A. S., "Aging of Tin-Lead Solders and Joints Soldered by Them," *Metallovedenie i Obrabotka Metallov*, No. 7, pp. 16-23, 1956.
37. Lampe, B. T., "Room Temperature Aging Properties of Some Solder Alloys," *Welding Journal*, Vol. 55(10), pp. 330-340, 1976.

38. Ma, H., Suhling, J. C., Zhang, Y., Lall, P., Bozack, M. J., "The Influence of Elevated Temperature Aging on Reliability of Lead Free Solder Joints," *Proceedings of the 57th IEEE Electronic Components and Technology Conference*, pp. 653-668, Reno, NV, 2007.

39. Ma, H., Suhling, J. C., Lall P., Bozack, M. J., "Reliability of the Aging Lead-free Solder Joint," *Proceeding of the 56th Electronic Components and Technology Conference*, pp. 849-864, San Diego, CA, 2006.

40. Ding, Y., Wang, C. Q., Tian, Y. H., Li, M. Y., "Influence of Aging Treatment on Deformation Behavior of 96.5Sn3.5Ag Lead Free Solder Alloy During In Situ Tensile Tests," *Journal of Alloys and Compounds*, Vol. 428, pp. 274–285, 2007.

41. Zhang, Y., Cai, Z., Suhling, J. C., Lall, P., Bozack, M. J., "The Effects of SAC Alloy Composition on Aging Resistance and Reliability," *Proceedings of the 59th IEEE Electronic Components and Technology Conference*, pp. 370-389, San Diego, CA, 2009.

42. Zhang, J., Thirugnanasambandam, S., Evans, J. L., Bozack, M. J., Zhang, Y., Suhling, J. C., "Correlation of Aging Effects on the Creep rate and Reliability in Lead Free Solder Joints," *SMTA Journal*, Vol. 25(3), pp. 19-28 2012.

43. Zhang, J., Hai, Z., Thirugnanasambandam, S., Evans, J. L., Bozack, M. J., Zhang, Y., Suhling, J. C., "Thermal Aging Effects on Thermal Cycling Reliability of Lead-Free Fine Pitch Packages," *IEEE Transactions on Components and Packaging Technologies*, Vol. 3(8), pp. 1348-1357, 2013.

44. Xiao, Q., Nguyen, L., Armstrong, W. D., "Aging and Creep Behavior of Sn3.9Ag0.6Cu Solder Alloy," *Proceedings of the 54th Electronic Components and Technology Conference*, pp. 1325-1332, Las Vegas, NV, 2004.

45. Xiao, Q., Bailey, H. J, Armstrong, W. D., "Aging Effects on Microstructure and Tensile Property of Sn3.9Ag0.6Cu Solder Alloy," *Journal of Electronic Packaging*, Vol. 126(2), pp. 208-212, 2004.

46. Chen, W. M., McCloskey, P., O'Mathuna, S. C., "Isothermal Aging Effects on the Microstructure and Solder Bump Shear Strength of Eutectic Sn37Pb and Sn3.5Ag Solders," *Microelectronics Reliability*, Vol. 46(5-6), pp. 896-904, 2006.

47. Anderson, I. E., and Harringa, J. L., "Elevated Temperature Aging of Solder Joints based on Sn-Ag-Cu: Effects on Joint Microstructure and Shear Strength," *Journal of Electronic Materials*, Vol. 33(12), pp. 1485-1496, 2004.

48. Mustafa, M., Cai, Z., Suhling, J., Lall, P., "The Effects of Aging on the Cyclic Stress-Strain Behavior and Hysteresis Loop Evolution of Lead Free Solders" *Proceedings of the 61st Electronic Components and Technology Conference*, pp. 927-939, Orlando, FL, 2011.

49. Mustafa, M., Roberts, J. C., Suhling, J. C., Lall, P., "The Effects of Aging on the Fatigue Life of Lead Free Solders," *Proceedings of the 64th Electronic Components and Technology Conference*, pp. 666-683, Orlando, FL, 2014.

50. Motalab, M., Cai, Z., Suhling, J. C., Zhang, J., Evans, J. L., Bozack, M. J., Lall, P., "Improved Predictions of Lead Free Solder Joint Reliability That Include Aging Effects," *Proceedings of 62nd Electronic Components and Technology Conference*, pp. 513-531, San Diego, CA, 2012.

51. Lall, P., Shantaram, S., Suhling, J., Locker, D., "Effect of Aging on the High Strain Rate Mechanical Properties of SAC105 and SAC305 Lead-free Alloys," *Proceedings of the 63rd IEEE Electronic Components and Technology Conference*, pp. 1277-1293, Las Vegas, NV, 2013.

52. Peng, W., Monlevade, E., and Marques, M. E., "Effect of Thermal Aging on the Interfacial Structure of Sn-Ag-Cu Solder Joints on Cu," *Microelectronics Reliability*, Vol. 47(12), pp. 2161-2168, 2007.

53. Darveaux, R., "Shear Deformation of Lead Free Solder Joints," *Proceedings of the 55th IEEE Electronic Components and Technology Conference*, pp. 882-893, Lake Buena Vista, FL, 2005.

54. Wiese, S., and Wolter, K. J., "Creep of Thermally Aged SnAgCu Solder Joints," *Microelectronics Reliability*, Vol. 47, pp. 223-232, 2007.

55. Dutta, I., Pan, D., Marks, R. A., Jadhav, S. G., "Effect of Thermo-Mechanically Induced Microstructural Coarsening on the Evolution of Creep Response of Sn-Ag-based Microelectronic Solders," *Materials Science and Engineering A*, Vol. 410-411, pp. 48-52, 2005.

56. Chavali, S., Singh, Y., Kumar, P., Subbarayan, G., Dutta, I., and Edwards, D. R. , "Aging Aware Constitutive Models for SnAgCu Solder Alloys, " *Proceedings of the 61st IEEE Electronic Components and Technology Conference* , pp. 701-705, Lake Buena Vista, FL, 2011.

57. Mysore, K., Chan, D., Bhate, D., Subbarayan, G., Dutta, I., Gupta, V., Zhao, J. H., Edwards, D. R., "Aging-Informed Behavior of Sn3.8Ag0.7Cu Solder Alloys,"

Thermal and Thermomechanical Phenomena in Electronic Systems, ITHERM, pp. 870-875, Orlando, FL, 2008.

58. Fix, A. R., Nüchter, W., Wilde, J., "Microstructural Changes of Lead-Free Solder Joints during Long-Term Ageing, Thermal Cycling and Vibration Fatigue," *Soldering & Surface Mount Technology*, Vol. 20(1), pp.13-21, 2008.
59. Rhee, H., Lucas, J. P., and Subramanian, K. N., "Micromechanical Characterization of Thermo-Mechanically Fatigued Lead-Free Solder Joints," J*ournal of Materials Science: Materials in Electronics*, Vol. 13, pp. 477-484, 2002.
60. Lucas, J. P., Rhee, H., Guo, F., Subramanian, K. N., "Mechanical Properties of Intermetallic Compounds Associated with Pb-Free Solder Joints Using Nanoindentation," *Journal of Electronic Materials*, Vol. 32(12), pp 1375-1383, 2003.
61. Chromik, R. R., Vinci, R. P., Allen, S. L., Notis, M. R., "Measuring the Mechanical Properties of Lead Free Solder and Sn-Based Intermetallics by Nanoindentation," *Journal of Metals*, Vol. 55(6), pp. 66-69, 2003.
62. Deng, X., Chawla, N., Chawla, K. K., Koopman, M., "Deformation Behavior of (Cu, Ag)-Sn Intermetallics by Nanoindentation," *Acta Materialia*, Vol. 52, pp. 4291-4303, 2004.
63. Deng, X., Chawla, N., Chawla, K. K., Koopman, M., "Young Modulus of (Cu, Ag)-Sn Intermetallics by Nanoindentation," *Materials Science and Engineering A*, Vol. 364, pp. 240-243, 2004.
64. Gao, F., Taekmoto, T., "Mechanical Properties Evolution of Sn-3.5Ag Based Lead Free Solders by Nanoindentation," *Materials Letters*, Vol. 60, pp. 2315-2318, 2006.

65. Gao, F., Nishikawa, H., Takemoto, T., "Nanoscale Mechanical Response of Sn-Ag Based Lead Free Solders," *Proceedings of the 57th Electronic Components and Technology Conference*, pp. 206-210, Sparks, NV, 2007.

66. Sun, Y., Liang, J., Xu, J. H., Wang, G., Li, X., "Nanoindentation for Measuring Individual Phase Mechanical Properties of Lead Free Solder Alloy," *Journal of Materials Science: Materials in Electronics*, Vol. 19, pp. 514-521, 2008.

67. Liu, Y. C., Teo, J. W. R., Tung, S. K., Lam, K. H., "High Temperature Creep and Hardness of Eutectic 80Au/20Sn Solder," *Journal of Alloys and Compounds*, Vol. 448, pp. 340-343, 2008.

68. Gao, F., Nishikawa, H., Takemoto, T., Qu, J., "Mechanical Properties versus Temperature Relation of Individual Phase in Sn-3.0Ag-0.5Cu Lead Free Solder Alloy," *Microelectronics Reliability*, Vol. 49, pp. 296-302, 2009.

69. Han, Y. D., Jing, H. Y., Nai, S. M. L., Xu, L. Y., Tan, C. M., Wei, J., "Temperature Dependence of Creep and Hardness of Sn-Ag-Cu Lead Free Solders," *Journal of Electronic Materials,* Vol. 39(2), pp.223-229, 2010.

70. Han, Y. D., Jing, H. Y., Nai, S. M. L., Xu, L. Y., Tan, C. M., Wei, J., "Indentation Size Effect on the Creep Behavior of SnAgCu Solder," *International Journal of Modern Physics B*, Vol. 24(1-2), pp. 267-275, 2010.

71. Xu, L., Pang, J. H. L., "Nanoindentation on SnAgCu Solder Joints and Analysis," *Journal of Electronic Materials*, Vol. 35(12), pp. 2107-2115, 2006.

72. Xu, L., Pang, J. H. L., "Nanoindentation Characterization of Ni-Cu-Sn IMC Layer Subjected to Isothermal Aging," *Thin Solid Films*, Vol. 504, pp. 362-366, 2006.

73. Song, J. M., Huang, B. R., Liu, C. Y., Lai, Y. S., Chiu, Y. T., Huang, T. W., "Nanomechanical Response of Intermetallic Phase at the Solder Joint Interface-Crystal Orientation and Metallurgical Effects," *Materials Science and Engineering A*, Vol. 534, pp. 53-59, 2012.

74. Venkatadri, V., Liang, Y., Yan, X., Cotts, E., Srihari, K., Borgesen, P., "Accelerating the Effects of Aging on The Reliability of Lead Free Solder Joints in a Quantitative Fashion," *Proceedings of the 59th Electronic Components and Technology Conference*, pp.398-405, San Diego, CA, 2009.

75. Mu, D., Huang, H., McDonald, S. D. and Nogita, K., "Creep and Mechanical Properties of Cu_6Sn_5 and $(Cu,Ni)_6Sn_5$ at Elevated Temperature," *Journal of Electronic Materials*, Vol. 42(2), pp. 304-311, 2013.

76. Mu, D., Huang, H., Mcdonald, S. D., Read, J., and Nogita, K., "Investigating the Mechanical Properties, Creep and Crack Pattern of Cu_6Sn_5 and $(Cu,Ni)_6Sn_5$ on Diverse Crystal Planes," *Material Science and Engineering*, Vol. A566, pp. 126-133, 2013.

77. Mu, D., Yasuda, H., Huang, H., and Nogita, K., "Growth Orientations and Mechanical Properties of Cu_6Sn_5 and $(Cu,Ni)_6Sn_5$ on Poly-crystalline Cu," *Journal of Alloys and Compounds*, Vol. 536, pp. 38-46, 2012.

78. Mu, D., Read, J., Yang, Y., and Nogita, K., "Thermal Expansion of Cu_6Sn_5 and $(Cu,Ni)_6Sn_5$" *Journal of Materials Research*, Vol. 26(20), pp. 2660-2664, 2011.

79. El-Daly, A. A., Hammad, A. E., Fawzy, A., and Nasrallh, D. A., "Microstructure, Mechanical Properties and Deformation Behavior of Sn-1.0Ag-0.5Cu Solder after Ni and Sb Additions," *Materials and Design*, Vol. 43, pp. 40-49, 2013.

80. El-Daly, A. A., and El-Taher, A. M., "Evolution of Thermal Property and Creep Resistance of Ni and Zn-Doped Sn-2.0Ag-0.5Cu Lead Free Solders," *Materials and Design*, Vol. 51, pp. 789-796, 2013.

81. Hammad, A. E., "Evolution of Microstructure, Thermal and Creep Properties of Ni-doped Sn-0.5Ag-0.7Cu Low-Ag Solder Alloys for Electronic Applications," *Materials and Design*, Vol. 52, pp. 663-670, 2013.

82. Witkin, D. B., "Creep Behavior of Bi-Containing Lead-Free Solder Alloys," *Journal of Electronic Materials*, Vol. 41, pp. 190-203, 2012.

83. Mukherjee, S., Mattila, T. T., and Dasgupta, A., "Effect of Addition of Manganese and Antimony on Viscoplastic Properties and Cyclic Mechanical Durability of Low Silver SAC Solder," *Proceeding of ITherm*, pp. 888-895, San Diego, CA, 2012.

84. Liu, W., Lee, N. C., Porras, A., Ding, M., Gallagher, A., Huang, A., Chen, S., and Lee, JC. B., "Achieving High Reliability Low Cost Lead-Free SAC Solder Joints via Mn or Ce Doping," *Proceedings of the 59th Electronic Components and Technology Conference*, pp. 994-1007, San Diego, CA, 2009.

85. Liu, W., and Lee, N. C., "The Effects of Additives to SAC Alloys on Microstructure and Drop Impact Reliability of Solder Joints," *JOM*, Vol. 59(7), pp. 26-31, 2007.

86. Sweatman, K., Howell, K., Coyle, R., Parker, R., Henshall, G., Smetana, J., Benedetto, E., Lui, W., Pandher, R. S., Daily, D., Currie, M., Nguyen, J., Lee, T. K., Osterman, M., Miremadi, J., Allen, A., Arnold, J., Moore, D., and Chang, G., "iNEMI Lead-Free Alloy Alternatives Project Report: Part III – Thermal Fatigue Results for Low-Ag Alloys," *Proceedings of the SMTAI*, pp. 359-375, 2012.

87. Coyle, R., Parker, R., Arfaei, B., Mutuku, F., Sweatman, K., Howell, K., Longgood, S., and Benedetto, E., "The Effect of Nickel Microalloying on Thermal Fatigue Reliability and Microstructure of SAC105 and SAC205 Solders," *Proceedings of the 64th Electronic Components and Technology Conference*, pp. 425-440, Orlando, FL, 2014.

88. Goodall, R., Clyne, T.W., "A Critical Appraisal of the Extraction of Creep Parameters from Nanoindentation Data Obtained at Room Temperature," *Acta Materialia*, Vol. 54, pp. 5489-5499, 2006.

89. Poisl, W. H., Oliver, W. C., and Fabes, B. D., "The Relationship between Indentation and Uniaxial Creep in Amorphous Selenium," *Journal of Materials Research*, Vol. 10(8), pp. 2024-2032, 1995.

90. Lucas, B. N., Oliver, W. C., "Indentation Power Law Creep of High Purity Indium," *Metallurgical and Materials Transactions A*, Vol. 30(3), pp. 601-610, 1999.

91. Wang, C. L., Lai, Y. H., Huang, J. C., and Nieh, T. G., "Creep of Nanocrystalline Nickel: A Direct Comparison between Uniaxial and Nanoindentation Creep," *Scripta Materialia*, Vol. 62(4), pp. 175-178, 2010.

92. Henshall, G., Miremadi, J., Parker, R., Coyle, R., Smetana, J., Nguyen, J., Lui, W., Sweatman, K., Howell, K., Pandher, R. S., Daily, D., Currie, M., Lee, T. K., Silk, J., Jones, B., Tisdale, S., Hua, F., Osterman, M., Barthel, B., Sack, T., Snugovsky, P., Syed, A., Allen, A., Arnold, J., Moore, D., Chang, G., and Benedetto, E., "iNEMI Lead-Free Alloy Alternatives Project Report: Part I – Program Goals, Experimental Structure, Alloy Characterization, and Test Protocols for Accelerated Life Testing," *Proceedings of the SMTAI*, pp. 335-347, 2012.

93. Henshall, G., "iNEMI Lead-Free Alloy Alternatives Project Report: Thermal Fatigue Experiments and Alloy Test Requirements," *Proceedings of the SMTAI*, pp. 317-324, 2009.

94. Oliver, W. C., and Pharr, G. M., "An Improved Technique for Determining Hardness and Elastic Modulus using Load and Displacement Sensing Indentation Experiments," *Journal of Materials Research*, Vol. 7(6), pp. 1564-1583, 1992.

95. Pharr, G. M., Oliver, W. C., and Brotzen, F. R., "On the Generality of the Relationship among Contact Stiffness, Contact Area, and Elastic Modulus during Indentation," *Journal of Materials Research*, Vol. 7(3), pp. 613-617, 1992.

96. Tabor, D., *Hardness of Metals*, Oxford University Press, 1951.

97. Zhang, P., Li, S. X., and Zhang, Z. F., "General Relationship between Strength and Hardness," *Materials Science and Engineering A*, Vol. 529, pp. 62-73, 2011.

98. LaLonde, A., Emelander, D., Jeannette, J., Larson, C., Rietz, W., Swenson, D., and Henderson, D. W., "Quantitative Metallography of β-Sn Dendrites in Sn-3.8 Ag-0.7 Cu Ball Grid Array Solder Balls via Electron Backscatter Diffraction and Polarized Light Microscopy," *Journal of Electronic Materials*, Vol. 33(12), pp. 1545-1549, 2004.

99. Kunz, M., Tamura, N., Chen, K., Macdowell, A. A., and Ustundag, E., "A Dedicated Superband X-Ray Microdiffraction Beamline for Materials, Geo-, and Environmental Sciences at the Advanced Light Source," *Review of Scientific Instruments*, Vol. 80(3), pp. 035108, 2009.

100. Wiedemann, H., "*Synchrotron Radiation*," Springer Berlin Heidelberg, 2003.

101. Liu, X., Thadesar, P. A., Taylor, C. L., Kunz, M., Tamura, N., Bakir, M. S., and Sitaraman, S. K., "Thermo-Mechanical Strain Measurements by Synchrotron X-ray Diffraction and Data Interpretation for Through-Silicon vias," *Applied Physics Letters*, Vol. 103(2), pp. 022107, 2013.

102. Jiang, T., Wu, C., Spinella, L., Im, J., Tamura, N., Kunz, M., Son, H-Y., Kim, B. G., Huang, R., and Paul P. S., "Plasticity Mechanism for Copper Extrusion in Through-Silicon vias for Three-Dimensional Interconnects," *Applied Physics Letters*, Vol. 103(21), pp. 211906, 2013.

103. Magid, K. R., Nyilas, R. D., and Spolenak, R., "Metal Plasticity by Grain Rotation—Microdiffraction case Studies," *Materials Science and Engineering A*, Vol. 524(1), pp. 33-39, 2009.

104. Suh, J. O., Tu, K. N., and Tamura, N., "Preferred Orientation Relationship between Cu_6Sn_5 Scallop-type Grains and Cu substrate in Reactions between Molten Sn-based Solders and Cu," *Journal of Applied Physics*, Vol. 102(6), pp. 063511-063511, 2007.

105. Chhanda, N., Suhling, J. C., and Lall, P., "Experimental Characterization and Viscoplastic Modeling of the Temperature Dependent Material Behavior of Underfill Encapsulants," *Proceedings of the ASME InterPACK Conference,* Paper No.IPACK2011-52209, pp. 1-13, 2011.

106. Mayo, M. J., and Nix, W. D., "A Micro-Indentation Study of Superplasticity in Pb, Sn and Sn-38 wt%Pb," *Acta Materialia*, Vol. 36(8), pp. 2183-2192, 1988.

107. Mayo, M. J., and Nix, W. D., "Mechanical Properties of Nanophase TiO_2 as Determined by Nanoindentation," *Journal of Materials Research*, Vol. 5(5), pp. 1073-1082, 1990.

108. Wu, A. T., Tamura, N., Lloyd, J. R., Kao, C. R., and Tu, K. N., "Synchrotron X-ray Microdiffraction Analysis on Microstructure Evolution in Sn under Electromigration," *Material Research Society Symposium Proceedings*, Vol. 863, pp. B9-10, 2005.

109. Chen, K., Tamura, N., Valek, B. C., and Tu, K. N., "Plastic Deformation in Al (Cu) Interconnects Stressed by Electromigration and Studied by Synchrotron Polychromatic X-ray Microdiffraction," *Journal of Applied Physics*, Vol. 104(1), pp. 013513, 2008.

110. Kunz, M., Chen, K., Tamura, N., and Wenk, H. R., "Evidence of Residual Elastic Strain in Deformed Natural Quartz," *American Mineralogist*, Vol. 94, pp. 1059-1062, 2009.

111. Sarobol, P., and Chen, W. H., "Effects of Local Grain Misorientation and β-Tin Elastic Anisotropy on Whisker and Hillock Formation," *Journal of Materials Research*, Vol. 28(5), pp. 747-756, 2013.

112. Sarobol, P., Koppes, J. P., Chen, W. H., Su, P., Blendell, J. E. and Handwerker, C. A., "Recrystallization as a Nucleation Mechanism for Whiskers and Hillocks on Thermally Cycled Sn-alloy Solder Films," *Materials Letters*, Vol. 99, pp. 76-80, 2013.